



Delft University of Technology  
Faculty of Electrical Engineering, Mathematics and Computer Science  
Delft Institute of Applied Mathematics

**Inverse Modeling for Magnetic Signature  
Monitoring of Naval Ships**

A thesis submitted to the  
Delft Institute of Applied Mathematics  
in partial fulfillment of the requirements

for the degree

**MASTER OF SCIENCE  
in  
APPLIED MATHEMATICS**

by

**A.R.P.J. Vijn**

**Delft, the Netherlands  
January 2016**

Copyright © 2016 by Aad Vijn. All rights reserved.





**MSc THESIS APPLIED MATHEMATICS**

**“Inverse Modeling for Magnetic Signature Monitoring of Naval Ships”**

A.R.P.J. Vijn

**Delft University of Technology**

**Daily supervisors**

Dr. ir. E.S.A.M. Lepelaars  
Dr. ir. M. Keijzer

**Other thesis committee members**

Dr. ir. M.B. van Gijzen

**Responsible professor**

Prof. dr. ir. A. Heemink

January 2016

Delft, the Netherlands



# **Inverse Modeling for Magnetic Signature Monitoring of Naval Ships**



## Abstract

In this project, we have defined a prediction model for the magnetic signature of the **M4**, based on on-board measurements of the magnetic field and an accurate description of the geometry of the steel object. The prediction model consists of consecutively solving an inverse problem and the computation of a forward problem. The forward problem was first derived and used as a starting point for the derivation of the inverse problem.

To analyze the behavior of an inverse problem, theory of inverse modeling is discussed. The notion of a generalized inverse operator enables one to come up with best-approximate solutions of the inverse problem. Furthermore, we showed that the inverse problem involved in this project is, at a fundamental level, ill-posed, in the sense of Hadamard's definition of well-posedness. This shows that solving the inverse problem is hard and that additional tools are required to produce good solutions. One of those tools is regularization.

The Petrov-Galerkin method is used to reduce the inverse problem to a discrete linear inverse problem, by discretising the geometry of the **M4** and applying suitable quadrature rules. Several solving methods are considered to solve this discrete linear inverse problem: direct solvers like the SVD as a way to construct the generalized inverse, and the CGLS method as an iterative solver.

Besides the choice of a numerical solver, the use of regularization has been investigated. We have looked at several standard regularization methods such as Truncated SVD and the application of Tikhonov regularization. Also, the regularizing behavior of the CGLS method is considered.

The performance of the proposed prediction model has been studied. It is shown that the prediction model performs accurate with exact measurement data and noisy measurement data. The effect of regularization by truncation has been demonstrated and it shows that within certain limits the prediction model can be used to do reliable predictions.

A measurement campaign is performed for real data to validate the prediction model. For two different magnetic states and several background fields, we have measured the magnetic field inside the mock-up, and the magnetic signature below the mock-up using the array of sensors in the basement of the facility. The prediction model is demonstrated for a specific measurement setup. It is shown that Tikhonov regularization leads to a reasonable prediction of the magnetic field. However, there are

more steps to make in enhancing the prediction model, so that the performance of the model is also good in practice.

The campaign was a rich source of new insights in regard to the complexity of an accurate prediction model. The inhomogeneity of the background field is not taken into account in the proposed prediction model. Furthermore, we have seen that magnetic sensors are quite sensitive to their orientation. Small changes in the orientation can lead to large variations in the measured values. Such deviations may result in bad performances of the prediction model. Therefore, the prediction model should be enhanced in such a way that it can deal with these issues. Lastly, we have observed that the mobile sensor probably malfunction. Such details must be taken into account in future research.

The performance of the prediction model in practice is demonstrated with a measurement data set obtained during the measurement campaign.

## Nomenclature

Below one can find a list with acronyms and notations used in this thesis. The list is ordered by first appearance in this thesis and per chapter.

### Symbols used in Chapter 1

|                           |   |
|---------------------------|---|
| $\mathcal{E}$             | Electromotive force                                 |
| $\Phi_{\mathbf{B}}$       | Magnetic flux                                       |
| $\mathbf{n}$              | Unit normal vector                                  |
| $\mathbf{B}$              | Magnetic induction field                            |
| $\mathbf{H}$              | Magnetic field                                      |
| $\mu_0$                   | Magnetic permeability in vacuum                     |
| $\mathbf{M}$              | Magnetization of some object                        |
| $\nabla \cdot \mathbf{M}$ | Divergence of the magnetization [A/m <sup>2</sup> ] |
| <b>M4</b>                 | Mock-up for Magnetic Monitoring Measurements        |

### Symbols used in Chapter 2

|                                  |  |
|----------------------------------|--|
| $\mathbf{D}$                     | Electric flux intensity [C/m]                |
| $\rho$                           | Electric charge [C/m <sup>3</sup> ]          |
| $\mathbf{B}$                     | Magnetic induction field in tesla [T]        |
| $\mathbf{E}$                     | Electric field intensity [V/m]               |
| $\mathbf{H}$                     | Magnetic field intensity [A/m]               |
| $\mathbf{J}$                     | Electric current density [A/m <sup>3</sup> ] |
| $\frac{\partial}{\partial t}$    | Time-derivative                              |
| $\nabla \times \mathbf{H}$       | curl of $\mathbf{H}$                         |
| $\mu_0$                          | Magnetic permeability in vacuum              |
| $\Omega$                         | Steel object                                 |
| $\varphi$                        | Magnetic scalar potential                    |
| $\sigma$                         | Magnetic surface charge                      |
| $\mathbf{n}$                     | normal vector w.r.t. $\Omega$                |
| $t$                              | Thickness of $\Omega$                        |
| $\nabla(f)$                      | Gradient of $f$                              |
| $\frac{\partial}{\partial \nu'}$ | Normal derivative                            |
| $E$                              | Set of triangular elements                   |

## Symbols used in Chapter 2, continued

|                   |  |
|-------------------|--|
| $BE$              | Set of boundary elements                                   |
| $P$               | Set of vertices/grid points                                |
| $ X $             | Number of elements in the set $X$                          |
| $f, g, h$         | Magnetic source functions                                  |
| $\partial\Omega$  | Boundary of $\Omega$                                       |
| $\varphi_i$       | basis functions defined on elements in $E$                 |
| $\bar{\varphi}_i$ | basis functions defined on elements in $BE$                |
| $\psi_i$          | basis functions defined on $\mathbb{R}^3 \setminus \Omega$ |

## Symbols used in Chapter 3

|   |  |
|---|--|
| $\ \cdot\ _2$                           | The $L^2$ -norm/Euclidean norm   |
| $\nabla^2$                              | The Laplacian, $\nabla^2 := \nabla \cdot \nabla$                                     |
| $\mathcal{F}$                           | Forward operator   |
| $T$                                     | Linear operator  |
| $\mathcal{N}(T)$                        | Kernel/null-space of the operator $T$  |
| $\inf X$                                | infimum of the set $X$ : largest lower bound of the set $X$                          |
| $\mathcal{L}(\mathcal{X}, \mathcal{Y})$ | The vector space of all bounded linear operators from $\mathcal{X}$ to $\mathcal{Y}$ |
| $\mathcal{D}(T)$                        | Domain of the operator $T$   |
| $\mathcal{R}(T)$                        | Range/image of the operator $T$  |
| $V \oplus W$                            | Direct sum of the spaces $V$ and $W$   |
| $\mathcal{R}(T)^\perp$                  | Orthogonal complement of $\mathcal{R}(T)$  |
| $f \upharpoonright_X$                   | Restriction of the function $f$ to $X$   |
| $T^\dagger$                             | Moore-Penrose generalized inverse of the operator $T$                                |
| $\overline{\mathcal{R}(T)}$             | Topological closure of the space $\mathcal{R}(T)$                                    |
| $T^*$                                   | Adjoint operator of $T$  |
| $x^\dagger$                             | Best-approximated solution   |

### Symbols used in Chapter 4

|                                |   |
|--------------------------------|---|
| $\mathbf{e}$                   | Noise vector  |
| $\kappa(A)$                    | Condition number of the matrix $A$  |
| $\ A\ _2$                      | Euclidean norm of the matrix $A$  |
| $\sigma_{\min}/\sigma_{\max}$  | smallest/largest singular value   |
| $\mathcal{K}_k(A, \mathbf{b})$ | The $k$ -th order Krylov subspace spanned by the matrix $A$ and the vector $\mathbf{b}$ |
| CG                             | Conjugate Gradient Method   |
| CGLS                           | Conjugate Gradient Method for Least Squares   |
| $\Phi$                         | Functional that is used in the CGLS   |
| $\mathbf{r}_k$                 | Residual vector of the $k$ -iterate   |
| $\mathbf{p}_k$                 | Search vectors  |
| $\alpha_{k-1}$                 | Step size in the $k$ -iterate of the CGLS   |
| $\beta_k$                      | Step size in the new search direction $\mathbf{p}_k$                                    |
| $\mathbf{d}_k$                 | Discrepancy of iterate $\mathbf{x}_k$   |

### Symbols used in Chapter 6

|               |   |
|---------------|---|
| $\varepsilon$ | Absolute error between real and predicted signature |
| $\tau$        | Relative error between real and predicted signature |



## Preface

In the period September 2014 until February 2015 I did an internship at TNO on the subject of modeling the magnetic signature of a steel plate. The magnetic signature is defined as the magnetic induction field that is induced by magnetic sources in the steel plate. Together with my supervisor Eugène Lepelaars we described a system that predicted the magnetic signature by a finite number of measurements of the signature. We called this the *simplified magnetic signature monitoring*. Solving an (severely) ill-posed problem is involved in such a system.

This simplified magnetic signature monitoring system is a step towards what we want to achieve on-board of a naval ship. A so-called magnetic signature monitoring system should be able to compute the magnetic induction field based on on-board measurements of the magnetic induction field. Also, the monitoring system should warn the crew on board for critical situations and advice the crew what action should be taken.

Furthermore, a magnetic signature monitoring system should be able to reduce the magnetic induction field effectively by coupling the monitoring system to a degaussing system. A degaussing system is the placement of large coils inside the vessel. By defining suitable currents in these coils the magnetic signature can be reduced. This reduction makes the vessel more magnetic silence.

Of course, the step between a single steel plate and a large complex steel structure such as a steel hull of a naval ship is rather a foolish heroic leap of faith. Therefore a smaller step – constructing a system for some mock-up model – is a more reasonable step to take.

During my internship I became more and more enthusiastic about this particular subject, that I decided to continue the work in the form of a graduation project. Together with Eugne Lepelaars we took the next steps in the realization of such a magnetic signature monitoring system.

We started by designing a mock-up model that represented, in a simplistic manner, the specific shape and complex structure of a naval vessel. (It turned out that this relatively small mock-up model already led us to new challenges which were not visible in the internship.) This model was built in a 3D CAD modeling tool called *Rhino3d*.

This mock-up model was then imported in a multiphysics simulation program called *COMSOL*. Using this program we were able to simulate different scenario's of magnetic induction field surrounding the mock-up model in order to test the implementation in

MATLAB.

We investigated in which way we can achieve the best approximations of the magnetic signature. The goal of the simulations in COMSOL is to analyze and validate the inverse model, and to understand the behavior of the model. Questions on the number of sensors and placement of the sensors are important for future applications of the model.

By financial support of DMO (Defensie Materieel Organisatie) the Marine bedrijf in Den Helder was able to build real life version of the mock-up model for us. A measurement campaign was then set up in order to support our research in the form of real measurement data. This measurement campaign took place at the item range of the WTD71 in Borgstedt, Germany.

## Acknowledgements

I would like to thank my supervisors Marleen Keijzer (TUD) and Eugène Lepelaars (TNO) for their pleasant support throughout my graduation period. The (many) meetings we had were very pleasant and fun. They gave me a lot of freedom and opportunities to grow during the graduation project, which was inspiring.

Furthermore I thank the colleagues associated with TNO for their support during my graduation project. In particular I thank my roommate Henry Veerman, for the pleasant time and conversations. Also I thank K.P. Hart (TUD) for reviewing Chapter 3 of this report.

Lastly I thank DMO, CSSM (Centre for Ship Signature Management) and WTD 71 (Wehrtechnische Dienststelle für Schiffe und Marinewaffen der Bundeswehr, Maritime Technologie und Forschung) for their financial support and for making it possible to perform a measurement campaign in Bünsdorf, Germany.



# Contents

|                         |  |             |
|-------------------------|--|-------------|
| <b>Abstract</b>         | .....  | <b>i</b>    |
| <b>Nomenclature</b>     | .....  | <b>iii</b>  |
| <b>Preface</b>          | .....  | <b>vii</b>  |
| <b>Acknowledgements</b> | .....  | <b>ix</b>   |
| <b>List of Figures</b>  | .....  | <b>xvii</b> |
| <b>1</b>                | <b>Introduction</b> .....                                    | <b>1</b>    |
| 1.1                     | Motivation .....   | 1           |
| 1.1.1                   | The signature of a naval vessel .....                        | 2           |
| 1.1.2                   | The magnetic signature .....                                 | 4           |
| 1.2                     | The magnetic naval mine .....                                | 6           |
| 1.2.1                   | The very first naval mine .....                              | 6           |
| 1.2.2                   | From contact mines to influence mines .....                  | 7           |
| 1.2.3                   | The modern influence mine .....                              | 8           |
| 1.3                     | Previous work .....  | 9           |
| 1.4                     | Research goals .....   | 10          |
| 1.5                     | Chapter outline .....  | 11          |
| 1.6                     | Software .....   | 12          |
| <b>2</b>                | <b>Model formulation</b> .....                               | <b>13</b>   |
| 2.1                     | Maxwell's Equation .....                                     | 13          |
| 2.2                     | Forward Problem .....  | 14          |
| 2.2.1                   | Solving Poission's equation .....                            | 14          |
| 2.3                     | Approximation of forward problem solutions .....             | 15          |
| 2.4                     | Derivation of the inverse problem .....                      | 17          |
| 2.4.1                   | Petrov-Galerkin Expansion Method .....                       | 17          |
| 2.4.1.1                 | Expansion of functions .....                                 | 18          |
| 2.4.1.2                 | Orthogonality condition .....                                | 19          |
| 2.4.2                   | Construction of basis functions $\psi_i$ .....               | 21          |
| 2.4.3                   | Construction of basis functions $\varphi_i$ .....            | 21          |
| 2.4.4                   | Construction of basis functions $\bar{\varphi}_i$ .....      | 22          |
| 2.4.5                   | Approximation of the matrix entries $\mathbf{a}_{ij}$ .....  | 23          |
| 2.4.6                   | Continuity of inverse solutions and number of unknowns ..... | 25          |

|          |   |           |
|----------|---|-----------|
| 2.5      | Prediction model . . . . .  | 26        |
| 2.6      | Remarks . . . . .   | 26        |
| 2.6.1    | Non-uniqueness of the inverse problem . . . . .   | 26        |
| 2.6.2    | Different approach . . . . .  | 27        |
| <b>3</b> | <b>Inverse Modeling Theory . . . . .</b>  | <b>29</b> |
| 3.1      | Introduction . . . . .  | 29        |
| 3.2      | Introduction to the Forward . . . . .   | 30        |
| 3.2.1    | Smoothing properties of integral equations . . . . .  | 32        |
| 3.2.2    | General formulation . . . . .   | 32        |
| 3.3      | Hadamard's well-posed problem . . . . .   | 33        |
| 3.3.1    | When a solution does not exist . . . . .  | 34        |
| 3.3.2    | When a problem is not one-to-one . . . . .  | 34        |
| 3.3.3    | When the solution of an inverse problem does not depend continuously on the<br>data . . . . . | 35        |
| 3.4      | Generalized inverse . . . . .   | 36        |
| 3.4.1    | Least-squares and best-approximate solutions . . . . .  | 36        |
| 3.4.2    | Restriction of $T$ . . . . .  | 36        |
| 3.4.3    | Generalized Inverse . . . . .   | 37        |
| 3.4.4    | Generalized inverse as a projection . . . . .   | 38        |
| 3.4.5    | The generalized inverse yields the best-approximate solution . . . . .                        | 38        |
| 3.4.6    | The generalized inverse and ill-posedness . . . . .   | 40        |
| 3.4.7    | Remark on using the generalized inverse as a best-approximate solution . . . . .              | 41        |
| 3.5      | Construction of the generalized inverse for finite-dimensional compact operators . . . . .    | 42        |
| 3.6      | Ill-posed inverse problem . . . . .   | 43        |
| 3.6.1    | Finite-dimensional inverse problem . . . . .  | 43        |
| 3.6.2    | Proof of the claim . . . . .  | 43        |
| <b>4</b> | <b>Regularization Methods and Numerical Solvers . . . . .</b>                                 | <b>47</b> |
| 4.1      | Why do we need regularization? . . . . .  | 48        |
| 4.2      | Standard Regularization methods . . . . .   | 49        |
| 4.3      | Truncated SVD . . . . .   | 50        |
| 4.4      | Tikhonov Regularization . . . . .   | 51        |
| 4.4.1    | General form . . . . .  | 52        |
| 4.4.2    | L-curve method to find $\lambda$ . . . . .  | 53        |
| 4.4.3    | Writing the minimization in a different form . . . . .  | 53        |
| 4.4.4    | Tikhonov when $L = I$ . . . . .   | 54        |
| 4.5      | Numerical Solvers: direct methods . . . . .   | 55        |
| 4.5.1    | QR-decomposition for least-squares problems . . . . .   | 56        |
| 4.6      | Numerical Solvers: iterative methods . . . . .  | 57        |
| 4.6.1    | Krylov-subspace iterative methods . . . . .   | 57        |

|          |  |           |
|----------|--|-----------|
| 4.7      | CGLS method  | 59        |
| 4.7.1    | Residual error   | 59        |
| 4.7.2    | Sequential linear searches   | 59        |
| 4.7.3    | The value of stepsize $\alpha_{k-1}$                                     | 60        |
| 4.7.4    | New search direction $\mathbf{p}_k$                                      | 61        |
| 4.7.5    | Simplification of the expression for $\alpha$                            | 61        |
| 4.7.6    | The value of $\beta_k$   | 62        |
| 4.7.7    | Properties of $\mathbf{x}_k$ and $\mathbf{d}_k$                          | 63        |
| 4.7.8    | The CGLS method algorithm  | 63        |
| 4.8      | Regularization properties of the CGLS method                             | 64        |
| <b>5</b> | <b>Application/Test case</b>   | <b>67</b> |
| 5.1      | Mock-up  | 67        |
| 5.1.1    | Real version of the <b>M4</b>  | 68        |
| 5.1.2    | Simplifications in the CAD-model   | 68        |
| 5.1.3    | Properties of the steel used   | 69        |
| 5.1.4    | Meshing of the mock-up   | 69        |
| 5.2      | Introduction to COMSOL   | 70        |
| 5.2.1    | Computation of the (reduced) magnetic field and magnetic shielding       | 71        |
| <b>6</b> | <b>Validation and analysis of the prediction model</b>                   | <b>75</b> |
| 6.1      | Introduction to the CIFV process   | 76        |
| 6.1.1    | Relative and absolute errors   | 76        |
| 6.1.2    | Meshing  | 77        |
| 6.2      | Simulation: uniform background field along the $\mathbf{u}_x$ -direction | 79        |
| 6.2.1    | Results of <b>CIFV</b> routines  | 79        |
| 6.3      | Investigation of behavior of the prediction model                        | 84        |
| 6.3.1    | Direct solvers   | 84        |
| 6.3.2    | SVD analysis   | 86        |
| 6.3.3    | CGLS and SVD+Tikh simulations  | 88        |
| 6.3.4    | Anomalies in the prediction model  | 88        |
| 6.4      | Double Layer Component in the Magnetic Field Formulation                 | 88        |
| 6.4.1    | Changing the prediction model  | 89        |
| 6.4.2    | Results neglecting the double layer component                            | 89        |
| 6.5      | Noisy Measurements and the use of Regularization                         | 92        |
| 6.5.1    | Modeling of noise  | 92        |
| 6.5.2    | A remark on independency in the modeling of noise                        | 93        |
| 6.5.3    | Numerical tests  | 93        |

|                   |   |            |
|-------------------|---|------------|
| <b>7</b>          | <b>Measurement Campaign and application of Prediction Model</b> | <b>95</b>  |
| 7.1               | Measurement Campaign  | 95         |
| 7.1.1             | Campaign plan   | 96         |
| 7.1.1.1           | Helmholtz coil  | 96         |
| 7.1.1.2           | Deperming   | 97         |
| 7.1.1.3           | Permstate I   | 97         |
| 7.1.1.4           | Remark on the positioning of the mobile sensor                  | 97         |
| 7.1.1.5           | A remark on measuring the magnetic signature                    | 98         |
| 7.1.1.6           | Hysteresis Modeling   | 98         |
| 7.1.1.7           | Change the permstate of the <b>M4</b>                           | 98         |
| 7.1.1.8           | Permstate II  | 99         |
| 7.1.1.9           | Schedule  | 99         |
| 7.2               | Observations during the campaign                                | 101        |
| 7.2.1             | Inhomogeneity of the background field                           | 101        |
| 7.2.2             | Manual measurements   | 102        |
| 7.2.2.1           | Orientation of the sensor                                       | 103        |
| 7.3               | Results   | 104        |
| 7.3.1             | Demonstration of the prediction model on the measurement data   | 106        |
| <b>8</b>          | <b>Conclusion and Further Research</b>                          | <b>109</b> |
| 8.1               | Results   | 109        |
| 8.1.1             | Performance of the prediction model                             | 109        |
| 8.1.2             | Reducing the influence of noise in measurements on performance  | 109        |
| 8.1.3             | Demonstration of the prediction model on real measurement data  | 110        |
| 8.2               | Future research   | 111        |
| 8.2.1             | Bayesian interference and techniques from Bayesian statistics   | 111        |
| 8.2.2             | Advanced regularization methods                                 | 112        |
| 8.2.3             | Inhomogeneity of the background field                           | 113        |
| 8.2.4             | Use of sensors in magnetic signature monitoring                 | 113        |
| 8.2.5             | The magnetic field measured in closed spaces                    | 113        |
| 8.2.6             | Reducing the number of measurements                             | 114        |
| 8.2.7             | Reducing the complexity of the geometry                         | 114        |
| 8.2.8             | Double layer component  | 114        |
| <b>Appendices</b> |   |            |
| <b>A</b>          | <b>Tables</b>   |            |
| <b>B</b>          | <b>Fundamental Solution of the Laplace Equation</b>             |            |
| B.1               | Introduction  | 121        |
| B.2               | Computation of the fundamental solution                         | 121        |
| <b>C</b>          | <b>Double layer potential</b>                                   |            |

|          |   |     |
|----------|---|-----|
| C.1      | Further derivation of the potential expression of the Poisson problem . . . . . | 123 |
| C.2      | Approximation of the double layer expression for $B^\perp$ . . . . .            | 125 |
| C.3      | Interpretation of the double layer potential . . . . .                          | 127 |
| <b>D</b> | <b>Quadrature Rules</b>   |     |
| D.1      | Quadrature rules for generic triangular elements . . . . .                      | 129 |
| D.2      | Quadrature rule for line integrals over generic boundary elements . . . . .     | 131 |
| D.3      | Tables of the quadrature rules . . . . .  | 131 |
| <b>E</b> | <b>Expression of the magnetic field for uniform magnetized steel plates</b>     |     |
| <b>F</b> | <b>Development of the M4</b>  |     |



## List of Figures

- 1.1 Zr. Ms. Vlaardingen (M863) 1
- 1.2 Overview signatures 2
- 1.3 Multi-purpose frigate Zr.Ms. Van Speijk (F828) 3
- 1.4 Beer keg mine 6
- 1.5 Dip needle mine 7
- 1.6 A multi-influence shallow water sea mine 8
- 1.7 Earth Field Simulator 11
  
- 2.1 Partitioning of a rectangle 18
- 2.2 Triangle transformation 21
- 2.3 Boundary line element transformation. 22
- 2.4 Reduction of unknowns 25
- 2.5 Simple flow chart of the prediction model. 26
  
- 3.1 Forward Problem 30
- 3.2 Inverse Problem 31
- 3.3 Projection of  $\bar{z}$  onto  $\mathcal{N}(T)$  40
  
- 4.1  $L$ -curve example in the CGLS method 65
  
- 5.1 An example of a model created in `Rhinoceros` 67
- 5.2 The real **M4** 68
- 5.3 Example of the meshing of the mock-up. 69
- 5.4 Magnetic field in `COMSOL` 70
  
- 6.1 Flow chart of the CIFV routine. 78
- 6.2 The relative and absolute errors of the CGLS predicted signature. 80
- 6.3 The CGLS predicted and `COMSOL` magnetic signature. 81
- 6.4 The magnetic sources  $f$ ,  $g$  and  $h$  in the **M4**, computed by the inverse problem. 82
- 6.5 The  $L$ -curve in loglog-scale corresponding to the system  $A\mathbf{x} = \mathbf{b}$  83
- 6.6 Source solutions computed via the SVD method 84
- 6.7 Predicted magnetic signature computed via the SVD method 85
- 6.8 Mesh IV, defined on the mock-up. 86

- 6.9 The singular values and the SVD components of the inverse problem. 87
- 6.10 Prediction results without double layer component 90
- 6.11 Noise investigation 94
  
- 7.1 A schematic drawing of a Helmholtz coil 96
- 7.2 A grid, painted on the inside of the mock-up, that is used to do accurate on-board measurements. 98
- 7.3 Measuring the inhomogeneity of the background field 101
- 7.4 Orientation of sensor in experimental setup 103
- 7.5 Intensity of the magnetic signature of the **M4** at Bünsdorf. 104
- 7.6 Field components of the magnetic signature of the **M4** at Bünsdorf 105
- 7.7 The  $L$ -curve used to choose the regularization parameter of the Tikhonov regularization method 106
- 7.8 The magnetic sources  $f$ ,  $g$  and  $h$  in the **M4**, computed by the inverse problem. 107
- 7.9 Field components of the magnetic signature at Bünsdorf 108
  
- C.1 Boundaries  $\partial\Omega_1$  and  $\partial\Omega_2$  of the plate. 124
- C.2 The projection of  $\Omega$  onto the  $x, y$ -axis leads to a two-dimensional plate with an one-dimensional boundary. 125
- C.3 Two parallel surface  $S_1$  and  $S_2$  with magnetic charge densities  $\rho_1$  and  $\rho_2$ . 127
  
- D.1 Triangle transformation 129
  
- E.1 A steel plate 136
  
- F.1 Development of the **M4**. © Jan Sijs 139

# 1 Introduction

## 1.1 Motivation

The Royal Netherlands Navy operates often in areas where the threat of naval mines is high. Such fields of naval mines can be found near the coast of a country or in shallow waters. The presence of mines influences the probability of mission success and therefore any risk of detonation of a naval mine must be avoided .

One of the tasks of the Royal Netherlands Navy is the disarming of the naval mines in the North sea and near the Dutch coast to secure shipping routes. At this moment, there is an estimated number of 250.000 naval mines in the earths waters. This number shows the need of clearing these bombs. To succeed this task, two kinds of naval vessels can be used. The so-called *mine hunters* are naval vessels that use special drones to disarm naval mines without detonating them, while *minesweepers* are used to disarm naval mines by detonating the naval mines. In both cases the vessels may come in range of the mines.

At this moment the Royal Netherlands Navy has a total of six mine hunters and no mine sweepers. In figure 1.1 one can find a picture of the mine hunter Zr. Ms. Vlaardingen (M863). This mine hunter is approximately 51.5 meters long, 8.9 meters wide and has the possibility to use mine clearance divers as well as the mine identification and disposal system SPVDS, which is an unmanned underwater vehicle (UUV).



Figure 1.1: Zr. Ms. Vlaardingen (M863), source: <https://www.defensie.nl/>

A modern influence mine uses all kinds of sensors to measure signals in order to determine whether a vessel is near. If indeed a naval vessel is near, an influence mine can decide to actuate. Some of these signals are the following:

- A **magnetic field** around a vessel that locally disturbs the earth magnetic field. This disturbance is caused by the ferromagnetic material in the construction of the vessel.
- An **electric field** is partially caused by on board equipment that work on electricity. Also the movement of the vessel in a background field generates an electrical field. The main cause however is the cathodic protection of the hull: using electricity to avoid corrosion of the vessel's hull. A current along the vessel's hull induces also a contribution to the magnetic field that surrounds the vessel.

In figure 1.2 several other signals are mentioned in a simple overview. Notice that some of the signals are only of interest above sea level, while other signals play a larger role below sea level.

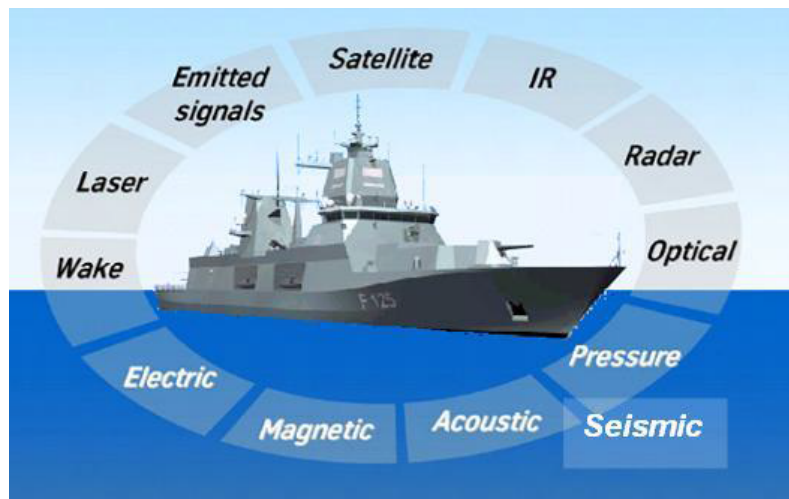


Figure 1.2: An overview of signals that a naval vessel emits. Source: CSSM

### 1.1.1 The signature of a naval vessel

It is important to know how these signals propagate and to be able to minimize and manipulate the signals as much as possible. These signals depend uniquely on the naval vessel. Therefore we define the **signature** of a naval vessel as the complete “picture” of the propagation of these signals in its environment. We speak of the **magnetic signature** when we consider the magnetic field of a specific naval vessel. The reduction of these signals improves the probability of a mission success of a naval vessel.

The Netherlands Organization for Applied Scientific Research (TNO) is doing research in describing these signatures of a naval vessel. This research is done for the Ministry of Defense. TNO focuses mainly on the underwater signatures such as

the magnetic signature, electric signature and acoustic signatures and above water ship signatures such as IR and RCS signatures.

In figure (1.3) one can find the Zr.Ms. Van Speijk (F828) multi-purpose frigate. The Royal Netherlands Navy has the ambition to equip future naval vessels with a so-called **signature monitoring system**. This system should visualize the signature of different influences. To reduce the signatures of a vessel, the signature monitoring system has to be coupled to some control system that minimizes the signals. Such a system is then called a **signature management system**. During a mission the signature management system should also warn and give advice if the threat level becomes critical.

With a so-called degaussing system the magnetic field around the naval vessel can be reduced. By placing large coils in a ship's hull (in all three directions) the degaussing system is able to generate a magnetic field. Such a magnetic field is then used to reduce the magnetic induction field around a vessel. An extensive explanation of these systems can be found in [15].

The ultimate task is to complete the creation of a *closed-loop degaussing system*. This is essentially the connection between the signature monitoring system and the degaussing system (and thus a crucial module in the signature management system). By using the magnetic signature from the signature monitoring system the degaussing system can operate optimally.



Figure 1.3: Multi-purpose frigate Zr.Ms. Van Speijk (F828). Source: <http://www.defensie.nl>

### 1.1.2 The magnetic signature

In this report we consider the magnetic signature of a naval vessel. The *magnetic signature* is distortion of the earth's magnetic field due to the naval vessel. This distortion can be sensed by a naval mine.

The magnetic signature of a vessel is mainly caused by the following four contributions:

- (1) The **interaction** between the steel ship structure and the static earth's magnetic field;
- (2) The use of **cathodic protection** to control the corrosion of the metal surface of a naval vessel;
- (3) **Eddy currents** in the vessel's hull by the motion of the vessel in the earth magnetic field;
- (4) **Stray fields** generated by electrical equipment and cabling inside the vessel.

We limit ourselves to the first contribution, the interaction between the steel ship construction and the earth's magnetic field. The interaction of the earth background field and the steel construction of a vessel is described by the Maxwell equations. The ship structure is made out of welded steel plates. Because of the ferromagnetic behavior of steel, the steel plates magnetize in the presence of the earth magnetic field. Together with the permanent magnetization of the steel, this is a significant contribution to the magnetic signature.

Steel has the following complex magnetic behavior:

- **Hysteresis:** the *magnetic memory* of steel constantly changes the properties of the steel. The changes are due to a present background field. The way how the steel magnetizes thus changes over time. This complex behavior can be expressed by a so-called *hysteresis* curve that shows how the magnetization of the steel is in relation to the background field.
- **Magneto-Mechanical effects:** The behavior and properties of steel change due to mechanical stress. Examples of mechanical stress are bending/welding of steel plates and damage to the vessel's hull due to military weapons. For submarines the different effect plays an important role. As the pressure on the submarine pressure hull rises when a submarine is deep below sea level, the hysteresis curve of the steel hull changes significantly. These effects are called the Villari effects. Descriptions of these effects are quite complex.
- **Inhomogeneous magnetization:** Zooming in onto a steel plate leads to the visibility of so-called magnetic domains. In each domain the magnetization is uniform, but these magnetic domains vary in shape and cover the steel plate quite randomly. Therefore the magnetization of a steel plate is inhomogeneous. When a background field changes, the shape of these magnetic domains changes as well, and therefore changing the magnetization of steel.

The magnetisation cannot be measured directly. This makes the notion of a magnetisation hard to grasp. We see that it is complicated to model the magnetic field surrounding a vessel when we want to take into account all these complex properties. In this project, however, we are not interested in the causes of the magnetisation, only in the resulting magnetic field. We will use measurements of the magnetic field and inverse modeling, to reconstruct the total magnetisation.

## 1.2 The magnetic naval mine

The following is an excerpt of chapter 3 in [13]. A summary is given of the history of the naval mine and the mechanics behind the magnetic naval mine. It will become clear why there is a need of precise magnetic signature computations for future naval vessels.

### 1.2.1 The very first naval mine

The naval mine was first invented by David Bushnell during the American Revolutionary War in the eighteenth century. This primitive mine, if one could speak of a “mine” at all, was in principle a tar covered beer keg filled with gunpowder. The tar was necessary to make the keg waterproof. the wood lets the kegs float on water.

The detonation was based on a flintlock mechanism that hopefully got triggered when the beer keg made contact with a ship’s hull. This type of mine is called a *contact mine*. These contact mines were obviously unreliable as the trigger mechanism would not always work properly. Furthermore, the gunpowder could get wet so that the mine could not work at all. Yet it was a brilliant first step to the modern naval mines. An illustration of such a typical beer keg mine can be found in figure 1.4.

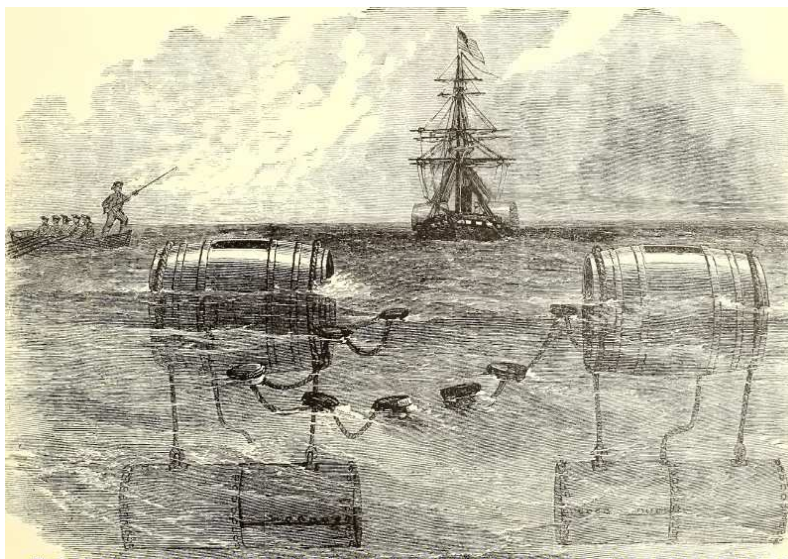


Figure 1.4: Beer keg mines in the 18th century. [13]

After the American Revolutionary War, further development of contact mines led to a reliable detonation mechanism based on pressure/touch. The flintlock mechanism was replaced by the typical pins.

A pin was “made out of a soft lead that covered a glass vile filled with an electrolyte”. When a pin contacted the ship’s hull, the glass would break and the electrolyte would flow between two contacts so that a closed circuit was formed. This then led to the detonation of the mine.

The contact mines had a spherical shape, with the typical pins on top of the sphere, and were held in place by an anchor below the water surface in such a way that the mines were out of sight of the human eye, but in reach of the vessel's hull. This type of naval mine was used excessively in the first World War. They were moored throughout the waters of Europe and the North sea. It appeared to be an effective device to defend against submarines.

## 1.2.2 From contact mines to influence mines

After World War I, Germany started the development of mines that are actuated not by contact, but rather by influence fields from ships, such as magnetic fields and electric fields. Germany developed a bottom influence mine that lies on the sea floor and explodes when it detect a ship's magnetic field by its distortion of the background field.

In figure 1.5, one can see the typical detonation mechanism. A dip-needle, which is also used in a simple compass, reacts on the change from the background field when a ship is nearby, and closes a circuit when the change was significant enough. This simple idea is rather brilliant. Without any modern technology they were able to build a sensor that was rather cheap and worked very well. These mines were used extensively during World War II.

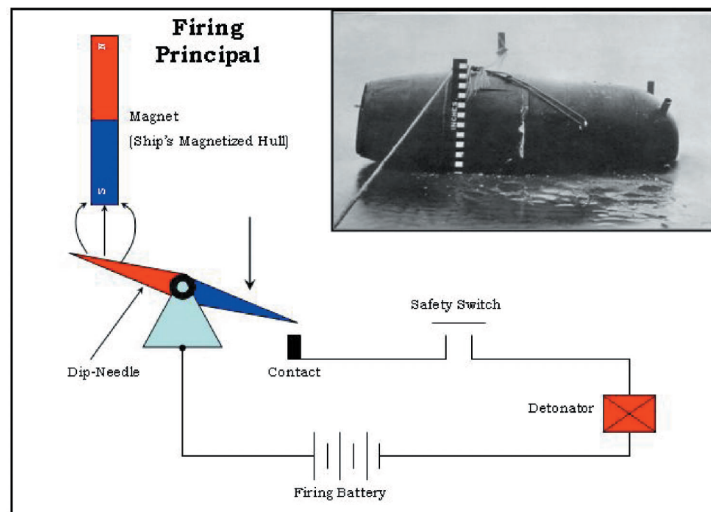


Figure 1.5: Schematic of a dip needle firing circuit in a magnetic bottom mine used in World War II. [13]

The U.S. took a different approach in the development of a magnetic mine. Their magnetic mine sensor was not based on a dip-needle but rather on Faraday's law of induction. Given a closed circuit  $C$  which encloses an open surface  $S$ , Faraday's law of induction is expressed by the following formula

$$\mathcal{E} = -\frac{d\Phi_{\mathbf{B}}}{dt}$$

where  $\mathcal{E}$  is the electromotive force (EMF) and  $\Phi_B$  is the magnetic flux defined by

$$\Phi_B = \int_S \mathbf{n} \cdot \mathbf{B} \, dA$$

This law states that when there is a magnetic field surrounding the circuit that rapidly changes over time, then there is a current in the circuit produced by this varying magnetic field. The intensity of this current is related to the change in the magnetic flux. Hence when a magnet moves through the circuit, a current runs inside the circuit.

This is the idea used in the magnetic mine sensor of the U.S. In the detonation circuit there is a sensitive relay that is powered by another circuit. In this second circuit a current is induced when a ship changes the background field. When the change of the magnetic field is large enough, the sensitive relay closes the detonation circuit which actuates the naval mine.

### 1.2.3 The modern influence mine

The modern naval mine does not only sense variations in the earth magnetic field, but also the other influences as described before. By combining the measurements of the magnetic and electric fields, acoustic and pressure waves, a smart algorithm in such a naval mine determines whether a naval vessel is passing by and if actuation of the mine will lead to maximum damage. As the power source on such a mine is limited, the mine should be built in such a way that it minimizes the usage of energy. Therefore, not all sensors are active at all time. A managing system controls the use of sensors and switches between the various sensors available in the mine, which makes the protection against such naval mines complicated. At one time the naval mine mainly senses the magnetic field, while at some other instance the mine may sense acoustic and pressure waves.



Figure 1.6: A multi-influence shallow water sea mine, designed to be effective against landing crafts and small-mid tonnage vessels. source: <http://www.aiad.it/>

### 1.3 Previous work

During the internship we have worked on the first steps of magnetic signature monitoring. We investigated how one sets up the framework for the connection between the magnetic sources in a single steel plate and the magnetic field that is induced by it. Starting with assumptions for the vector fields considered, we are left with the following set of equations that describes the connection between the magnetization  $\mathbf{M}$  of a plate  $\mathcal{P}$  and the magnetic induction field  $\mathbf{B}$ :

$$\begin{cases} \nabla \times \mathbf{H} = \mathbf{0} \\ \nabla \cdot \mathbf{B} = 0 \\ \mathbf{B} = \mu_0(\mathbf{H} + \mathbf{M}) \end{cases}$$

Here,  $\mu_0$  is the magnetic permeability in vacuum and  $\mathbf{H}$  is the magnetic field. An analytical solution to the forward problem is given by

$$\mathbf{B}(\mathbf{r}) = -\frac{\mu_0 t}{4\pi} \iint_{\mathcal{P}} \frac{\mathbf{r} - \mathbf{r}'}{|\mathbf{r} - \mathbf{r}'|^3} \nabla \cdot \mathbf{M}(\mathbf{r}') d\mathbf{r}', \quad \mathbf{r} \notin \mathcal{P}$$

Note that  $\nabla \cdot \mathbf{M}$  is the source of the field. The thickness of the plate is given by  $t$ . After using an appropriate discretisation of plate  $\mathcal{P}$ , the above integral can be approximated using *quadrature rules*. The forward problem was then implemented in `MATLAB`.

A validation of the implementation was done. In the case of a uniform magnetization of the single steel plate we compared the results of the simulation in `MATLAB` together with analytical expressions.

Next, we considered the inverse problem for a single steel plate. The inverse problem can be stated heuristically in the following manner: Given  $N$  measurements of some magnetic induction field  $\mathbf{B}$  which is induced by a magnetization of the steel plate  $\mathcal{P}$ , reconstruct the source  $f$  such that the following equation holds in each measurement  $\mathbf{B}(\mathbf{r}_i)$ :

$$\mathbf{B}(\mathbf{r}_i) = -\frac{\mu_0 t}{4\pi} \iint_{\mathcal{P}} \frac{\mathbf{r}_i - \mathbf{r}'}{|\mathbf{r}_i - \mathbf{r}'|^3} f(\mathbf{r}') d\mathbf{r}', \quad \text{for } i = 1, 2, \dots, N$$

It appeared at the beginning of this graduation project that a few programming errors and a few small errors in the derivation of the forward problem had been made. These mathematical mistakes weren't visible because of the simple geometry. The mistakes have been corrected.

In the years 2000-2008 Chadebec et al. worked on the Inverse Magnetostatic Problem. They derived an inverse problem for the magnetization  $\mathbf{M}$  of some steel object, rather than the magnetic sources  $\nabla \cdot \mathbf{M}$  as in the internship. Although they achieved a lot of progress in their research, it seemed that it stagnated at some point.

## 1.4 Research goals

The aim of this project is to create a prediction model for the magnetic signature monitoring of a naval vessel, based on a mathematical-physical model. One part of this model is the construction of the total magnetic signature of a naval vessel from limited on-board measurements of the magnetic signature. In this thesis we focus on the development of this model and we call this the *prediction model*. The prediction model will be part of a larger numerical system that will be developed in the near future. Therefore some of the research goals in this thesis are shared by other projects within TNO.

To realize an actual magnetic signature monitoring system in a naval vessel, we should keep in mind that a naval ship is a (very) complex ship where the placement of sensors for the magnetic signature monitoring system should be optimal to achieve our goals.

It is already a challenge to determine the best positioning of sensors inside a naval vessel, keeping in mind all electrical machines on board of a vessel that create local distortions of the magnetic field. Furthermore we would like to know which kind of sensors are needed (in particular the required *accuracy* of the sensor) and how many sensors are needed in order to have an adequate magnetic signature monitoring system. Some of these questions are challenges for the near future, when actual measurement campaigns on large ships will be conducted.

Specifically, we want to design a model that predicts the magnetic signature from a limited number of on-board measurements of the magnetic field. Topics we will consider are:

- Determine a correct formulation of this prediction model.
- Analyze the inverse problem and study regularization methods.
- Use simulated data to investigate whether the model can predict accurately.
- Analyse the influence of noise in the measurement data with respect to the solutions of the inverse problem.
- Apply the prediction model to real on-board measurement data.

The required accuracy of the prediction model is classified. As a rule of thumb the relative errors between the predicted magnetic signature and the real magnetic signature of a vessel should not exceed the 10%. We use this as a guideline in the validation of the prediction model. Techniques from the field of *regularization* are investigated in order to enhance the prediction model.

To validate whether the prediction model works accurately in practice, a measurement campaign is organized. A mock-up model called the **M4** (which stands for the “Mock-up for Magnetic Monitoring Measurements”) is built by the Marine Bedrijf in

Den Helder and is transported to the item range “Grosse Eva” at the WTD71 in Borgstedt, Germany. A picture of the **M4** is found in figure 5.2.

The Grosse Eva is a dry magnetic measurement facility that consists of two systems of coils and a measurement setup made out of magnetic flux-gate sensors. The larger coil system is used to simulate any background field on earth. For instance, it is possible to simulate the earth’s magnetic field near the coast of Aruba. The second smaller coil system is used to change the magnetic state of the **M4**. This is done by placing the **M4** in a very strong changing magnetic field. A much larger measurement facility lies near the Grosse Eva and can be used to measure the magnetic signature of large vessels, such as submarines. This facility is called the “earth Field Simulator”. In figure 1.7 a picture of the earth Field Simulator can be found.

The measurement campaign took place in October 2015. For one measurement we have processed the data. This data set is used as input for the prediction model. Further processing of the data and validation will be done in the near future.



Figure 1.7: Earth Field Simulator. source: baainbw.de/WTD 71

## 1.5 Chapter outline

This report is structured as follows. In Chapter 2 we formulate our problem in terms of a so-called Forward and Inverse problem. We show that the application of the Galerkin-Petrov Method leads to a linear inverse problem. In Chapter 3 we give an overview of inverse modeling. We discuss the elementary notion of inverse problems and describe what a generalized inverse is. Furthermore, we prove that our inverse problem is ill-posed. In Chapter 4 we present an introduction to regularization methods and the use of (iterative) solvers to approximate solutions (for linear systems). Several solvers are discussed. In particular we discuss the Conjugate Gradient

Method for Least Squares (CGLS) as well. The regularizing properties of the CGLS method are presented as well. In Chapter 5 we discuss the geometries that we use in our simulations. In particular we discuss the mock-up model **M4**. A brief explanation on the meshing of our mock-up is then given. In addition, the multiphysics program COMSOL is introduced and we show how COMSOL computes magnetic fields. In Chapter 6 we test our inverse model and investigate its behavior in detail. In Chapter 7 we discuss the measurement campaign and the observations that are done during the campaign. Chapter 7 ends with the demonstration of the prediction model on real measurement data. In Chapter 8 we discuss the results obtained in this project and we discuss further research directions for the near future.

## 1.6 Software

Throughout this project we have used several software packages. The multiphysics software COMSOL is used to create several meshes of the mock-up and to generate data for validation of our prediction model. For the development of our mock-up model we have used Rhino to build the CAD-model that is necessary as an input geometry in COMSOL.

MATLAB has been used for the implementation of the forward problem, inverse problem and the prediction model. We used MATLAB to test several numerical solvers, regularization methods and for the validations of our inverse model.

The MATLAB toolbox called *Regularization Tools*, created by Per Christian Hansen, has been used for the investigation and implementation of regularization methods in our model. In particular the algorithms `cgl_s.m` and `csvd.m` have been used extensively in our research, as well as the implementations for Tikhonov regularization and the L-curve plot.

## 2 Model formulation

In this chapter we start with the formulation of two problems that are used in the construction of our prediction model, namely the forward and inverse formulation. The forward problem is derived from the Maxwell's equations and the inverse problem follows from the forward problem.

After the computation and approximation of solutions of the forward problem we use these expressions as a start of the formulation of the inverse problem. Together with the forward formulation we can define the prediction model.

### 2.1 Maxwell's Equation

In the late 1800s the knowledge of electric and magnetic fields was summarized by Maxwell's equations:

|  |  |
|--|--|
| $\nabla \cdot \mathbf{D} = \rho$   | <b>Gauss' law:</b> electrical fields are produced by electrical charges                |
| $\nabla \cdot \mathbf{B} = 0$  | <b>Gauss' law:</b> there exist no magnetic monopoles                                   |
| $\nabla \times \mathbf{E} = -\frac{\partial \mathbf{B}}{\partial t}$             | <b>Faraday's law of induction:</b> changing magnetic fields produce electric fields    |
| $\nabla \times \mathbf{H} = \frac{\partial \mathbf{D}}{\partial t} + \mathbf{J}$ | <b>Ampère's law:</b> magnetic fields result from currents and changing electric fields |

In these equations  $\mathbf{E}$  stands for the electric field intensity [V/m] and  $\mathbf{H}$  stands for the magnetic field intensity [A/m]. The quantities  $\mathbf{D}$  and  $\mathbf{B}$  stand for the electric and magnetic flux densities respectively. The units of these quantities are [C/m<sup>2</sup>] and [T] respectively. The magnetic flux density may also be called the magnetic induction field. The electric charge density [coulomb/m<sup>3</sup>] is given by  $\rho$  and  $\mathbf{J}$  stands for the electric current density measured in [A/m<sup>2</sup>].

We see that in general the electric and magnetic fields are coupled by the above equations. We therefore speak of the electromagnetic field. When we assume that the fields are **static**, i.e., the fields do not change in time, then the four equations decouple into two sets of two equations that describe the electric field and the magnetic field. Assuming that there are no currents present ( $\mathbf{J} \equiv \mathbf{0}$ ), the *static magnetic field* is described by

$$\begin{aligned}\nabla \cdot \mathbf{B} &= 0 \\ \nabla \times \mathbf{H} &= \mathbf{0}\end{aligned}$$

## 2.2 Forward Problem

In this section we derive and solve the forward problem. The forward problem is the determination of the magnetic induction field  $\mathbf{B}$  that is produced by some *known* magnetization  $\mathbf{M}$  in a steel object  $\Omega$ . In this thesis a steel object is made out of steel plates of the same thickness  $t$ . Furthermore we assume that the thickness is relatively small compared to the other dimensions of the steel, which implies that a magnetization of a steel plate is uniform in  $t$ . Therefore we may assume that the steel plate consists of two-dimensional surfaces and the thickness  $t$  of the steel plates is a constant value in the formulation.

The set of PDE's that describes that *static magnetic field* generated by some magnetization in an volume object  $\Omega$  is given by the following system of equations:

$$\begin{cases} \nabla \times \mathbf{H} = \mathbf{0} & \text{(Ampère's law)} \\ \nabla \cdot \mathbf{B} = 0 & \text{(Gauss' law)} \\ \mathbf{B} = \mu_0(\mathbf{H} + \mathbf{M}) & \text{(Constitutive law)} \end{cases}$$

Here,  $\mu_0$  is the magnetic permeability in vacuum:  $\mu_0 = 4\pi \cdot 10^{-7} T \cdot m/A$ . Note that a magnetization  $\mathbf{M}$  only lives on the objects  $\Omega$ . Because  $\nabla \times \mathbf{H} = \mathbf{0}$  it follows from the Hodge decomposition theory that there is a magnetic scalar potential  $\varphi$  such that  $\mathbf{H} = -\nabla\varphi$ . From the above set of equations we can derive the following Poisson equation:

$$\Delta\varphi = \nabla \cdot \mathbf{M}$$

where  $\Delta$  is the so-called Laplace operator. We interpret  $\nabla \cdot \mathbf{M}$  as the magnetic source of the  $\mathbf{B}$ -field.

### 2.2.1 Solving Poission's equation

Poisson's equation can be solved analytically using the fundamental solution of Laplace's equation. A derivation of this fundamental solution for the Laplace equation in  $\mathbb{R}^n$  can be found in appendix B. Notice that  $\Omega$  is a two-dimensional object with one-dimensional boundary surfaces and thickness  $t$ . We obtain the following solution for  $\varphi$  (see "appendix B and appendix C for more explanation on this expression):

$$\begin{aligned} \varphi(\mathbf{r}) = & -\frac{t}{4\pi} \iint_{\Omega} \frac{(\nabla' \cdot \mathbf{M})(\mathbf{r}')}{|\mathbf{r} - \mathbf{r}'|} d\mathbf{r}' + \frac{t}{4\pi} \int_{\partial\Omega} \frac{\mathbf{n}'(\mathbf{r}') \cdot \mathbf{M}(\mathbf{r}')}{|\mathbf{r} - \mathbf{r}'|} d\mathbf{r}' \\ & + \frac{t}{4\pi} \iint_{\Omega} \frac{\partial}{\partial\nu'} \left( \frac{1}{|\mathbf{r} - \mathbf{r}'|} \right) \mathbf{n}'(\mathbf{r}') \cdot \mathbf{M}(\mathbf{r}') d\mathbf{r}' \end{aligned} \quad (2.1)$$

Here, the first two integrals in  $\varphi(\mathbf{r})$  are convolutions of the Green's function

$$G(\mathbf{r}) = -\frac{1}{4\pi} \frac{1}{|\mathbf{r}|}$$

and the functions  $\nabla \cdot \mathbf{M}$  on  $\Omega$  and the flux  $\mathbf{n} \cdot \mathbf{M}$  on the boundary  $\partial\Omega$  respectively. The third integral is called a *double layer potential*. A derivation of this double layer potential term in the potential expression can be found in appendix C.

Knowing  $\varphi$  we can obtain the  $\mathbf{H}$ -field via the Hodge-decomposition

$$\mathbf{H}(\mathbf{r}) = -\nabla\varphi(\mathbf{r})$$

There is also an analytical expression to be computed for  $\mathbf{H}(\mathbf{r})$ . Note that in the expression  $\mathbf{H}(\mathbf{r}) = -\nabla\varphi(\mathbf{r})$  the gradient is with respect to  $\mathbf{r}$ . We can derive the following expression:

$$\begin{aligned} \mathbf{H}(\mathbf{r}) = & -\frac{t}{4\pi} \iint_{\Omega} \frac{\mathbf{r} - \mathbf{r}'}{|\mathbf{r} - \mathbf{r}'|^3} \nabla \cdot \mathbf{M}(\mathbf{r}') d\mathbf{r}' + \frac{t}{4\pi} \int_{\partial\Omega} \frac{\mathbf{r} - \mathbf{r}'}{|\mathbf{r} - \mathbf{r}'|^3} \mathbf{n}'(\mathbf{r}') \cdot \mathbf{M}(\mathbf{r}') d\mathbf{r}' \\ & + \frac{1}{4\pi} \iint_{\Omega} \frac{\partial}{\partial \nu'} \left( \frac{\mathbf{r} - \mathbf{r}'}{|\mathbf{r} - \mathbf{r}'|^3} \right) \mathbf{n}'(\mathbf{r}') \cdot \mathbf{M}(\mathbf{r}') d\mathbf{r}' \end{aligned} \quad (2.2)$$

Here, we have used that  $\nabla \left( \frac{1}{|\mathbf{r} - \mathbf{r}'|} \right) = -\frac{\mathbf{r} - \mathbf{r}'}{|\mathbf{r} - \mathbf{r}'|^3}$ . For any point  $\mathbf{r} \notin \Omega$  we have that  $\mathbf{M} \equiv \mathbf{0}$  so the following relation

$$\mathbf{B} = \mu_0 \mathbf{H}$$

can be used to give an analytical description of the  $\mathbf{B}$ -field outside the object  $\Omega$ , namely

$$\begin{aligned} \mathbf{B}(\mathbf{r}) = & -\frac{\mu_0 t}{4\pi} \iint_{\Omega} \frac{\mathbf{r} - \mathbf{r}'}{|\mathbf{r} - \mathbf{r}'|^3} \nabla \cdot \mathbf{M}(\mathbf{r}') d\mathbf{r}' + \frac{\mu_0 t}{4\pi} \int_{\partial\Omega} \frac{\mathbf{r} - \mathbf{r}'}{|\mathbf{r} - \mathbf{r}'|^3} \mathbf{n}'(\mathbf{r}') \cdot \mathbf{M}(\mathbf{r}') d\mathbf{r}' \\ & + \frac{\mu_0 t}{4\pi} \iint_{\Omega} \frac{\partial}{\partial \nu'} \left( \frac{\mathbf{r} - \mathbf{r}'}{|\mathbf{r} - \mathbf{r}'|^3} \right) \mathbf{n}'(\mathbf{r}') \cdot \mathbf{M}(\mathbf{r}') d\mathbf{r}' \end{aligned} \quad (2.3)$$

where the first two integrals correspond to magnetic field components that are *tangential* to the object  $\Omega$ . We call the third integral the *double layer component* of the magnetic field.

### 2.3 Approximation of forward problem solutions

In the previous section we have derived an analytical expression for the magnetic induction field  $\mathbf{B}$  that comes from some magnetization  $\mathbf{M}$  of the object  $\Omega$ . We now approximate the magnetic induction field by means of quadrature rules. Let  $\{T\}$  be a triangulation of  $\Omega$ . Define the set of triangular elements by  $E$ , the set of line boundary elements by  $BE$  and the set of vertices by  $P$ . This defines a partitioning of  $\Omega$  by the triple  $(P, E, BE)$ . The analytical description of  $\mathbf{B}$  on this partitioning becomes

$$\begin{aligned} \mathbf{B}(\mathbf{r}) = & -\frac{\mu_0 t}{4\pi} \sum_{i=1}^{|E|} \iint_{e_i} \frac{\mathbf{r} - \mathbf{r}'}{|\mathbf{r} - \mathbf{r}'|^3} \nabla \cdot \mathbf{M}(\mathbf{r}') d\mathbf{r}' + \frac{\mu_0 t}{4\pi} \sum_{i=1}^{|BE|} \int_{be_i} \frac{\mathbf{r} - \mathbf{r}'}{|\mathbf{r} - \mathbf{r}'|^3} \mathbf{n}'(\mathbf{r}') \cdot \mathbf{M}(\mathbf{r}') d\mathbf{r}' \\ & + \frac{\mu_0 t}{4\pi} \sum_{i=1}^{|E|} \iint_{e_i} \frac{\partial}{\partial \nu'} \left( \frac{\mathbf{r} - \mathbf{r}'}{|\mathbf{r} - \mathbf{r}'|^3} \right) \mathbf{n}'(\mathbf{r}') \cdot \mathbf{M}(\mathbf{r}') d\mathbf{r}' \end{aligned} \quad (2.4)$$

Notice that on each triangular element and boundary element, the normal vector  $\mathbf{n}$  is constant. Applying a symmetric quadrature rule on each internal element  $e_i$  and a line

quadrature rule on each boundary element  $be$  now leads to an approximation of  $\mathbf{B}$ . In appendix D more information about the quadrature rules involved in this computation can be found.

An analytical expression for the magnetic induction field  $\mathbf{B}$  given some uniform magnetization of a single steel plate can be found in appendix E. This expression is used to validate if the forward is correctly implemented in `MATLAB`.

## 2.4 Derivation of the inverse problem

In this section the linear inverse problem is derived. We want to note that in Chapter 3 we give a general overview of inverse theory. For now we give a heuristic idea behind the inverse problem. From the forward problem description in the previous section we know that, given some magnetization  $\mathbf{M}$  of an object  $\Omega$ , the induced magnetic field can be computed via formula 2.3.

The integral equation that defines the inverse problem is given in the following formulation: Given the function  $\mathbf{B} : \mathbb{R}^3 \setminus \Omega \rightarrow \mathbb{R}^3$ , determine continuous source functions  $f, g$  and  $h$  such that

$$\begin{aligned} \mathbf{B}(\mathbf{r}) = & -\frac{\mu_0 t}{4\pi} \iint_{\Omega} \frac{\mathbf{r} - \mathbf{r}'}{|\mathbf{r} - \mathbf{r}'|^3} f(\mathbf{r}') d\mathbf{r}' + \frac{\mu_0 t}{4\pi} \int_{\partial\Omega} \frac{\mathbf{r} - \mathbf{r}'}{|\mathbf{r} - \mathbf{r}'|^3} g(\mathbf{r}') d\mathbf{r}' \\ & + \frac{\mu_0 t}{4\pi} \iint_{\Omega} \frac{\partial}{\partial \nu'} \left( \frac{\mathbf{r} - \mathbf{r}'}{|\mathbf{r} - \mathbf{r}'|^3} \right) h(\mathbf{r}') d\mathbf{r}' := R(f)(\mathbf{r}) + S(g)(\mathbf{r}) + T(h)(\mathbf{r}) \end{aligned} \quad (2.5)$$

where  $R, S, T$  are the corresponding integral operators. The volume of object  $\Omega$  is a compact subset of  $\mathbb{R}^3$ . Here,  $f$  and  $h$  represent the magnetic sources in  $\Omega$  and  $g$  is the magnetic source on the boundary  $\partial\Omega$ . The vector function  $\mathbf{B}$  is the magnetic induction field, generated by these sources.

Therefore the task is, given measurements of the magnetic induction field  $\mathbf{B}$ , to find source functions  $f, g$  and  $h$  such that the generated field by these sources matches the measurements as accurate as possible.

Unfortunately in the situation we just described, we normally do not have access to a full description of the magnetic induction field  $\mathbf{B}$ . However, we can measure the magnetic induction field by means of magnetic field sensors. We can measure the field by a finite number of measurements and the more measurement points available, the more information about  $\mathbf{B}$  may be known.

To be able to solve the inverse problem, we reduce it to a finite-dimensional one. For instance this can be done by a so-called expansion method or by approximating the integrals involved in the inverse formulation by appropriate quadrature rules. This finite-dimensional formulation allows us to use magnetic field measurements as input for the inverse problem.

### 2.4.1 Petrov-Galerkin Expansion Method

In [10, Ch. 3, p. 25-26] the so-called Petrov-Galerkin method is described for inverse problems defined over intervals. This expansion method can be used (like finite element methods) to derive a system of linear equations. Solutions of such systems are then approximations of solutions of the inverse problem.

In this section we extend the Petrov-Galerkin method mentioned in [10] to multiple dimensions and apply this method to our inverse problem.

### 2.4.1.1 Expansion of functions

Introduce a partitioning of  $\Omega$  by the triple  $(P, E, BE)$ . Here,  $P$  stands for the set of grid points,  $E$  is the set of triangular elements and  $BE$  is the set of line boundary elements. An example of such partitioning is given in Figure 2.1. The Petrov-Galerkin method is based on expanding the functions involved in terms of predefined sets of basis functions:

- The basis functions  $(\varphi_i)_{i=1}^N$  are defined on the triangular elements  $E$ . These describe the magnetic sources inside  $\Omega$ .
- The basis functions  $(\bar{\varphi}_i)_{i=1}^M$  are defined on the boundary elements  $BE$ . These describe the magnetic flux at the boundaries  $\partial\Omega$ .
- The basis functions  $(\psi_i)_{i=1}^K$  defined on  $\mathbb{R}^3 \setminus \Omega$  (outside the object  $\Omega$ ) are *vector functions*. The basis functions  $\psi_i$  are used to formulate the measurements of the magnetic field, outside the object  $\Omega$ .

The value  $M$  is three times the number of triangular elements and  $N$  is two times the number of boundary elements. The value of  $K$  is specified later on. The basis functions should be chosen in such a way that they provide a good description of the solutions that we seek.

Expand the functions  $\mathbf{B}$ ,  $f$  and  $g$  by using these basis functions:

$$\begin{aligned} f &= f^M + E_f, & f^M &\in \text{sp}(\varphi_1, \varphi_2, \dots, \varphi_M) \\ g &= g^N + E_g, & g^N &\in \text{sp}(\bar{\varphi}_1, \bar{\varphi}_2, \dots, \bar{\varphi}_N) \\ h &= h^M + E_h, & h^M &\in \text{sp}(\varphi_1, \varphi_2, \dots, \varphi_M) \\ \mathbf{B} &= \mathbf{B}^K + \mathbf{E}_B, & \mathbf{B}^K &\in \overline{\text{sp}}(\psi_1, \psi_2, \dots, \psi_K) \end{aligned}$$

where  $E_f, E_g, E_h$  and  $\mathbf{E}_B$  are the errors in the expansions, and

$$f^M = \sum_{j=1}^M p_j \varphi_j, \quad g^N = \sum_{j=1}^N p_{j+M} \bar{\varphi}_j, \quad h^M = \sum_{j=1}^M p_{j+(M+N)} \varphi_j, \quad \mathbf{B}^K = \sum_{i=1}^K \mathbf{b}_i \odot \psi_i,$$

In the above expansions of  $f, g, h$  and  $\mathbf{B}$  the variables  $p_j$  are unknown scalar coefficients. The vectors  $\mathbf{b}_i \in \mathbb{R}^3$  are connected to the measurements (and therefore known in the inverse formulation(!)). The operation  $\mathbf{b}_i \odot \psi_i$  stands for **component-wise** multiplication.

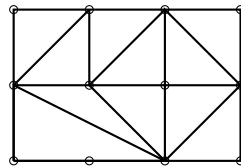


Figure 2.1: An example of a partitioning of a rectangle in triangular and line boundary elements. In this mesh we have 12 grid points, 11 triangular elements and 10 boundary elements.

The expansion

$$\mathbf{B} = \mathbf{B}^K + \mathbf{E}_B, \quad \mathbf{B}^K \in \overline{\text{sp}}(\boldsymbol{\psi}_1, \boldsymbol{\psi}_2, \dots, \boldsymbol{\psi}_K)$$

should be read component-wise, i.e., each component of  $\mathbf{B}$  is expanded individually:

$$\begin{aligned} (\mathbf{B})_x &= (\mathbf{B}^K)_x + (\mathbf{E}_B)_x, & (\mathbf{B}^K)_x &\in \text{sp}((\boldsymbol{\psi}_1)_x, (\boldsymbol{\psi}_2)_x, \dots, (\boldsymbol{\psi}_K)_x) \\ (\mathbf{B})_y &= (\mathbf{B}^K)_y + (\mathbf{E}_B)_y, & (\mathbf{B}^K)_y &\in \text{sp}((\boldsymbol{\psi}_1)_y, (\boldsymbol{\psi}_2)_y, \dots, (\boldsymbol{\psi}_K)_y) \\ (\mathbf{B})_z &= (\mathbf{B}^K)_z + (\mathbf{E}_B)_z, & (\mathbf{B}^K)_z &\in \text{sp}((\boldsymbol{\psi}_1)_z, (\boldsymbol{\psi}_2)_z, \dots, (\boldsymbol{\psi}_K)_z) \end{aligned}$$

Therefore the three expansions of  $(\mathbf{B})_x$ ,  $(\mathbf{B})_y$  and  $(\mathbf{B})_z$  leads to the known vector  $\mathbf{b}_i$  in the expansion of  $\mathbf{B}$ .

Using the integral operators  $R, S$  and  $T$  introduced in equation 2.5, define the vector function  $\boldsymbol{\nu} : \mathbb{R}^{2M+N} \rightarrow \mathbb{R}^3$

$$\boldsymbol{\nu} = \begin{bmatrix} (\boldsymbol{\nu})_x \\ (\boldsymbol{\nu})_y \\ (\boldsymbol{\nu})_z \end{bmatrix} = R(f^M) + S(g^N) + T(h^M) = \sum_{j=1}^M p_j (R\varphi_j) + \sum_{j=1}^N p_{j+M} (S\bar{\varphi}_j) + \sum_{j=1}^M p_{j+(M+N)} (T\varphi_j)$$

Write the vector function  $\boldsymbol{\nu}$  as (in a similar way as we expanded the function  $\mathbf{B}$ )

$$\boldsymbol{\nu} = \boldsymbol{\nu}^K + \mathbf{E}_\nu, \quad \boldsymbol{\nu}^K \in \overline{\text{sp}}(\boldsymbol{\psi}_1, \boldsymbol{\psi}_2, \dots, \boldsymbol{\psi}_K)$$

The vector function  $\boldsymbol{\nu}$  represents the magnetic field that is produced by the source functions  $f^M, g^N$  and  $h^M$ . Note that in general  $\boldsymbol{\nu}$  is not identical to  $\mathbf{B}$ , nor that  $\boldsymbol{\nu}$  lies in the subspace  $\overline{\text{sp}}(\boldsymbol{\psi}_1, \boldsymbol{\psi}_2, \dots, \boldsymbol{\psi}_K)$ .

#### 2.4.1.2 Orthogonality condition

Let  $\mathbf{B}^K$  and  $\boldsymbol{\nu}^K$  be the orthogonal projection onto subspace  $\overline{\text{sp}}(\boldsymbol{\psi}_1, \boldsymbol{\psi}_2, \dots, \boldsymbol{\psi}_K)$ . Note that the orthogonal projection is done component-wise. Now both  $\boldsymbol{\nu}^K$  and  $\mathbf{B}^K$  are uniquely determined as the subspace  $\text{sp}(\boldsymbol{\psi}_1, \boldsymbol{\psi}_2, \dots, \boldsymbol{\psi}_K)$  is closed. The Petrov-Galerkin approach is to determine the unknown coefficients  $p_j$  and such that

$$\boldsymbol{\nu}^K = \mathbf{B}^K$$

Using the expressions above we can rewrite this statement in the following form: find unknowns  $p_j$  and such that

$$\boldsymbol{\nu} - \mathbf{B} = E_\nu - E_B$$

Because  $E_\nu, E_B \perp \overline{\text{sp}}(\boldsymbol{\psi}_1, \boldsymbol{\psi}_2, \dots, \boldsymbol{\psi}_K)$ , we have that  $\boldsymbol{\nu} - \mathbf{B} \perp \overline{\text{sp}}(\boldsymbol{\psi}_1, \boldsymbol{\psi}_2, \dots, \boldsymbol{\psi}_K)$  component-wise. The Petrov-Galerkin condition can now be stated as follows: find unknowns  $p_i$  such that

$$\langle \boldsymbol{\psi}_i, (\boldsymbol{\nu} - \mathbf{B}) \rangle = 0, \quad \text{for } i = 1, 2, \dots, K \quad (2.6)$$

where the ‘‘inner product’’ should be read component-wise, i.e.,

$$\begin{cases} \langle (\boldsymbol{\psi}_i)_x, (\boldsymbol{\nu} - \mathbf{B})_x \rangle_2 = 0 \\ \langle (\boldsymbol{\psi}_i)_y, (\boldsymbol{\nu} - \mathbf{B})_y \rangle_2 = 0 \\ \langle (\boldsymbol{\psi}_i)_z, (\boldsymbol{\nu} - \mathbf{B})_z \rangle_2 = 0 \end{cases}, \quad \text{for } i = 1, 2, \dots, K$$

Here, the inner product  $\langle \cdot, \cdot \rangle_2$  is defined by

$$\langle f, g \rangle_2 = \iiint_{\mathbb{R}^3 \setminus \Omega} f(\mathbf{r})g(\mathbf{r})d\mathbf{r}$$

For simplicity the following “inner product” between a function  $f : \mathbb{R}^3 \setminus \Omega \rightarrow \mathbb{R}$  and  $\mathbf{g} : \mathbb{R}^3 \setminus \Omega \rightarrow \mathbb{R}^3$  is defined

$$\langle \mathbf{f}, \mathbf{g} \rangle := \begin{bmatrix} \langle (\mathbf{f})_x, (\mathbf{g})_x \rangle_2 \\ \langle (\mathbf{f})_y, (\mathbf{g})_y \rangle_2 \\ \langle (\mathbf{f})_z, (\mathbf{g})_z \rangle_2 \end{bmatrix} = \iiint_{\mathbb{R}^3 \setminus \Omega} \mathbf{f}(\mathbf{r}) \odot \mathbf{g}(\mathbf{r})d\mathbf{r}$$

Returning to the orthogonality relations, for each  $\psi_i$  equation 2.6 can be expressed as

$$\langle \psi_i, \boldsymbol{\nu} - \mathbf{B} \rangle = \sum_{j=1}^M p_j \langle \psi_i, R\varphi_j \rangle + \sum_{j=1}^N p_{j+M} \langle \psi_i, S\bar{\varphi}_j \rangle + \sum_{j=1}^M p_{j+(M+N)} \langle \psi_i, T\varphi_j \rangle \quad (2.7)$$

which leads to a system of linear equations

$$[A_f | A_g | A_h] \begin{bmatrix} \mathbf{p}_f \\ \mathbf{p}_g \\ \mathbf{p}_h \end{bmatrix} = \mathbf{b} \quad \text{or simply} \quad A\mathbf{p} = \mathbf{b} \quad (2.8)$$

where  $A$  is a  $3K \times (M + N + M)$  matrix,  $\mathbf{p}$  is a  $(M + N + M) \times 1$  vector and  $\mathbf{b}$  is a  $3K \times 1$  vector. The matrix  $A$  is called the *field matrix* that contains the physics model involved, and  $\mathbf{b}$  is called the *load vector*. For  $i = 1, 2, \dots, K$  equation 2.7 leads to three rows in  $A$  and 3 entries in the vector  $\mathbf{b}$ :

$$\begin{aligned} [3 \times 1] \quad \mathbf{a}_{ij} &= \langle \psi_i, R\varphi_j \rangle & \text{for } j = 1, 2, \dots, M \\ [3 \times 1] \quad \mathbf{a}_{ij} &= \langle \psi_i, S\bar{\varphi}_j \rangle & \text{for } j = M + 1, 2, \dots, M + N \\ [3 \times 1] \quad \mathbf{a}_{ij} &= \langle \psi_i, T\varphi_j \rangle & \text{for } j = (M + N) + 1, 2, \dots, 2M + N \\ [3 \times 1] \quad \mathbf{b}_i &= \langle \psi_i, \mathbf{B} \rangle \end{aligned}$$

To solve our specific integral equation we choose the following basis functions:

- (I)  $(\varphi_i)_{i=1}^M$  are linear functions on  $E$  [three basis functions per internal element  $e$  (triangles)]
- (II)  $(\bar{\varphi}_i)_{i=1}^N$  are linear functions on  $BE$  [two basis functions per boundary element  $be$  (line elements)]
- (III)  $(\psi_i)_{i=1}^K$  are vector functions that consist of delta functions defined on  $\mathbb{R}^3 \setminus \Omega$ :

$$\psi_i(\mathbf{r}) = \begin{bmatrix} \delta(x - x_i) \\ \delta(y - y_i) \\ \delta(z - z_i) \end{bmatrix} := \boldsymbol{\delta}(\mathbf{r} - \mathbf{r}_i) \text{ where } \mathbf{r}_i = (x_i, y_i, z_i)^T \text{ is the location of a measurement.}$$

### 2.4.2 Construction of basis functions $\psi_i$

We take  $K$  measurements at different sensor positions of the magnetic. Each measurement is associated with a basis function  $\psi$ , which is built out of delta functions. For basis functions  $\psi_i$  we have:

$$\mathbf{b}_i = \langle \psi_i, \mathbf{B} \rangle = \iiint_{\mathbb{R}^3 \setminus \Omega} \delta(\mathbf{r} - \mathbf{r}_i) \odot \mathbf{B}(\mathbf{r}) d\mathbf{r} = \mathbf{B}(\mathbf{r}_i)$$

by the fundamental property of a Dirac-delta function. So by ‘‘collocation’’ of the measurements of the magnetic field we can find the coefficients of the lead vector  $\mathbf{b}$ . The above coefficients  $\mathbf{a}_{ij}$  can be computed by applying quadrature rules on each of the integrals involved, as we did in the approximation of the solution of the forward problem.

### 2.4.3 Construction of basis functions $\varphi_i$

It remains to construct the basis functions  $\varphi_i$  on the internal elements  $E$  and  $\bar{\varphi}_i$  on the boundary line elements  $BE$ . First we construct on each internal element in  $E$  three linear basis functions. Let  $\{\mathbf{v}_1, \mathbf{v}_2, \mathbf{v}_3\}$  denote the set of vertices of the fixed internal element  $e$ . The three linear basis functions  $\varphi_1, \varphi_2$  and  $\varphi_3$  on  $E$  have to satisfy the following conditions:

$$\varphi_i(\mathbf{v}_j) = \delta_{ij}, \quad \varphi_i \text{ is linear on } e, \quad \varphi_i \equiv 0 \text{ outside } e$$

Note that the basis functions  $\varphi$  are discontinuous in  $\mathbf{r} = \mathbf{r}_i$ . In the derivation of these basis functions we use the following functions which are basically the basis functions on a standard triangle  $T_{st}$  in the plane  $\mathbb{R}^2$ . The triangle  $T_{st}$  has vertices  $(0, 0)$ ,  $(1, 0)$  and  $(0, 1)$ , see Figure 2.2. Consider the function that maps the stand triangle in  $\mathbb{R}^2$  onto the internal element  $E$

$$\mathbf{r}(s, t) = \mathbf{v}_1 + (\mathbf{v}_2 - \mathbf{v}_1)s + (\mathbf{v}_3 - \mathbf{v}_1)t$$

See also figure 2.2, where  $\mathbf{v}_j = (x_j, y_j, z_j)^T$ .

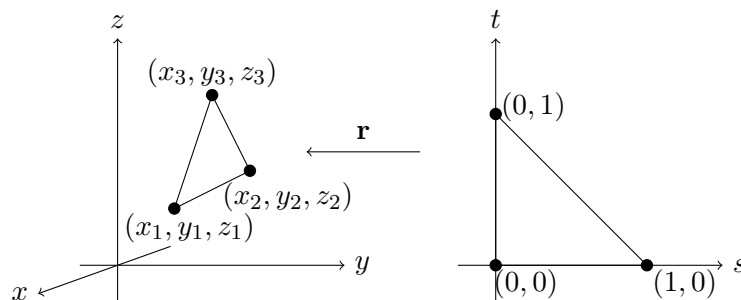


Figure 2.2: Triangle transformation

Let  $u_1, u_2$  and  $u_3$  denote the three linear basis functions on the standard triangle  $T_{st}$ . This means that  $u_1$  is one in the vertex  $(0, 0)$  and zero in the other vertices,  $u_2$  is one in the vertex  $(1, 0)$  and zero in the others, and  $u_3$  is one in the vertex  $u(0, 1)$  and zero in the others. Each of the  $u_i$  is of the form  $u_i(\mathbf{r}) = a_0^i + a_1^i s + a_2^i t$  for  $i = 1, 2, 3$ . It is now the task to determine the coefficients such that the above conditions holds for  $i = 1, 2, 3$ . The  $u_i(\mathbf{r})$  should be right in their own vertices:

$$\begin{bmatrix} 1 & 0 & 0 \\ 1 & 1 & 0 \\ 1 & 0 & 1 \end{bmatrix} \begin{bmatrix} a_0^1 & a_1^1 & a_2^1 \\ a_0^2 & a_1^2 & a_2^2 \\ a_0^3 & a_1^3 & a_2^3 \end{bmatrix} = \begin{bmatrix} 1 & 0 & 0 \\ 0 & 1 & 0 \\ 0 & 0 & 1 \end{bmatrix}$$

The above system is non singular, hence for every internal element  $e$  we can compute the coefficients exactly, leading to

$$u_1(s, t) = 1 - s - t, \quad u_2(s, t) = s, \quad u_3(s, t) = t, \quad \text{for } (s, t) \in T_{st}$$

These functions can be used to define the basis functions  $\varphi_1, \varphi_2$  and  $\varphi_3$  on the internal element  $E$  (By taking suitable compositions of  $u$  with the transformation  $\mathbf{r}$ ). However, only the basis functions  $u_{1,2}$  and  $u_3$  on each triangular element  $E$  are required to compute the entries of the matrix  $A$  in equation 2.8. This becomes clear when we approximate the entries of the matrix  $A$  in the next section.

### 2.4.4 Construction of basis functions $\bar{\varphi}_i$

Suppose that  $BE$  denotes a boundary element with vertices  $\mathbf{v}_1$  and  $\mathbf{v}_2$ . We look for two linear basis functions  $\bar{\varphi}_1$  and  $\bar{\varphi}_2$  such that

$$\bar{\varphi}_i(\mathbf{v}_j) = \delta_{ij}, \quad \varphi_i \text{ is linear on } be, \quad \varphi_i \equiv 0 \text{ outside } be$$

Similar to the steps we have taken in the previous subsection, we look at basis functions defined on the interval  $[-1, 1]$ . Let  $\bar{\mathbf{r}} : [-1, 1] \rightarrow be$  given by

$$\bar{\mathbf{r}} = \frac{1}{2}(\mathbf{v}_1 + \mathbf{v}_2) - \frac{1}{2}\xi(\mathbf{v}_2 - \mathbf{v}_1), \quad \xi \in [-1, 1]$$

See Figure 2.3. The corresponding basis functions  $u_1$  and  $u_2$  are given by:

$$\bar{u}_1(\xi) = \frac{1}{2} - \frac{1}{2}\xi, \quad \bar{u}_2(\xi) = \frac{1}{2} + \frac{1}{2}\xi, \quad \text{for } \xi \in [-1, 1]$$

which satisfies  $\bar{u}_1(-1) = 1, \bar{u}_1(1) = 0$  and  $\bar{u}_2(-1) = 0, \bar{u}_2(1) = 1$ .

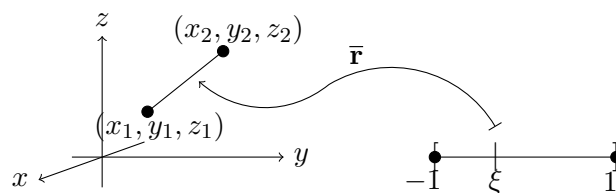


Figure 2.3: Boundary line element transformation.

### 2.4.5 Approximation of the matrix entries $\mathbf{a}_{ij}$

Now that the basis functions are defined, we derive approximations of the elements of  $A$  in equation 2.8 that are related to the unknowns  $p_i$  on an internal element  $E$  and on a boundary element  $BE$ .

Consider basis function  $\psi_i$  and let  $j \leq M$  be fixed. The linear basis function  $\varphi_j$  then corresponds to some internal element  $e_j$ . A part of the column  $\mathbf{a}_{ij}$  (three entries) is given by  $\mathbf{a}_{ij} = \langle \psi_i, R\varphi_j \rangle$  and using that the support of  $\varphi_j$  is lying in  $e_j$  leads to the following approximation: for  $j = 1, 2, \dots, M$

$$\begin{aligned} \mathbf{a}_{ij} &= \langle \psi_i, R\varphi_j \rangle \\ &= \iiint_{\mathbb{R}^3 \setminus \Omega} \left[ \delta(\mathbf{r} - \mathbf{r}_i) \odot \iint_{\Omega} \frac{\mathbf{r} - \mathbf{r}'}{|\mathbf{r} - \mathbf{r}'|^3} \varphi_j(\mathbf{r}') d\mathbf{r}' \right] d\mathbf{r} \\ &= -\frac{\mu_0 t}{4\pi} \iint_{e_j} \frac{\mathbf{r}_i - \mathbf{r}'}{|\mathbf{r}_i - \mathbf{r}'|^3} \varphi_j(\mathbf{r}') d\mathbf{r}' \\ &= -\frac{\mu_0 t \cdot 2|e_j|}{4\pi} \iint_{Tr} \frac{\mathbf{r}_i - \mathbf{r}'(s, t)}{|\mathbf{r}_i - \mathbf{r}'(s, t)|^3} u_j(\mathbf{r}'(s, t)) d\mathbf{r}' \\ &\approx -\frac{\mu_0 t \cdot |e_j|}{4\pi} \sum_{k=1}^{n_g} w_k \frac{\mathbf{r}_i - \mathbf{r}'(s_k, t_k)}{|\mathbf{r}_i - \mathbf{r}'(s_k, t_k)|^3} u_j(\mathbf{r}'(s_k, t_k)) \end{aligned}$$

where  $u_j$  is one of the three basis functions defined on the standard triangle in  $\mathbb{R}^2$  that corresponds to  $\varphi_j$ , and in the approximation step we applied a Symmetric Triangular Quadrature rule, see appendix D.1. Here  $n_g$  is the number of quadrature points used for the triangle. Note how we use the basis functions  $u_1, u_2$  and  $u_3$  defined on the standard triangle in the approximation of the entries of  $\mathbf{a}_{ij}$ .

In the same way we derive approximations of 3-parts of  $\mathbf{a}_{ij}$  that correspond to the boundary elements  $BE$ . For  $j = M + 1, M + 2, \dots, M + N$ :

$$\begin{aligned} \mathbf{a}_{ij} &= \langle \psi_i, S\bar{\varphi}_j \rangle \\ &= \iiint_{\mathbb{R}^3 \setminus \Omega} \left[ \delta(\mathbf{r} - \mathbf{r}_i) \odot \iint_{\partial\Omega} \frac{\mathbf{r} - \mathbf{r}'}{|\mathbf{r} - \mathbf{r}'|^3} \bar{\varphi}_j(\mathbf{r}') d\mathbf{r}' \right] d\mathbf{r} \\ &= -\frac{\mu_0 t}{4\pi} \int_{be_j} \frac{\mathbf{r}_i - \mathbf{r}'}{|\mathbf{r}_i - \mathbf{r}'|^3} \bar{\varphi}_j(\mathbf{r}') d\mathbf{r}' \\ &= -\frac{\mu_0 t}{4\pi} \frac{|be_j|}{2} \int_{-1}^1 \frac{\mathbf{r}_i - \mathbf{r}'(\xi)}{|\mathbf{r}_i - \mathbf{r}'(\xi)|^3} \bar{u}_j(\mathbf{r}'(\xi)) d\xi \\ &\approx -\frac{\mu_0 t}{4\pi} \frac{|be_j|}{2} \sum_{k=1}^{n_g} w_k \frac{\mathbf{r}_i - \mathbf{r}'(\xi_k)}{|\mathbf{r}_i - \mathbf{r}'(\xi_k)|^3} \bar{u}_j(\mathbf{r}'(\xi_k)) \end{aligned}$$

In the approximation step we applied a line quadrature rule, see appendix D.2.

Lastly, the approximations of the 3 element-parts of  $\mathbf{a}_{ij}$  are based on the derivations of the forward problem in appendix C. For  $j = (M + N) + 1, \dots, 2M + N$

$$\begin{aligned}
\mathbf{a}_{ij} &= \langle \boldsymbol{\psi}_i, T\varphi_j \rangle \\
&= \iiint_{\mathbf{R}^3 \setminus \Omega} \left[ \boldsymbol{\delta}(\mathbf{r} - \mathbf{r}_i) \odot \iint_{\Omega} \frac{\partial}{\partial \boldsymbol{\nu}'} \left( \frac{\mathbf{r} - \mathbf{r}'}{|\mathbf{r} - \mathbf{r}'|^3} \right) \varphi_j(\mathbf{r}') d\mathbf{r}' \right] d\mathbf{r} \\
&= \frac{\mu_0 t}{4\pi} \iint_{e_j} \frac{\partial}{\partial \boldsymbol{\nu}'} \left( \frac{\mathbf{r}_i - \mathbf{r}'}{|\mathbf{r}_i - \mathbf{r}'|^3} \right) \varphi_j(\mathbf{r}') d\mathbf{r}' \\
&\approx -\frac{\mu_0 t}{4\pi} |e_j| \left( \sum_{k=1}^{n_g} w_k \frac{1}{|\mathbf{r}_i - \mathbf{r}'(s_k, t_k)|^3} u_j(\mathbf{r}'(s_k, t_k)) \right) \mathbf{n}_j \\
&\quad + \frac{3\mu_0 t}{4\pi} |e_j| \sum_{k=1}^{n_g} w_k \mathbf{n}_j \cdot (\mathbf{r}_i - \mathbf{r}'(s_k, t_k)) \frac{\mathbf{r}_i - \mathbf{r}'(s_k, t_k)}{|\mathbf{r}_i - \mathbf{r}'(s_k, t_k)|^5} u_j(\mathbf{r}'(s_k, t_k))
\end{aligned}$$

### 2.4.6 Continuity of inverse solutions and number of unknowns

The above application of Petrov-Galerkin leads to a large system of linear equations, depending on the choice of the meshing. For geometries such as large naval ships, the systems become extremely large, which makes solving the system problematic.

The dimensions of the system can be reduced by demanding that the solutions  $f, g$  and  $h$  are continuous on the complete geometry  $\Omega$ . The physical interpretation of this reduction arises from the behavior of the magnetic sources  $f, g$  and  $h$ . One can show that the magnetic sources are continuous. For us that means that there are unknowns  $p_i$  of adjacent triangular and boundary elements that take the same value. This identification leads to a reduction of the number of unknowns. In figure 2.4 this idea is illustrated. The same reduction holds for unknowns defined boundary elements and for the unknowns  $p_i$  that describe the function  $h$  on the internal elements.

For those unknowns  $p_j$  that we identify as described above, we can add up the corresponding columns  $\mathbf{a}_{ij}$  in equation 2.8. This leads to a reduction of the number of unknowns (and therefore to a reduction of columns) and we obtain the adjusted linear inverse formulation

$$A' \bar{\mathbf{p}} = \mathbf{b} \quad (2.9)$$

The linear system described in equation 2.9 has fewer columns and therefore it is better determined. Furthermore, solutions of system 2.9 correspond to continuous source functions  $f^M, g^N$  and  $h^M$  on  $\Omega$ . From a physical point of view magnetic sources inside the steel satisfy a continuity condition and therefore we expect that the solutions of equation 2.9 are more feasible for the prediction model.

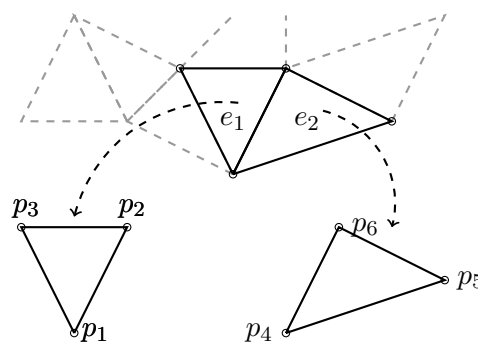


Figure 2.4: A part of a mesh in the internal geometry of the mock-up is shown. We assume that the solution  $f$  in the inverse problem is continuous on the whole geometry. Therefore we can conclude that  $p_1 = p_4$  and  $p_2 = p_6$  must hold. This leads to a reduction of unknowns, because the function  $f$  is now fully described by 4 unknowns (instead of 6 unknowns without the assumption on the continuity of  $f$ ).

## 2.5 Prediction model

The forward model and inverse model formulations allow us to define a prediction model for the magnetic signature of a ferromagnetic object. As the derivation of the inverse model already indicates, this prediction model is based on a number of measurements of the magnetic signature by sensors. The prediction model is summarized in the following three steps:

1. Measure the magnetic signature of a ferromagnetic object using a finite number of sensor positions;
2. Estimate the magnetic sources in the ferromagnetic object via the inverse model formulation;
3. Use the magnetic sources to approximate the magnetic signature of the ferromagnetic object (in other positions than just the measurement positions).

A flow chart of the prediction model is given in figure 2.5. In Chapter 6 we validate the inverse problem and the prediction model. Observe that we are interested in the results of the prediction model, however the behavior of the inverse problem solutions plays a major role in the validity of the prediction model.

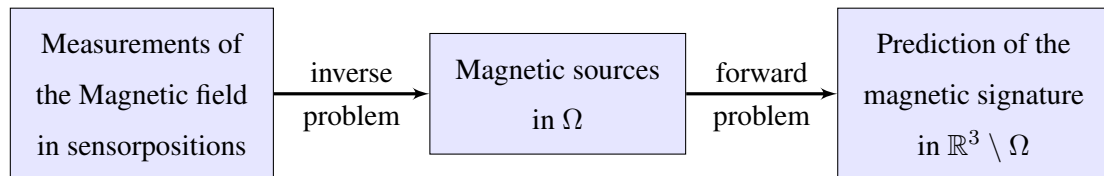


Figure 2.5: Simple flow chart of the prediction model.

## 2.6 Remarks

### 2.6.1 Non-uniqueness of the inverse problem

The prediction model consists of solving an inverse problem, based on on-board measurements of the magnetic signature. In practice, we will use a finite number of sensors, say around the 20 magnetic sensors. Therefore, our discrete inverse problem is most likely *under determined*: the matrix  $A$  has more columns than rows. Of course, this depends on the ratio between the number of measurements and the dimensions of the partitioning of  $\Omega$ .

One of the direct implications of an under-determined system is that the null space of  $A$  is non-trivial and therefore the discrete inverse problem has infinite many solutions. Of course, an under determined linear system can also have no solutions, take for example

$$\begin{bmatrix} 1 & 0 & 0 \\ 0 & 0 & 0 \end{bmatrix} \mathbf{x} = \begin{bmatrix} 1 \\ 1 \end{bmatrix}$$

we measure the magnetic signature at different positions, hence the rows of matrix  $A$  are independent and therefore our discrete inverse problem is always consistent.

This means that we always encounter non-uniqueness of a solution of our inverse problem. To resolve this issue, we can enforce extra constraints on the solution that we seek. An example of such a constraint is given in example 3.3.1.

## 2.6.2 Different approach

In this chapter, we have derived the forward formulation of the magnetic field of some steel object  $\Omega$ , based on magnetization  $\mathbf{M}$ . Next, based on the forward formulation, an inverse formulation is derived. The Petrov-Galerkin method is used to reduce the inverse formulation to a discrete linear inverse problem (based on a predefined mesh of object  $\Omega$ ).

As explained in the introduction (section 1.3), Chadebec and his colleagues developed inverse formulations based on finding some magnetization  $\mathbf{M}$  of the steel object. In [26] they state that the magnetic field of some ferromagnetic material can be calculated via

$$\mathbf{H}_{red} = -\frac{1}{4\pi} \text{grad} \iiint_{\Omega} \mathbf{M} \cdot \frac{\mathbf{r} - \mathbf{r}'}{\|\mathbf{r} - \mathbf{r}'\|^3} d\Omega'$$

where  $\mathbf{M}$  is the magnetization of the ferromagnetic material  $\Omega$ . The inverse problem is finding the magnetization  $\mathbf{M}$  via

$$\mathbf{M} + \frac{\chi_r}{4\pi} \text{grad} \iiint_{\Omega} \mathbf{M} \cdot \frac{\mathbf{r} - \mathbf{r}'}{\|\mathbf{r} - \mathbf{r}'\|^3} d\Omega' = \chi_r \mathbf{H}_0$$

where  $\mathbf{H}_0$  is some external background field and  $\chi_r$  is the magnetic susceptibility.

We want to emphasize the different approach of our derivation of the inverse problem, compared to the approaches in [3, 26, 5]. While the above stated formulation searches for the magnetization, we are actually not interested in the specific magnetization  $\mathbf{M}$  of  $\Omega$  itself. We only need some description of the magnetic sources  $f, g$  and  $h$ , where  $f$  is (a discretised version of)  $\nabla \cdot \mathbf{M}$ ,  $h$  is one of  $\nu \cdot \mathbf{M}$  in  $\Omega$  and  $g$  a discretised version of  $\mathbf{n} \cdot \mathbf{M}$  on  $\partial\Omega$ . By this choice we believe that we can achieve better approximations of the magnetic sources. Furthermore, in our formulation we always find magnetic sources that come from a physical magnetization, whereas the formulation of Chadebec and his colleagues may produce magnetizations that are not physical.



## 3 Inverse Modeling Theory

### 3.1 Introduction

In this chapter we want to achieve two goals: we want to find a way to compute solutions of our inverse problem and we want to know how we can investigate the behavior of our inverse problem. We will explain what the ill-posedness of a inverse problem means and prove that our inverse problem (formulated in the previous Chapter) is ill-posed. To prove the ill-posedness we need some basic theory of inverse modeling.

We start this chapter with an introduction to the Forward operator. Many physical problems can be formulated as a so-called forward problem. Forward problems find the effect from causes. Given a forward problem, we can associate an inverse problem with it: determine the cause from effects. We illustrate the idea of a forward and inverse problem with an example and show that solving inverse problems can be very complex.

In section 3.3 we consider Hadamard's definition of a well posed problem. Problems that violate one of the criteria in this definition are called ill-posed. This implies that a problem is hard to solve or does not have a unique solution. In general, inverse problems are ill-posed.

Forward problems are often expressed in terms of an operator

$$T : \mathcal{X} \rightarrow \mathcal{Y}$$

between Hilbert spaces. One way of solving the associated inverse problem is by the use of the inverse operator of  $T$  but the solving becomes more complex if the inverse operator does not exist. Even if the operator is not invertible itself, one can still define some kind of inverse operator. This so-called generalized inverse of the operator  $T$  will take an important role in solving general inverse problems. We will describe in section 3.4 and 3.5 the construction of this generalized inverse and we will show how it can be used to solve inverse problems.

In section 3.6 we end the chapter with proving the claim that our inverse problem is ill-posed. In the proof we use all the techniques and theorems of this chapter.

### 3.2 Introduction to the Forward

In the field of the mathematical modeling we often want to compute some *effect* which is generated by some *cause* (figure 3.1). For example, when a violin is being played, the vibrations of the snares produce sound waves that we can hear. Here, the vibrations of the snares are the cause and the sound waves are the effect. The translation of the touch of a violin player and the movement of the string that is produced can be described well by the wave equation

$$\frac{\partial^2}{\partial t^2} u(x, t) = \nu_s^2 \frac{\partial^2}{\partial x^2} u(x, t), \quad \begin{cases} u(0, t) = u(l, t) = 0 \\ u(x, 0) = f(x) \end{cases} \quad \text{for all } 0 < x < l \text{ and } t > 0$$

where  $\nu_s$  is the speed of sound,  $l$  is the length of the string and  $u(x, t)$  is the sound-wave. The wave equation model thus describes the connection between the cause and its effect. Such a model is often called a *forward model* and the problem of computing the waves that are created by knowing the initial conditions of the snares is the so-called *forward problem*. In general physical, forward problems can be solved numerically quite accurately.

**Example 3.2.1** (Forward Heat Problem). Another example of a forward problem is the *forward heat equation* which can be used to compute the temperature distribution  $u$  in a one-dimensional steel rod  $\Omega$  of length  $l$  for some given heat sources  $f$ . The connection between  $u$  and the heat sources  $f$  is given by the following PDE:

$$\begin{cases} \frac{\partial}{\partial t} u(x, t) = k \frac{\partial^2}{\partial x^2} u(x, t) + f(x, t), & (x, t) \in \Omega \times (0, \infty) \\ u(0, t) = u(l, t) = 0 \\ u(x, 0) = g(x) \end{cases}$$

where  $k$  is the thermal conductivity and  $f$  consists of heat sources in  $\Omega$ . In this case the temperature at the ends of the rod is kept at zero degrees.

The forward problem is to determine the temperature distribution  $u$  given the heat sources  $f$ . This problem can be solved analytically because the boundary conditions of the PDE are homogeneous. A separation of variables leads to an analytical description of  $u$  in terms of the eigenfunctions of  $\nabla^2$  and  $\frac{\partial}{\partial t}$ . Because we have prescribed the function  $u$  at the boundaries there exists a unique solution.

We can also ask ourselves whether it is possible to determine the initial temperature distribution  $u(x, 0)$  when we know the distribution  $u(x, t')$  at time  $t'$ . Such problems focus on the determination of the cause given some known (measured) effect. It is

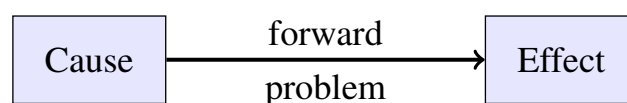


Figure 3.1: Forward Problem

precisely the opposite of a forward problem. Such problems are called *inverse problems*, see figure 3.2.

When considering inverse problems one wants to determine causes for some observed effects or one wants to determine material properties that can not be observed directly.

**Definition 3.2.1** (Inverse problem). Consider the Fredholm integral equation of the first kind

$$g(s) = \int_{\Omega} K(x, s)f(x)dx$$

where the (smooth) kernel  $K$  and the function  $g$  are known. The kernel represents the underlying (physical) model. The *inverse problem* consists of computing  $f$  given the function  $g$  and kernel  $K$ .

**Remark:** *Throughout this thesis we talk about a specific type of inverse problems, namely the task of approximating the sources that cause some measured effect. Therefore, if we talk about an inverse problem, we are always referring to such inverse problems.*

Return to the inverse problem. For the one-dimensional unbounded case (where  $\Omega = \mathbb{R}$ ,  $f = 0$  and  $k = 1$ ) the final temperature distribution  $u(x, T)$  at time  $T$  is related to the initial temperature distribution  $u(x, 0)$  via [7]

$$\frac{1}{2\sqrt{\pi T}} \int_{-\infty}^{\infty} u(s, 0) \exp\left(-\frac{(x-s)^2}{4T}\right) ds = u(x, T) \tag{3.1}$$

Such a problem can also be seen as an inverse problem, although in this case we are not looking for the sources that have caused the final temperature distribution but rather the initial temperature distribution.

The above equation is a so-called *convolution equation* with kernel

$$K(x, s) = \frac{1}{2\sqrt{\pi T}} \exp\left(-\frac{(x-s)^2}{4T}\right)$$

One can show that solutions of the above convolution equation are smooth due to the properties of the kernel  $k(x, s)$ . This makes the inverse problem very hard to solve as initial temperature distributions are not a priori smooth (if the initial temperature distribution  $u(s, 0)$  contains some discontinuities, then the smooth kernel resolves these in the final temperature distribution). The local variations in the initial temperature distribution cannot be well determined in an inverse problem.

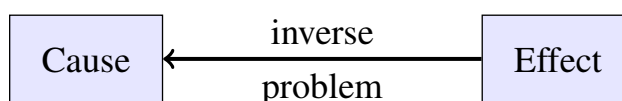


Figure 3.2: Inverse Problem

### 3.2.1 Smoothing properties of integral equations

The integral equation in its general form defined by

$$y(s) = \int_{\Omega} K(x, s) f(x) dx$$

has so-called smoothing properties. In the heat equation example, the function  $u(x, T)$  is in general much smoother compared to  $u(s, 0)$ . This behavior makes it hard to find the correct solutions of the inverse problem. The smoothing property of these integral operators is formulated in the following lemma of Riemann-Lebesgue.

**Riemann-Lebesgue Lemma.** Let  $K$  be a square-integrable function on the closed interval  $[a, b]^2$ . Then

$$y_1(s) = \int_a^b K(x, s) \sin(\lambda x) dx \rightarrow 0, \quad (\text{for } \lambda \rightarrow \pm\infty)$$

$$y_2(s) = \int_a^b K(x, s) \cos(\lambda x) dx \rightarrow 0, \quad (\text{for } \lambda \rightarrow \pm\infty)$$

*Proof.* A proof of the Riemann-Lebesgue lemma can be found in [8]. □

We can interpret this lemma<sup>1</sup> as follows. As the frequency  $\lambda$  increases, the amplitudes of the functions  $y_1$  and  $y_2$  decrease. So higher frequencies are being damped by the kernel  $K(s, t)$ , hence functions  $y_1$  and  $y_2$  become smoother by applying this integral operator with kernel  $K$  to function  $f(t)$ . Notice that the lemma is formulated for square-integrable functions only on compact intervals of  $\mathbb{R}^2$ . However, this theorem can be found in a more general setting.

If we consider the Riemann-Lebesgue lemma for *inverse* problems, the reverse happens: we observe that such a kernel  $K$  actually amplifies high frequencies and the higher the frequency, the more the amplification. This leads to large variations in the solution of the inverse problem. Furthermore, small perturbations in  $g_1$  and  $g_2$  can lead to very large perturbations of the source  $f$  when the perturbation of  $g_1$  and  $g_2$  contains a high frequency component.

This smoothing property of the forward problem is a huge problem from a fundamental point of view. It makes inverse problems significantly more complex and harder to “solve”.

### 3.2.2 General formulation

Consider some linear operator  $T$  between Hilbert spaces  $\mathcal{X}$  and  $\mathcal{Y}$  given by

$$T : \mathcal{X} \rightarrow \mathcal{Y}, \quad x \mapsto y := Tx$$

---

1. Observe that we can not apply this lemma to our Heat example. But by truncation of the indefinite integral in equation 3.1 to some definite integral on some closed interval  $[a, b]$  we are able to apply the Riemann-Lebesgue lemma.

The forward problem can be formulated in the following simple operator equation

$$y = Tx$$

where  $x$  is called the source and  $T$  is the so-called forward operator. The operator  $T : \mathcal{X} \rightarrow \mathcal{Y}$  maps source functions  $x \in \mathcal{X}$  onto functions  $y \in \mathcal{Y}$  that are caused by the sources  $x \in \mathcal{X}$ . The idea behind solving inverse problems is that – given some forward operator  $\mathcal{F}$  that describes the forward problem – we want to take the “inverse operator” of the forward operator. The expression

$$x = T^{-1}y$$

can only make sense whenever  $\mathcal{F}$  is invertible. But if the inverse operator does not exist, we want to come up with a way to define some operator that approximates the inverse operator. In the next section we introduce the notion of a pseudo-inverse and show that this operator can be used to solve the inverse problem for a special situation.

### 3.3 Hadamard’s well-posed problem

In 1902 Jacques Hadamard defined what properties a mathematical model of physical phenomena should have in order to represent the phenomena correctly. His notion of a *well-posed* problem is defined as follows

**Definition 3.3.1** (Hadamard). A problem is *well-posed* if the following three criteria holds:

1. **(Existence)** A solution exists of the problem, for all admissible data
2. **(Uniqueness)** The solution is unique, for all admissible data
3. **(Continuity)** The solution depends continuously on the data.

When a problem does not satisfy (at least) one of these conditions, the problem is called *ill-posed*. Examples of well-posed forward problems are the forward heat equation and the Dirichlet problem for Laplace’s Equation, under suitable boundary and initial conditions.

Inverse problems are often ill-posed. The inverse heat diffusion example is a typical example of an ill-posed problem. Small changes in the final temperature distribution  $u(x, T)$  lead to large changes in the solution  $u(x, 0)$ . We see that the third condition of Hadamard’s well-posedness is violated. Also, different initial temperature distributions can diffuse to the same final temperature  $u(x, T)$ , so the second criterion is also violated.

Hadamard’s definition as stated above is not a precise mathematical definition. A general inverse problem is of the form

$$y = Tx$$

where  $T$  is a bounded linear operator between Hilbert spaces  $\mathcal{X}$  and  $\mathcal{Y}$  and  $y$  is known. Then, the three criteria of Hadamard's well-posed problem can be formulated as: the operator  $T$  should be 1. **onto** (surjective), 2. **one-to-one** (injective) and the inverse operator  $T^{-1}$  should be **continuous**.

### 3.3.1 When a solution does not exist

Consider a bounded linear operator  $T \in \mathcal{L}(\mathcal{X}, \mathcal{Y})$  and an element  $y \in \mathcal{Y}$ . If the inverse problem  $Tx = y$  does not have a solution, then by Hadamard's definition of well-posedness the inverse problem is called ill-posed.

Recall the definition of the adjoint operator. The *adjoint operator*  $T^* : \mathcal{Y} \rightarrow \mathcal{X}$  is defined as the bounded linear operator such that

$$\langle Tx, y \rangle = \langle x, T^*y \rangle, \quad \text{for all } x \in \mathcal{X} \text{ and for all } y \in \mathcal{Y}$$

One way to resolve the lack of existence of solutions is to look for *least-squares solutions*. This is done by solving the normal equations

$$T^*Tx = T^*y$$

where  $T^*$  is defined as the adjoint operator of  $T$ . In the next section we explain what a least-squares solution of the equation  $Tx = y$  is.

### 3.3.2 When a problem is not one-to-one

If a bounded linear operator  $T$  is not one-to-one, then its kernel  $\mathcal{N}(T)$  is non-trivial, i.e., if for  $y \in \mathcal{Y}$  there exists some  $x \in \mathcal{X}$  such that  $Tx = y$  then for every  $z \in \mathcal{N}(T)$  we have

$$T(x + z) = Tx + Tz = y + 0 = y$$

So the solution  $x$  is not unique and in particular any element in the set  $x + \mathcal{N}(T)$  is a solution of the equation  $Tx = y$ . Whenever this problem occurs one can try to add additional information to make the solution  $x$  unique.

To illustrate the violation of the second criterion of Hadamard's well-posed problem, we look at the following simple example.

**Example 3.3.1.** Consider the following linear equation

$$3x + 5y = 2, \quad \mathbf{x} = (x, y) \in \mathbb{R}^2 \tag{3.2}$$

Observe that the equation  $3x + 5y = 0$  has infinite many solutions, so the solution of 3.2 is not unique. Therefore, the second criterion of Hadamard's well-posed problem is violated and the problem is ill-posed. The solutions of the system are given by

$$\mathbf{x} = \begin{bmatrix} -1 \\ 1 \end{bmatrix} + \alpha \begin{bmatrix} 5 \\ -3 \end{bmatrix}$$

By adding additional information we can change the problem so it has a unique solution. We can, for example, demand that the 2-norm of the solution is minimal. The adjusted problem is given by

$$3x + 5y = 2 \quad \text{subjected to} \quad \min \|\mathbf{x}\|_2, \quad \mathbf{x} = (x, y) \in \mathbb{R}^2 \quad (3.3)$$

To solve the adjusted problem we consider the function

$$\varphi(\alpha) := \|\mathbf{x}\|_2^2 = 34\alpha^2 - 16\alpha + 2$$

We compute for which  $\alpha$  the function  $\varphi(\alpha)$  is minimal. It follows that  $\alpha = \frac{4}{17}$  minimizes  $\varphi$ . Hence

$$\mathbf{x} = \begin{bmatrix} -1 \\ 1 \end{bmatrix} + \frac{4}{17} \begin{bmatrix} 5 \\ -3 \end{bmatrix} = \frac{1}{17} \begin{bmatrix} 3 \\ 5 \end{bmatrix}$$

is *the* solution of problem 3.3.

In the example we have seen that adding extra constraints can resolve the issue of non-uniqueness of the solution. Recall that our discrete inverse problem has non-unique solutions and therefore we need to add extra constraints to our inverse problem as well.

This so-called *regularization* of the inverse problem is a way to resolve the issue of non-uniqueness of a problem.

### 3.3.3 When the solution of an inverse problem does not depend continuously on the data

Violation of the third criterion of Hadamard's definition creates serious numerical problems. If we want to approximate a problem whose solution does not continuously depend on the data, we have to expect that traditional numerical solvers becomes unstable. Small changes in the data lead to large variations in the computed solutions.

A remedy for this is the use of "regularization methods". A regularization methods tends to recover partial information from the given solution as stable as possible, at the cost of accuracy. Therefore, when we apply regularization methods we have to find a good balance between stability of the solutions and accuracy.

In chapter 4 we cover a more general overview on regularization methods and we will see how regularization methods try to resolve the issue of discontinuity.

### 3.4 Generalized inverse

In this section we define the generalized inverse of an operator  $T \in \mathcal{L}(\mathcal{X}, \mathcal{Y})$  where  $\mathcal{X}, \mathcal{Y}$  are Hilbert spaces. We end by proving that the pseudo-inverse of a bounded linear operator can be used to compute a least-square solution of minimal norm of the operator equation  $Tx = y$ . The theory summarized in this section can be found in [7], Chapter 2.

#### 3.4.1 Least-squares and best-approximate solutions

First a definition.

**Definition 3.4.1.** *Let  $T : \mathcal{X} \rightarrow \mathcal{Y}$  be a bounded linear operator between Hilbert spaces  $\mathcal{X}$  and  $\mathcal{Y}$ . Then*

(i)  $x \in \mathcal{X}$  is called a least-squares solution of  $Tx = y$  if

$$\|Tx - y\| = \inf\{\|Tz - y\| : z \in \mathcal{X}\}.$$

(ii)  $x \in \mathcal{X}$  is called the best-approximate solution of  $Tx = y$  if

$$\|x\| = \inf\{\|z\| : z \text{ is a least-squares solution of } Tx = y\}.$$

The best-approximate solution is thus defined as the least-square solution with minimal norm. Note that, when  $\mathcal{X}$  is a Hilbert space, the set of all least-squares solutions is closed, hence the best-approximation is unique. This is a standard result in Hilbert theory.

Abstract as it may seem, this concept of best-approximated solution has an applied side. The actual state of a physical system is usually that with the smallest energy. In many cases, the energy is formulated by a certain norm and so “minimal energy” is then equivalent to “minimal norm”, hence a best approximation problem.

#### 3.4.2 Restriction of $T$

Recall that for an operator  $T : \mathcal{X} \rightarrow \mathcal{Y}$  (not necessarily bounded) the null-space of  $T$  is defined as  $\mathcal{N}(T) = \{x \in \mathcal{X} : Tx = 0\}$  (which is a subset of  $\mathcal{X}$ ). The range (or image) of  $T$  is defined as  $\mathcal{R}(T) = \{Tx : x \in \mathcal{X}\}$  (which is a subset of  $\mathcal{Y}$ ). For any subspace  $\mathcal{Z} \subseteq \mathcal{X}$ , the *restriction* of  $T$  to  $\mathcal{Z}$  is defined as

$$T \upharpoonright_{\mathcal{Z}} : \mathcal{Z} \rightarrow \mathcal{Y}, \quad T \upharpoonright_{\mathcal{Z}}(z) = T(z)$$

In the construction of the generalized inverse we need the following lemma.

**Lemma 3.4.1.** *Let  $T \in \mathcal{L}(\mathcal{X}, \mathcal{Y})$  be some bounded linear operator and let  $\mathcal{X}, \mathcal{Y}$  be Hilbert spaces. Then  $\tilde{T}$ , the restriction of operator  $T$ , given by*

$$\tilde{T} := T \upharpoonright_{\mathcal{N}(T)^\perp} : \mathcal{N}(T)^\perp \rightarrow \mathcal{R}(T)$$

*is an invertible bounded linear operator.*

*Proof.* Given that  $T$  is a bounded linear operator it follows immediately that  $\tilde{T}$  is also a bounded linear operator. We claim that  $\tilde{T}$  is invertible. Since the domain of  $\tilde{T}$  is  $\mathcal{N}(T)^\perp$  we have that  $\mathcal{N}(\tilde{T}) = \{0\}$  by construction. Thus  $\tilde{T}$  is injective. Furthermore since  $\mathcal{R}(\tilde{T}) = \mathcal{R}(T)$  we have that  $\tilde{T}$  is surjective. Hence  $\tilde{T}$  is bijective and thus  $\tilde{T}$  is invertible. Lastly as  $\tilde{T}^{-1}$  exists it is also a linear<sup>2</sup> operator.  $\square$

By restricting the operator  $T$  its domain to  $\mathcal{N}(T)^\perp$  and its co-domain to  $\mathcal{R}(T)$ , the restriction is invertible. So we have found a part of the operator  $T$  that we can use in inverse problems to produce potential solutions. However, as we will see, the use of the restriction comes at a cost. This will be explained in section 3.4.7.

### 3.4.3 Generalized Inverse

For any two subspaces  $U, V \subseteq \mathcal{X}$  with  $U \cap V = \{0\}$  of some vector space  $\mathcal{X}$ , its *direct sum*  $U \oplus V$  is defined as

$$w \in U \oplus V \quad \text{if and only if} \quad (\exists!u)(\exists!v)(w = u + v)$$

The generalized inverse (or the so-called Moore-Penrose generalized inverse) is formulated as follows.

**Definition 3.4.2** (generalized inverse). *Let  $T \in \mathcal{L}(\mathcal{X}, \mathcal{Y})$  be some bounded linear operator between Hilbert spaces  $\mathcal{X}$  and  $\mathcal{Y}$ . The Moore-Penrose generalized inverse  $T^\dagger$  is defined as the unique linear extension of  $\tilde{T}^{-1}$  to the domain  $\mathcal{D}(T^\dagger)$ :*

$$\mathcal{D}(T^\dagger) := \mathcal{R}(T) \oplus \mathcal{R}(T)^\perp$$

with  $T^\dagger y = \tilde{T}^{-1}y$  if  $y \in \mathcal{R}(T)$  and  $T^\dagger y = 0$  if  $y \in \mathcal{R}^\perp$ .

We have to check that the generalized inverse operator is well-defined. Due to the construction of the kernel of  $\tilde{T}^{-1}$  and the linearity we have for any  $y \in \mathcal{D}(T^\dagger)$  with the unique representation

$$y = y_1 + y_2, \quad y_1 \in \mathcal{R}(T), y_2 \in \mathcal{R}(T)^\perp$$

that the image  $T^\dagger y$  of  $y$  under  $\tilde{T}$  is given by

$$T^\dagger y = T^\dagger y_1 + T^\dagger y_2 = T^\dagger y_1 + 0 := \tilde{T}^{-1}y_1$$

So  $T^\dagger$  is well-defined as a linear operator from  $\mathcal{D}(T^\dagger)$  to  $\mathcal{N}(T)^\perp$ .

The above definition of the generalized inverse tells us how to construct the generalized inverse. However, the discussed approach is rather cumbersome. In section 3.5 we discuss the construction of the generalized inverse by means of a singular value decomposition of the operator  $T$ .

---

2. Use that  $T^{-1} \circ T = Id$  for any invertible operator  $T$  and use the linearity of  $T$  to deduce the linearity of  $T^{-1}$ .

### 3.4.4 Generalized inverse as a projection

Now that the generalized inverse operator has been introduced, we will work our way to the theorem that states that the generalized inverse can be used to produce some best-approximate solution of the equation

$$Tx = y$$

For any subspace  $\mathcal{Z} \subseteq \mathcal{X}$  define the *closure*  $\overline{\mathcal{Z}}$  as the smallest closed set that contains  $\mathcal{Z}$ , or equivalently as the set of all limit points of all convergent sequences of points in  $\mathcal{Z}$ .

The following proposition shows properties of the generalized inverse as a projection. We omit the proof.

**Proposition 3.4.1.** *Let  $P$  and  $Q$  be the orthogonal projections onto  $\mathcal{N}(T)$  and  $\overline{\mathcal{R}(T)}$ , respectively. Then  $\mathcal{R}(T^\dagger) = \mathcal{N}(T)^\perp$ , and the four “Moore-Penrose equations” hold:*

$$TT^\dagger T = T, \tag{3.4}$$

$$T^\dagger TT^\dagger = T^\dagger, \tag{3.5}$$

$$T^\dagger T = I - P, \tag{3.6}$$

$$TT^\dagger = Q \upharpoonright_{\mathcal{D}(T^\dagger)}. \tag{3.7}$$

$$\tag{3.8}$$

Furthermore we have that  $(TT^\dagger)^* = TT^\dagger$ , i.e.,  $TT^\dagger$  is self-adjoint.

For clarification: we consider the operators  $P : \mathcal{X} \rightarrow \mathcal{N}(T)$  and  $Q : \mathcal{Y} \rightarrow \overline{\mathcal{R}(T)}$  as orthogonal projections onto the subspaces  $\mathcal{N}(T)$  and  $\overline{\mathcal{R}(T)}$ . Both the co-domains of the operators  $P$  and  $Q$  are *closed* in the Hilbert spaces  $\mathcal{X}$  and  $\mathcal{Y}$  respectively. This ensures us that both projectors are well-defined and that the projection  $Px$  for some  $x \in \mathcal{X}$  is unique (a standard result in the Hilbert spaces theory).

The self-adjointness of  $TT^\dagger$  is evident as it is an orthogonal projector on a Hilbert space.

### 3.4.5 The generalized inverse yields the best-approximate solution

We prove the connection between the best-approximate least-squares solution and the generalized inverse.

**Theorem 3.4.3.** *Let  $T \in \mathcal{L}(\mathcal{X}, \mathcal{Y})$  be a bounded linear operator between Hilbert spaces  $\mathcal{X}$  and  $\mathcal{Y}$ . Let  $y \in \mathcal{D}(T^\dagger)$ . Then the operator equation  $Tx = y$  has a best-approximate solution, which is given by*

$$x^\dagger := T^\dagger y$$

*Proof.* Let  $T \in \mathcal{L}(\mathcal{X}, \mathcal{Y})$  be a bounded linear operator between Hilbert spaces  $\mathcal{X}$  and  $\mathcal{Y}$  and let  $y \in \mathcal{D}(T^\dagger)$ . The proof consists of two parts. First we derive a concrete set of least-squares solutions  $\mathcal{S}$ . After that we show that the element of minimal norm  $\bar{z} \in \mathcal{S}$  in this set is in fact the element  $z = T^\dagger y$ .

Define the set

$$\mathcal{S} := \{w \in \mathcal{X} : Tw = Qy\}$$

where  $Q$  is the orthogonal projector in proposition 3.4.1. Since

$$\mathcal{D}(T^\dagger) = \mathcal{R}(T) \oplus \mathcal{R}(T)^\perp$$

we have that  $Qy \in \mathcal{R}(T)$ , hence  $\mathcal{S}$  is nonempty. We will show that  $\mathcal{S}$  is the set of all least-squares solutions of  $Tx = y$ .

Observe that the operator  $Q$  is also a metric operator<sup>3</sup> on the Hilbert space  $\mathcal{Y}$ , which implies for all  $w \in \mathcal{S}$  that

$$\|Tw - y\| = \|Qy - y\| \leq \|Tz - y\|, \quad \text{for all } z \in \mathcal{X}$$

So we see that every element  $w \in \mathcal{S}$  is a least-squares solution of the operator equation  $Tx = y$ . Conversely let  $z$  be some least-squares solution of the equation  $Tx = y$ . Then using that  $Q$  is a metric projector and the definition of a least-squares solution we have that

$$\|Qy - y\| \leq \|Tz - y\| = \inf\{\|u - y\| : u \in \mathcal{R}(T)\} = \|Qy - y\|$$

So we see that  $Tz$  is an element in  $\mathcal{R}(T)$  that is the closest to  $y$ . Using the uniqueness of the orthogonal projection we conclude that  $Tz = Qy$ . Hence

$$\mathcal{S} = \{x \in \mathcal{X} : x \text{ is a least-squares solution of } Tx = y\}$$

Let  $\bar{z}$  be the element of minimal norm in  $\mathcal{S}$ . This element can be found as the orthogonal projection of  $x = 0$  onto the closed linear manifold  $\mathcal{S}$ , as the element  $\bar{z}$  satisfies

$$\|\bar{z}\| = \|\bar{z} - 0\| := \inf_{u \in \mathcal{S}} \|u - 0\| = \inf_{u \in \mathcal{S}} \|u\|$$

Hence we can write  $\mathcal{S} = \bar{z} + \mathcal{N}(T)$ .

We claim that  $\bar{z}$  is orthogonal to  $\mathcal{N}(T)$ . Assume that  $\|\bar{z}\|$  is of minimal norm and that  $\bar{z}$  is not orthogonal to  $\mathcal{N}(T)$ , so  $P\bar{z} \neq 0$ . Let  $P$  be the orthogonal projector onto the subspace  $\mathcal{N}(T)$ , see figure 3.3. Then  $\bar{z} = P\bar{z} + (\bar{z} - P\bar{z})$ . The element  $w = \bar{z} - P\bar{z}$  then is smaller in norm, contradicting the assumption that  $\bar{z}$  is of minimal norm. Hence  $\bar{z} \in \mathcal{N}(T)^\perp$ . Hence  $P\bar{z} = 0$ . This yields

$$\bar{z} = \bar{z} - P\bar{z} = (I - P)\bar{z} = T^\dagger T\bar{z} = T^\dagger Qy = T^\dagger TT^\dagger y = T^\dagger y$$

So the best-approximate least-squares solution is given by  $\bar{z} = T^\dagger y$ .  $\square$

3. A metric operator  $Q : \mathcal{Y} \rightarrow \overline{\mathcal{R}(T)}$  maps elements  $y$  to the closest element  $z \in \overline{\mathcal{R}(T)}$  in distance:  $d(y, z) = \inf\{d(y, w) : w \in \overline{\mathcal{R}(T)}\}$ . The distance function in a Hilbert space is given by  $d(x, y) = \|x - y\|$ .

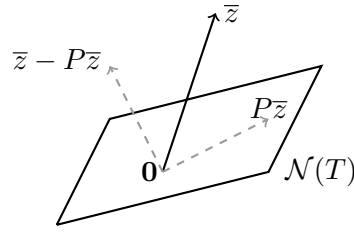


Figure 3.3: The vector  $\bar{z}$  and its projection  $P\bar{z}$  onto  $\mathcal{N}(T)$ .

**Corollary 3.4.1.** *Let  $y \in \mathcal{D}(T^\dagger)$ . Then  $x \in \mathcal{X}$  is a least-squares solution of  $Tx = y$  if and only if the normal equation*

$$T^*Tx = T^*y$$

*holds.*

*Proof.* Let  $y \in \mathcal{D}(T^\dagger)$  and let  $T^* : \mathcal{Y} \rightarrow \mathcal{X}$  denote the adjoint operator of  $T$ . Then  $x \in \mathcal{X}$  is a least-squares solution if and only if  $Tx - y \in \mathcal{R}(T)^\perp$ . The relationship<sup>4</sup> between the image of  $T$  and the kernel of the adjoint is given by

$$\mathcal{N}(T^*) = \mathcal{R}(T)^\perp$$

so that  $x$  is a least-squares solution if and only if  $Tx - y \in \mathcal{N}(T^*)$ , i.e.,  $T^*(Tx - y) = 0$  or  $T^*Tx = T^*y$ .  $\square$

It follows from this corollary that the best-approximate least-squares solution  $\bar{z} = T^\dagger y$  is one of the solutions of  $T^*Tx = T^*y$ . Using the generalized inverse of  $T^*T$ , the best approximate solution of the normal equations is given by

$$z^\dagger = (T^*T)^\dagger T^*y$$

Hence by comparison the expressions of  $x^\dagger$  and  $z^\dagger$  we have

$$T^\dagger = (T^*T)^\dagger T^*$$

This result is used in the next section to derive an analytical expression for the generalized inverse of matrices.

### 3.4.6 The generalized inverse and ill-posedness

We end this section with a theorem that can be used when we want to prove that an inverse problem is ill-posed. Before proving the theorem we recall the following definition of a compact operator.

**Definition 3.4.1** (Compact operator). Let  $T : X \rightarrow Y$  be a linear operator between Banach spaces  $X$  and  $Y$ . Then  $T$  is a compact operator if for any bounded sequence  $(x_n)_n$  in  $X$  we have that  $(Tx_n)_n$  has a convergent subsequence in  $Y$ .

4.  $T^*x = 0$  if and only if  $\langle T^*x, t \rangle = 0$  for all  $t \in \mathcal{X}$ . By definition this is equivalent to saying that this holds if and only if  $\langle x, Tt \rangle = 0$  for all  $t \in \mathcal{X}$  and this is equivalent to saying that  $x \perp \mathcal{R}(T)$ .

**Theorem 3.4.4.** *Let  $T : \mathcal{X} \rightarrow \mathcal{Y}$  be a compact bounded operator such that  $\mathcal{R}(T)$  is infinite dimensional. Then  $T^\dagger$  is a discontinuous operator.*

*Proof.* Let  $\mathcal{X}$  and  $\mathcal{R}(T)$  be infinite-dimensional spaces. As  $\mathcal{N}(T)^\perp$  is mapped onto  $\mathcal{R}(T)$  by the operator  $\tilde{T}$  (the map  $\tilde{T}$  is surjective), it is also infinite-dimensional. Hence, we can find a sequence<sup>5</sup>  $(x_n)_n$  with

$$x_n \in \mathcal{N}(T)^\perp, \|x_n\| = 1, \quad \text{and } \langle x_n, x_k \rangle = 0 \quad \text{for } k \neq n$$

Using that the operator  $T$  is compact gives us that the sequence  $(y_n)_n := (Tx_n)_n$  has a convergent subsequence.

Now fix  $\varepsilon > 0$ . Then there is an  $N \in \mathbb{N}$  such that for  $k, l \geq N$  we have  $\|y_l - y_k\| < \varepsilon$  (as the convergent subsequence of  $(y_n)_n$  is Cauchy). This implies

$$\begin{aligned} \|T^\dagger y_k - T^\dagger y_l\|^2 &= \|x_k - x_l\|^2 \\ &= \|x_k\|^2 + \|x_l\|^2 - 2\langle x_l, x_k \rangle \\ &= 2 \end{aligned}$$

As  $\varepsilon$  was arbitrary this implies that  $T^\dagger$  is unbounded. Thus  $T^\dagger$  is not continuous.  $\square$

So when a compact operator  $T$  (that is involved in an inverse problem) satisfies the above assumptions, then its generalized inverse is not continuous. By Hadamard's definition of a well-posed problem we conclude that the inverse problem is ill-posed.

### 3.4.7 Remark on using the generalized inverse as a best-approximate solution

The concept of the generalized inverse gives us a way to compute best-approximate solutions of the equation  $Tx = y$  whenever  $y \in \mathcal{D}(T^\dagger)$ . This inverse operator forces uniqueness upon the solution that we seek, by forcing the solution to have minimal norm amongst all possible least-squares solutions.

When  $y \notin \mathcal{D}(T^\dagger)$ , one can prove that no solution exists for the operator equation  $Tx = y$ ; therefore, we have to be careful when we apply the generalized inverse operator in our computations. However, when we consider discrete linear inverse problems this problem does not occur. In general discrete linear inverse problems have infinite many solutions.

---

5. The sequence can be found by applying the Gram-Schmidt procedure on a basis of the *infinite-dimensional* Hilbert space  $\mathcal{N}(T)^\perp$ ; such a basis has infinite size. The existence of such a basis is proven by Zorn's Lemma.

### 3.5 Construction of the generalized inverse for finite-dimensional compact operators

In this section we consider the construction of the generalized inverse of a compact finite-dimensional operator, i.e. a matrix operator. The construction can be easily extended to infinite-dimensional compact operators. However, in this thesis we use the Petrov-Galerkin method to reduce our inverse problem to a finite-dimensional inverse problem, so we limit ourselves to the finite-dimensional operators.

Let  $A \in \mathbb{R}^{n \times m}$  be some real-valued  $n \times m$  matrix. In [24] it is proven that for any real-valued  $n \times m$  matrix there exists a singular value decomposition of the form

$$A = U\Sigma V^T$$

where  $U$  and  $V$  are orthogonal matrices and  $\Sigma$  is a diagonal matrix containing the non-zero singular values of  $A$ . Let  $\mathbf{u}_n$  and  $\mathbf{v}_n$  denote the columns of the orthogonal matrices  $U$  and  $V$ , let  $\sigma_n$  be the singular values of  $A$  defined by

$$A\mathbf{v}_n = \sigma_n \mathbf{u}_n$$

then the triple  $(\sigma_n, \mathbf{u}_n, \mathbf{v}_n)$  is called a singular system and using this system we obtain

$$A\mathbf{x} = \sum_{n=1}^r \sigma_n \langle \mathbf{x}, \mathbf{v}_n \rangle \mathbf{u}_n, \quad \text{for any vector } \mathbf{x} \in \mathbb{R}^m$$

where  $r = \text{rank}(A)$ , so the matrix  $A$  has  $r$  nonzero singular values. For  $A^T$ , the adjoint<sup>6</sup> of  $A$ , we can derive<sup>7</sup> in a similar way a singular system. We have

$$A^T \mathbf{y} = \sum_{n=1}^r \sigma_n \langle \mathbf{y}, \mathbf{u}_n \rangle \mathbf{v}_n, \quad \text{for any vector } \mathbf{y} \in \mathbb{R}^n$$

Note that  $A^\dagger = (A^T A)^\dagger A^T$  (see previous section) and hence for  $\mathbf{x}^\dagger = A^\dagger \mathbf{y}$  we have

$$\sum_{n=1}^r \sigma_n^2 \langle \mathbf{x}^\dagger, \mathbf{v}_n \rangle \mathbf{v}_n = A^T A \mathbf{x}^\dagger = (A^T A)(A^T A)^\dagger A^T \mathbf{y} = A^T \mathbf{y} = \sum_{n=1}^r \sigma_n \langle \mathbf{y}, \mathbf{u}_n \rangle \mathbf{u}_n$$

We see by comparing the individual components that it holds that

$$\langle \mathbf{x}^\dagger, \mathbf{v}_n \rangle = \frac{1}{\sigma_n} \langle \mathbf{y}, \mathbf{u}_n \rangle$$

Therefore<sup>8</sup> the best-approximate solution of  $A\mathbf{x} = \mathbf{y}$  is given by (see theorem 3.4.3)

$$\mathbf{x}^\dagger = A^\dagger \mathbf{y} = \sum_{n=1}^r \frac{\langle \mathbf{y}, \mathbf{u}_n \rangle}{\sigma_n} \mathbf{v}_n \quad (3.9)$$

6. For any  $m \times n$  matrix  $A$ , the adjoint  $A^T$  of  $A$ , is defined through  $\langle A\mathbf{x}, \mathbf{y} \rangle = \langle \mathbf{x}, A^T \mathbf{y} \rangle$  for all  $\mathbf{x} \in \mathbb{R}^m$  and for all  $\mathbf{y} \in \mathbb{R}^n$ .

7. The prove is based on the fact that the eigenvalues of the matrices  $A^T A$  and  $A A^T$  are the same. Using this property the singular value system follows directly by the same derivation.

8.  $A\mathbf{x}^\dagger = \sum_{n=1}^r \frac{\langle \mathbf{y}, \mathbf{u}_n \rangle}{\sigma_n} A\mathbf{v}_n = \sum_{n=1}^r \langle \mathbf{y}, \mathbf{u}_n \rangle \mathbf{u}_n = \mathbf{y}$ .

The pseudo-inverse of  $A$  can be written compactly in the following form (note that  $\Sigma^\dagger = \Sigma^{-1}$ )

$$A^\dagger = (U\Sigma V^T)^\dagger = V\Sigma^\dagger U^T$$

So the best-approximate solution of the system  $A\mathbf{x} = \mathbf{y}$  can be computed relatively easily when the singular value decomposition of  $A$  is known. However, for large systems the numerical computation of the singular value decomposition becomes unreliable. Therefore when one encounters large systems of equations one should avoid the use of a singular value decomposition in their computations.

### 3.6 Ill-posed inverse problem

By Hadamard's definition of a well-posed problem, an inverse problem is ill-posed if it violates one of the three conditions. In this section we claim that our general inverse problem (the non-discretized version) is ill-posed.

#### 3.6.1 Finite-dimensional inverse problem

For our finite dimensional inverse problem (after discretisation) it is evident that it is ill-posed. Suppose that we have a finite number of measurements such that the discrete inverse problem is under determined. After discretisation of the integral equation we are left with the consistent system of linear equations

$$A\mathbf{p} = \mathbf{b}$$

as shown in the previous sections. Because  $A$  is an  $m \times n$  matrix, where  $m \ll n$ , it follows that the null-space of  $K$  is nontrivial. Let  $\mathbf{p}$  be some solution of the system  $A\mathbf{p} = \mathbf{b}$ . Then the set of all solutions of the linear system is given by

$$\mathbf{p} + \mathcal{N}(A)$$

Hence there exist many source functions  $f, g$  and  $h$  that satisfy the finite-dimensional inverse problem, irrespective of the number of measurements. Therefore *uniqueness* is violated and thus the finite-dimensional problem is ill-posed.

However we claim that the inverse problem is also at a fundamental level ill-posed. In the next subsection we prove that our inverse problem does not satisfy the third condition of Hadamard's definition of a well posed problem.

#### 3.6.2 Proof of the claim

To show that the inverse problem we consider is ill-posed, we reduce our problem to the following one-dimensional case. It is clear that the derivations in the one-dimensional case can be generalised to the three-dimensional case.

Define  $T : \mathcal{L}_2([-1, 1]) \rightarrow \mathcal{L}_2(C)$  to be the bounded linear integral operator

$$(Tf)(x) = \int_{-1}^1 \frac{x - x'}{|x - x'|^3} f(x') dx'$$

where  $C \subset \mathbb{R} \setminus [-1, 1]$  is some compact subset. The boundedness of  $T$  follows from theorem 2.13 in [18]. We start by showing that  $T$  is a compact operator.

We claim that the kernel of  $T$  is square integrable. Indeed, we have the following estimate of the kernel  $K(x, x')$ :

$$\begin{aligned} \|K\|_2 &= \int_C \int_{[-1, 1]} |K(x, x')|^2 d(x', x) \\ &= \int_C \int_{[-1, 1]} \frac{1}{(x - x')^4} d(x', x) \\ &= \frac{1}{3} \int_C \frac{1}{(x - 1)^3} - \frac{1}{(x + 1)^3} dx \\ &\leq \frac{1}{3} \mu(C) \cdot \max_{x \in C} \left( \frac{1}{(x - 1)^3} - \frac{1}{(x + 1)^3} \right) \\ &< \infty \end{aligned}$$

Here the volume of  $C$  is finite (as it is a compact subset) and the function

$$x \mapsto \frac{1}{(x - 1)^3} - \frac{1}{(x + 1)^3}$$

is continuous on the compact set  $C$ , so it has a maximum. Hence we have that  $K \in \mathcal{L}_2(C \times [-1, 1])$ . We conclude that the operator  $T$  is compact.

For given  $g \in \mathcal{L}_2(C)$  the inverse problem is to find a function  $f \in \mathcal{L}_2([-1, 1])$  such that  $Tf = g$  holds. We claim that the image of  $T$  is infinite-dimensional. To this end assume that  $f \in \mathcal{L}_2([-1, 1])$  and assume without loss of generality that  $C \subset (1, \infty)$ . This means that

$$(Tf)(x) = \int_{-1}^1 \frac{x - x'}{|x - x'|^3} f(x') dx', \quad x \in C$$

can be simplified to

$$(Tf)(x) = \int_{-1}^1 \frac{1}{(x - x')^2} f(x') dx', \quad x \in C$$

Let  $(x_i)_{i=1}^{\infty}$  be the sequence in  $[-1, 1]$  defined by  $x_i = (1/2)^i$  and define  $\varepsilon_i = (1/2)^{i+2}$ . For each  $i$  define on the interval  $[-1, 1]$  the characteristic function

$$f_i(x') = \chi_{[x_i - \varepsilon_i, x_i + \varepsilon_i]}(x')$$

Clearly each  $f_i$  belongs to  $\mathcal{L}^2([-1, 1])$  and for  $i \neq j$  the support of the functions  $f_i$  and  $f_j$  are disjoint. Furthermore we have

$$(Tf_i)(x) = \int_{x_i - \varepsilon_i}^{x_i + \varepsilon_i} \frac{1}{(x_i - x')^2} dx' = \frac{1}{x - (x_i + \varepsilon_i)} - \frac{1}{x - (x_i - \varepsilon_i)}$$

Observe now that all elements  $Tf_i$  belong to  $\mathcal{L}^2(C)$  as

$$\|Tf_i\|_2 \leq \|K\|_2$$

and that the poles of the functions  $Tf_i$  are all mutually disjoint. This implies that the functions  $(Tf_i)_i$  are linearly independent so

$$W = \text{Span}(Tf_i : i \in \mathbb{N})$$

is an infinite dimensional subspace of  $\mathcal{L}^2(C)$ . But each  $Tf_i \in \mathcal{R}(T)$  thus  $\mathcal{R}(T)$  is also infinite dimensional. Now by applying theorem 3.4.4 we conclude that the generalised inverse of  $T$  is a discontinuous operator. By Hadamard's well-posed criteria, we conclude that the inverse problem is ill-posed, as the third condition (continuity) is violated.



## 4 Regularization Methods and Numerical Solvers

We have seen in the previous chapter that our inverse problem is ill-posed, according to Hadamard's definition of well posedness. We proved that the pseudoinverse is an unbounded operator, and therefore, the third criterion is violated (continuity). Furthermore, by reducing the inverse problem to a discrete version we have seen that the discrete inverse problem has infinite many solutions, which means that the second criterion of Hadamard's definition is also violated (uniqueness of the solution). We discussed a solution this by enforcing an extra constraint on the solution, to make it unique. We postponed solutions for the discontinuous behavior of solutions on the data. In this chapter we will answer the question how we can deal with such ill-posedness.

Considering the noise in measured data and the ill-posed behavior of inverse problems, solving an inverse problem is (very) complex. Ordinary application of the pseudoinverse to obtain a solution simply fails. Reducing an inverse problem to a finite-dimensional problem (for instance using the Petrov-Galerkin Method in Chapter 2) leads to solving a discrete inverse problem of the form

$$Ax = b \tag{4.1}$$

Such discrete problems inherit the ill-posed properties of the inverse problems: the condition number of the matrix  $A$  becomes very large. The matrix  $A$  is then called *ill-conditioned*. Solving ill-conditioned problems is hard because solutions become very sensitive to small perturbations in the right-hand side  $b$ . Therefore one has to add additional information about the solution  $x$  in order to produce feasible solutions. This is called *regularization* of the solution. Also, the high condition number may make the use of direct solving methods useless. Hence we need to consider more advanced solvers that can produce good solutions.

In this chapter we start with answering the question why we need regularization. Then, we discuss several standard regularization methods that give us insight in the fundamental ideas behind regularization. We give a brief explanation about the regularization methods. A detailed overview of these methods can be found in [10].

In the second part of this chapter, we recall the basic ideas behind direct solvers and the iterative methods. We discuss the so-called conjugate gradient least squares method (abbreviated by CGLS), which is a small extension of the ordinary CG method to the non-symmetrical case. This method can be used to solve our inverse problem.

## 4.1 Why do we need regularization?

For this moment consider a linear system of the form

$$Ax = \mathbf{b}_e + \mathbf{e}$$

where  $A$  is some rectangular  $m \times n$  matrix and  $\mathbf{e}$  is some noisy term in the right-hand side of the system. Let  $\mathbf{x}_e$  denote the exact solution of the system when there is no noise ( $\mathbf{e} = \mathbf{0}$ ). Furthermore denote the condition number of a matrix  $A$  by  $\kappa(A)$ , where  $\kappa(A)$  is defined as

$$\kappa(A) := \|A\|_2 \|A^\dagger\|_2 = \frac{\sigma_{\max}}{\sigma_{\min}},$$

i.e., the quotient of the largest and smallest singular value of  $A$ . Here, the Euclidean norm of a matrix is defined by

$$\|A\|_2 := \sup_{\mathbf{x} \neq \mathbf{0}} \frac{\|A\mathbf{x}\|_2}{\|\mathbf{x}\|_2}$$

and one can prove that there is an equivalent formula for the Euclidean norm given by

$$\|A\|_2 = \sqrt{\lambda_{\max}(A^T A)} = \sigma_{\max}(A)$$

For ill-posed problems we expect that the corresponding linear problem  $A\mathbf{x} = \mathbf{b}$  has a large condition number in the order of  $10^6$  or more. The consequence of large condition numbers is stated in the following classical result from perturbation theory.

**Theorem 4.1.1.** *Suppose that  $A \in \mathbb{R}^{m \times n}$  is a rectangular matrix. Let  $\mathbf{b}, \mathbf{e} \in \mathbb{R}^m$  be some nonzero vectors and assume that  $A\mathbf{x}_e = \mathbf{b}$  and  $A\mathbf{x} = \mathbf{b} + \mathbf{e}$  holds. Then*

$$\frac{\|\mathbf{x} - \mathbf{x}_e\|_2}{\|\mathbf{x}_e\|_2} \leq \kappa(A) \frac{\|\mathbf{e}\|_2}{\|\mathbf{b}\|_2}$$

*Proof.* We start with the observation that (given that  $A$  is a bounded operator)

$$\|\mathbf{b}\|_2 = \|A\mathbf{x}_e\|_2 \leq \|A\|_2 \|\mathbf{x}_e\|_2$$

By rewriting this inequality we can obtain

$$\frac{1}{\|\mathbf{x}_e\|_2} \leq \|A\|_2 \frac{1}{\|\mathbf{b}\|_2}$$

Now notice that  $A(\mathbf{x} - \mathbf{x}_e) = \mathbf{e}$ , hence  $\mathbf{x} - \mathbf{x}_e = A^\dagger \mathbf{e}$  after applying the pseudo-inverse of  $A$ . Taking norms on both sides leads to

$$\|\mathbf{x} - \mathbf{x}_e\|_2 = \|A^\dagger \mathbf{e}\|_2 \leq \|A^\dagger\|_2 \|\mathbf{e}\|_2$$

as the pseudo-inverse of  $A$  is also bounded. Combining both inequalities leads to

$$\frac{\|\mathbf{x} - \mathbf{x}_e\|_2}{\|\mathbf{x}_e\|_2} \leq \|A\|_2 \|A^\dagger\|_2 \frac{\|\mathbf{e}\|_2}{\|\mathbf{b}\|_2} = \kappa(A) \frac{\|\mathbf{e}\|_2}{\|\mathbf{b}\|_2}$$

□

The above result implies that ill-conditioned matrices  $A$  produce solutions that are very sensitive to (small) perturbations  $\mathbf{e}$ . We expect that in this case the solution  $\mathbf{x}$  may be far away from the exact solution  $\mathbf{x}_e$ . This behavior should be avoided for accurate predictions of the solution. One way of reducing the sensitivity is to add extra information to our inverse problem about the solution we seek. This way we *regularize* the solution as we reduce the “solution space” of our problem, by adding extra constraints.

Another way of regularizing the problem is to consider a better conditioned system

$$A'\mathbf{x} = \mathbf{b} \quad (4.2)$$

that is “near” the original system in the sense that the solutions of (4.2) approximate the solutions of the original system and such that the solution is less sensitive to small perturbations. Such methods are called *regularization methods*. In fact, there is a close relationship between  $A'$  and the pseudo inverse  $A^\dagger$  of matrix  $A$ . Solutions of system 4.2 are approximations of  $\mathbf{x}^\dagger$  and the operator  $(A')^\dagger$  approximates  $A^\dagger$ . A theoretical approach of regularization methods can be found in [7].

## 4.2 Standard Regularization methods

We begin with discussing some standard regularization methods as described in the introduction. The ideas behind these regularization methods can be used later on to describe the regularizing effects of the CGLS method. As we will see, the CGLS method is suitable for the application of regularization.

As always consider the following linear system of equations

$$A\mathbf{x} = \mathbf{b}$$

where  $A$  is a rectangular  $m \times n$  matrix and  $\mathbf{b}$  is polluted by a noisy term

$$\mathbf{b} = \mathbf{b}_e + \mathbf{e}$$

Denote by  $\mathbf{x}_e$  the exact solution of the system  $A\mathbf{x} = \mathbf{b}_e$  and let  $(U, \Sigma, V)$  be a singular system for  $A$ , i.e., we can decompose  $A$  as

$$A = U\Sigma V^T$$

Let  $\sigma_1 \geq \sigma_2 \geq \dots \geq \sigma_r > 0$  denote the singular values of  $A$ ,  $\mathbf{u}_i$  the left-singular vector of  $A$  and  $\mathbf{v}_i$  the right-singular vectors of  $A$ . As described in the previous chapter, we can solve the linear system using the pseudo-inverse of  $A$  to obtain the naive solution

$$\mathbf{x}^\dagger := A^\dagger(\mathbf{b}_e + \mathbf{e}) = \sum_{i=1}^r \frac{\langle \mathbf{b}_e, \mathbf{u}_i \rangle}{\sigma_i} \mathbf{v}_i + \sum_{i=1}^r \frac{\langle \mathbf{e}, \mathbf{u}_i \rangle}{\sigma_i} \mathbf{v}_i \quad (4.3)$$

where  $r = \text{rank}(A)$  is the rank of  $A$ . Note that a solution of the system  $A\mathbf{x} = \mathbf{b}$  drifts away from the exact solution  $\mathbf{x}_e$  in the presence of some noisy term in  $\mathbf{b}$ . This means that if the matrix  $A$  is ill-conditioned we can see that in 4.3 the second summation can become very large due to small singular values. So even if  $\|\mathbf{e}\|_2 \ll \|\mathbf{b}\|_2$ , we can expect that the solution  $\mathbf{x}^\dagger$  is far away from the exact solution  $\mathbf{x}_e$ .

The idea behind some standard regularization methods is to reduce the influence of noise on the best-approximate solution  $\mathbf{x}^\dagger$ . There are two methods that are based on this principle: the truncated SVD regularization and Tikhonov regularization.

### 4.3 Truncated SVD

For this moment we assume that  $\|\mathbf{e}\|_2 \ll \|\mathbf{b}\|_2$  and consider expression 4.3. Furthermore we assume that matrix  $A$  has a large condition number, such that  $A$  has both large and small singular values and that there is a clear distinction between them. Now for large singular values  $\sigma_i$  we assume<sup>1</sup> that

$$\frac{\langle \mathbf{b}, \mathbf{u}_i \rangle}{\sigma_i} \approx \frac{\langle \mathbf{b}_e, \mathbf{u}_i \rangle}{\sigma_i}$$

while for small singular values we assume that

$$\frac{\langle \mathbf{b}, \mathbf{u}_i \rangle}{\sigma_i} \approx \frac{\langle \mathbf{e}, \mathbf{u}_i \rangle}{\sigma_i}$$

Therefore it seems reasonable to only take in account the first few contributions to the solution in 4.3 that contain the most information about the signal that we seek. We simply chop off those SVD components that are dominated by the noise, which are the SVD terms that correspond to small singular values. This leads to the so-called *truncated SVD* (also abbreviated as the TSVD) solution  $\mathbf{x}_k$  as the solution obtained by retaining the first  $k$  components of the naive solution 4.3:

$$\mathbf{x}_k = \sum_{i=1}^k \frac{\langle \mathbf{b}, \mathbf{u}_i \rangle}{\sigma_i} \mathbf{v}_i, \quad \text{for some } k \leq r \quad (4.4)$$

In this expression parameter  $k$  is called the truncation parameter and serves as a so-called *regularization parameter*. The parameter should be chosen in such a way that the noisy terms that are dominating in the naive solution are neglected. The choice of the truncation parameter depends on the specific problem that is considered. In [10, Ch. 5.2 - 5.5] a few parameter choice methods are discussed such as the *discrepancy principle*, the so-called *Generalized Cross Validation* (GCV) method and the choice of the truncation parameter via a so-called NCP analysis (normalized cumulative periodogram).

---

1. We assume that the exact data  $\mathbf{b}_e$  satisfies the *Picard Criterion*, that is, the SVD components decay faster than the singular values. This guarantees that a square-integrable inverse solution exists. See [10, chapter 3] for a detailed explanation on the Picard Criterion. It follows from the Picard Criterion that the two approximations of the SVD components holds.

An alternative formulation of the TSVD can be given in terms of a “near” system of equations of  $A\mathbf{x} = \mathbf{b}$ . Let

$$A = \sum_{i=1}^n \mathbf{u}_i \sigma_i \mathbf{v}_i^T$$

denote the SVD of  $A$ . For some  $k \leq n$  we define the matrix

$$A' := A_k = \sum_{i=1}^k \mathbf{u}_i \sigma_i \mathbf{v}_i^T$$

The condition number of the matrix  $A_k$  is given by  $\kappa(A_k) = \frac{\sigma_1}{\sigma_k}$  and this is smaller than  $\kappa(A)$ , hence the matrix  $A'$  is better conditioned and the system  $A'\mathbf{x} = \mathbf{b}$  is near the original system. Since matrix  $A_k$  is rank deficient for  $k < n$ , there is not a unique solution to the least-squares minimization problem

$$\mathbf{x} = \arg \min \|A_k \mathbf{x} - \mathbf{b}\|_2^2$$

Observe that for  $A_k \mathbf{x} = \mathbf{b}$  the general solution<sup>2</sup> has the form

$$\mathbf{x} = \sum_{i=1}^k \frac{\langle \mathbf{b}, \mathbf{u}_i \rangle}{\sigma_i} \mathbf{v}_i + \sum_{i=k+1}^n \xi_i \mathbf{v}_i, \quad \text{for arbitrary } \xi_i \quad (4.5)$$

To define a unique solution, we have to add additional constraints to the least-squares problem. A natural constraint we already named before is to seek a solution that has a minimum 2-norm. The minimization problem then becomes

$$\min_{\mathbf{x}} \|A_k \mathbf{x} - \mathbf{b}\|_2 \quad \text{subject to} \quad \min \|\mathbf{x}\|_2$$

Looking at the general solution 4.5 we see that the solution of the minimization problem is given in 4.4: simply take all  $\xi_i = 0$ , then the solution  $\mathbf{x}$  has the smallest 2-norm. Therefore we can conclude that the TSVD produces a regularized solution of minimal norm.

#### 4.4 Tikhonov Regularization

Another well known regularization method is the so-called Tikhonov Regularization. Although its name suggests that the method is due to Tikhonov, many mathematicians invented the method in the same period. But as Tikhonov’s work in connection with this method was so important, his name was associated to this method.

Tikhonov regularization is, in some sense, based on the same observation as made in the case of the TSVD. We observed that the noise in the SVD components belonging to the smaller singular values are more dominant in 4.3 and that the SVD components

---

2. Note that  $\mathbf{x} = A_k^\dagger \mathbf{b}$  is a solution of  $A_k \mathbf{x} = \mathbf{b}$ . Write  $A_k = \sum_{i=1}^k \mathbf{u}_i \sigma_i \mathbf{v}_i^T - \sum_{i=k+1}^n \mathbf{u}_i \sigma_i \mathbf{v}_i^T$  and note that the right-singular vectors  $\mathbf{v}_{k+1}, \mathbf{v}_{k+2}, \dots, \mathbf{v}_n$  are elements of the null-space of the matrix  $A_k$ .

of the larger singular values contribute more to the solution. But the contributions of the SVD components of the smaller singular values to the solution should not be fully neglected, as they may contain important information about the solution. Therefore, we want to add small adjustments to the smaller singular values while keeping the larger singular values the same. Before we can observe this behavior of the Tikhonov regularization method, we first define the Tikhonov regularization in a more general setting.

When we solve a discrete inverse problems, we always encounter a system of equations of the form

$$A\mathbf{x} = \mathbf{b}$$

which in general can have no solution. Instead consider the corresponding least-squares minimization problem given by

$$\tilde{\mathbf{x}} = \arg \min_{\mathbf{x}} \|A\mathbf{x} - \mathbf{b}\|_2^2$$

where the term  $r(\mathbf{x}) = \|A\mathbf{x} - \mathbf{b}\|_2^2$  is called the *residual* of  $\mathbf{x}$ . The residual gives an indication of how well the solution  $\mathbf{x}$  fits the data in the system  $A\mathbf{x} = \mathbf{b}$ .

#### 4.4.1 General form

The Tikhonov Regularization problem takes the following general form

$$\mathbf{x}_\lambda = \arg \min_{\mathbf{x}} \|A\mathbf{x} - \mathbf{b}\|_2^2 + \lambda^2 \|L\mathbf{x}\|_2^2 \quad (4.6)$$

where  $L$  is some matrix that consists of a-priori information about the solution(s) of the system of equations  $A\mathbf{x} = \mathbf{b}$ . The regularization parameter  $\lambda$  has a positive value that controls the weighting between the two terms  $\|A\mathbf{x} - \mathbf{b}\|_2^2$  and  $\|L\mathbf{x}\|_2^2$ .

- The first term,  $\|A\mathbf{x} - \mathbf{b}\|_2^2$  models how well the solution  $\mathbf{x}$  fits the data in the presence of some noisy vector  $\mathbf{b}$ . If this term becomes too large, the solution  $\mathbf{x}$  does not solve the problem, and the vector  $\mathbf{x}$  is useless. On the other hand, we do not need the residual to be as small as possible. If the vector  $\mathbf{b}$  contains noise, a very small residual would imply that we also fit the noise in the data perfectly. This kind of fitting should be avoided at all cost, as the solutions obtained then are only locally applicable (the solution  $\mathbf{x}$  would only satisfy data set  $\mathbf{b}$ , and nothing can be said about the solution in a more global setting).
- The second term  $\|L\mathbf{x}\|_2^2$  measures the regularity of the solution. It measures how well the solution  $\mathbf{x}$  satisfies the a priori information described by  $L$ . We hope that we can produce better solutions by adding such information to the problem.

A small value of  $\lambda$  implies that the Tikhonov solution  $\mathbf{x}_\lambda$  has a small residual (so the solution  $\mathbf{x}_\lambda$  satisfies the data well) and that the a priori information in  $L$  is not satisfied (because that term is already small), where a larger value of  $\lambda$  produces a solution that satisfies the a priori information more. A good balance between these two terms

is important to produce good solutions. Therefore, the problem in a Tikhonov regularization reduces to finding the correct value for  $\lambda$  such that the solution  $\mathbf{x}_\lambda$  is the most optimal one, *given some good operator L*.

#### 4.4.2 L-curve method to find $\lambda$

Several techniques are known about finding the best value of  $\lambda$ . One way of finding the optimal  $\lambda$  is via the so-called “L-curve” method. This method is based on an intuitive view of regularization. One can prove that the residual norm

$$\rho(\lambda) = \|A\mathbf{x}_\lambda - \mathbf{b}\|_2^2$$

is monotonically increasing in  $\lambda$  and that the norm of the Tikhonov solution

$$\xi(\lambda) = \|L\mathbf{x}_\lambda\|_2^2$$

is monotonically decreasing in  $\lambda$ . This specific behavior of the residual norm and the norm of the solution implies an “optimal” value  $\lambda$  that is known as the corner of the graph

$$\Gamma(\lambda) = \left( \frac{1}{2} \log_{10} \rho(\lambda), \frac{1}{2} \log_{10} \xi(\lambda) \right)$$

One can prove that graph has a typical *L*-shape. The corner of this *L*-shaped graph is then the point for which the corresponding  $\lambda$  is *presumed* to be as the optimal value of the Tikhonov regularization method. In the corner there is an optimal balance between minimizing the residual norm and minimizing the length of  $L\mathbf{x}$ . In figure 7.7 an example of an *L*-curve is shown.

In [10], section 4.7, and in [11] one can find a detailed explanation about this method and other properties of the L-curve. We omit any further explanation of the L-curve method in this report and refer to [10] and [11].

#### 4.4.3 Writing the minimization in a different form

The Tikhonov problem formulation in 4.6 can be described as a least-squares problem in  $\mathbf{x}$ . This is done by first noting that

$$\left\| \begin{pmatrix} \mathbf{y} \\ \mathbf{z} \end{pmatrix} \right\|_2^2 = \begin{pmatrix} \mathbf{y} \\ \mathbf{z} \end{pmatrix}^T \begin{pmatrix} \mathbf{y} \\ \mathbf{z} \end{pmatrix} = \mathbf{y}^T \mathbf{y} + \mathbf{z}^T \mathbf{z} = \|\mathbf{y}\|_2^2 + \|\mathbf{z}\|_2^2$$

Applying this result to 4.6 leads to the equivalent problem

$$\min_{\mathbf{x}} \left\| \begin{pmatrix} A \\ \lambda L \end{pmatrix} \mathbf{x} - \begin{pmatrix} \mathbf{b} \\ \mathbf{0} \end{pmatrix} \right\|_2^2 \tag{4.7}$$

which is a least-squares problem in  $\mathbf{x}$ . Such a problem can be solved by first considering the corresponding normal equations given by

$$\begin{pmatrix} A \\ \lambda L \end{pmatrix}^T \begin{pmatrix} A \\ \lambda L \end{pmatrix} \mathbf{x} = \begin{pmatrix} A \\ \lambda L \end{pmatrix}^T \begin{pmatrix} \mathbf{b} \\ \mathbf{0} \end{pmatrix}$$

and then use an appropriate solver to find a (least-squares) solution. For numerical algorithms is it sometimes better to base the computation of Tikhonov solutions on 4.7 rather than on the normal equations. In the last part of this chapter, in section 4.7, we consider the CGLS method that is able to solve minimization problems like 4.7.

#### 4.4.4 Tikhonov when $L = I$

An example of the matrix  $L$  is when it equals the identity matrix  $L = I$ . The Tikhonov problem takes the form

$$\mathbf{x}_\lambda = \arg \min_{\mathbf{x}} \|\mathbf{A}\mathbf{x} - \mathbf{b}\|_2^2 + \lambda^2 \|\mathbf{x}\|_2^2$$

which means that we are looking for solutions such that the 2–norm of that solution is minimal. The Tikhonov problem is then solved by finding a least-squares solution of the equation

$$(A^T A + \lambda^2 I)\mathbf{x} = A^T \mathbf{b}$$

which can be solved using the pseudo-inverse of  $A^T A + \lambda^2 I$ :

$$\mathbf{x}_\lambda = (A^T A + \lambda^2 I)^\dagger A^T \mathbf{b}$$

Let  $A = U\Sigma V^T$  be the singular value decomposition of  $A$ . Here, we use the *compact* form of the SVD. This means that we can choose matrices  $U$ ,  $\Sigma$  and  $V$  in such a way that  $\Sigma$  is a diagonal matrix. Using that  $VV^T = I$  we find that

$$\begin{aligned} \mathbf{x}_\lambda &= (V\Sigma^2 V^T + \lambda^2 VV^T)^\dagger V\Sigma U^T \mathbf{b} \\ &= V(\Sigma^2 + \lambda^2 I)^\dagger V^T V\Sigma U^T \mathbf{b} \\ &= V(\Sigma^2 + \lambda^2 I)^\dagger \Sigma U^T \mathbf{b} \\ &= V(\Sigma^2 + \lambda^2 I)^{-1} \Sigma U^T \mathbf{b} \end{aligned}$$

Here, we have used that for an invertible diagonal matrix the pseudo-inverse is equal to the inverse matrix. The above expression for  $\mathbf{x}_\lambda$  can be expressed in terms of singular values and singular vectors. We obtain the following neat expression for  $\mathbf{x}_\lambda$ :

$$\mathbf{x}_\lambda = \sum_{i=1}^n \left( \frac{\sigma_i^2}{\sigma_i^2 + \lambda^2} \right) \frac{\mathbf{u}_i^T \mathbf{b}}{\sigma_i} \mathbf{v}_i \quad (4.8)$$

Observe how the regularization parameter  $\lambda$  influences the regularized solution  $\mathbf{x}_\lambda$ . Define

$$\varphi_i^{[\lambda]} = \frac{\sigma_i^2}{\sigma_i^2 + \lambda^2} \approx \begin{cases} 1 & \sigma_i \gg \lambda \\ \frac{\sigma_i^2}{\lambda^2} & \sigma_i \ll \lambda \end{cases}$$

where  $\varphi_i^{[\lambda]}$  are the so-called *filter factors* (compare with equation 4.4). For singular values that are much larger than  $\lambda$ , the corresponding filter factors are close to 1, so the associated singular value components are not changed a lot, while for singular

values much smaller than  $\lambda$ , the filter factors are proportional to  $\sigma_i^2$ , so the corresponding SVD components are damped.

Compared to the TSVD regularization method, Tikhonov regularization methods seem to be more “fair” towards the SVD components than the TSVD. In the TSVD method we simply cut off all the SVD components that correspond to the small singular values. But we see from the naive solution 4.3 that the SVD components that correspond to the small singular values also contain information about the solution.

Therefore, the TSVD method tends to produce a solution that is oversmoothed. Looking at the filter factors of the Tikhonov solution 4.8, we see that this oversmoothing behavior is less present there because the contribution of SVD components to the solution decreases more gradually. Only for very small  $\sigma_i$  the SVD component is reduced by the filter factor.

#### 4.5 Numerical Solvers: direct methods

Throughout this section we consider methods of solving the linear system

$$A\mathbf{x} = \mathbf{b}, \quad A \in \mathbb{R}^{m \times n}, \quad \mathbf{x} \in \mathbb{R}^n, \quad \mathbf{b} \in \mathbb{R}^m \quad (4.9)$$

Since the linear system is not necessarily square, it may happen that the system has no, one or infinitely many solutions. A linear system is called *underdetermined* if there are more unknowns than equations. A system is called *formally determined* if the number of unknowns equals the number of equations and a system is called *overdetermined* if the number of equations exceeds the number of unknowns.

In the case of a formally determined system, the system has exactly one solution if matrix  $A$  is invertible. In the case of a singular matrix  $A$ , it can still occur that a linear system is consistent, that is, the vector  $\mathbf{b} \in \text{col}(A)$  is a linear combination of the columns of  $A$ .

In the case of an underdetermined system we expect that at least  $n - m$  unknowns cannot be determined (these  $n - m$  unknowns are then called free variables). To be able to “solve” an underdetermined system, additional information is required to pick the “best” solution from all possible solutions. One way of doing this is to search for the *minimum norm solution*

$$\mathbf{x}_{MN} = \arg \min \{ \|\mathbf{x}\|_2 : A\mathbf{x} = \mathbf{b} \}$$

Note that we already have seen this approach in the alternative formulation of the TSVD. In this formulation, picking the minimum-norm solution is a way of picking a regularized solution by adding additional information about the solution.

When the system is overdetermined ( $m > n$ ) we cannot expect that the system 4.9 has a solution. A least-squares solution of the system 4.9 can be found by minimizing

the residual

$$\mathbf{x}_{LS} = \arg \min \|\mathbf{Ax} - \mathbf{b}\|_2^2$$

Depending on the specific problem (equation 4.9) considered, a numerical solver is chosen to solve the problem. A *direct solver* uses a factorization of  $A$  to solve the linear system 4.9 effectively. By a factorization of  $A$ , solving the system reduces to solving smaller linear systems of equations. In most of the time, solving such smaller linear systems is fast and easy. Drawbacks of direct solvers are:

- The matrix  $A$  needs to be explicitly available for factorization of  $A$ ;
- Sufficient memory allocation for matrix  $A$  and its factors;
- Possible numerical instability of direct solvers.

Direct solvers as the LU-decomposition, QR-decomposition and the SVD-factorization are direct solvers that can be used to compute solutions for small systems of equations.

#### 4.5.1 QR-decomposition for least-squares problems

The QR-decomposition can be used to solve underdetermined and overdetermined problems. For **underdetermined** problems 4.9 with  $\text{rank}(A) = m$  we first determine the QR-factorization of  $A^T = QR$ , where  $Q$  is an orthogonal  $n \times n$  matrix and  $R$  is of the form

$$R = \begin{bmatrix} R_1 \\ 0 \end{bmatrix}$$

Here, matrix  $R_1$  is an upper triangular  $m \times m$  matrix. The least-squares solution of the system is formally given by

$$\mathbf{x}_{QR} = Q \begin{bmatrix} (R_1^T)^{-1} \mathbf{b} \\ 0 \end{bmatrix}$$

where  $(R_1^T)^{-1} \mathbf{b}$  is the solution of the system  $R_1^T \mathbf{z} = \mathbf{b}$ . This solution can for example be found by applying a Gaussian elimination.

For **overdetermined** problems one first computes  $A = QR$ . The least-squares solution is then expressed by

$$\mathbf{x}_{QR} = R_1^{-1}(Q_1^T \mathbf{b})$$

where  $Q_1$  is an  $m \times n$  matrix containing the first  $n$  columns of the  $m \times m$  orthogonal matrix  $Q$  and  $n \times n$  matrix  $R_1$  is given as above.

## 4.6 Numerical Solvers: iterative methods

In this section we introduce the notion of Krylov-subspace iterative methods. We first recall the notion of an iterative solver and work towards one specific Krylov-subspace iterative solver: the conjugate gradient least squares method (CGLS). This method can be used to compute least-squares solutions of an underdetermined or overdetermined linear system. Furthermore, the method allows regularization. The method is suggested to work well with Tikhonov regularization. After defining how the CGLS method works, we will discuss regularization in the CGLS method to obtain more feasible results.

Iterative solvers tend to solve the system by starting at some initial guess  $\mathbf{x}_0$  and produce a sequence of vectors  $(\mathbf{x}_k)_{k=0}^{\infty}$  such that each iterate  $\mathbf{x}_k$  is an improved approximation of the exact solution. For iterative methods the matrix  $A$  does not need to be known explicitly, but one needs to be able to compute its product with an arbitrary vector. This makes using iterative solvers attractive when matrix  $A$  is very large or when  $A$  is not known explicitly.

In general we stop iterating when some stopping criterion has been satisfied or if a maximum of iterations has been reached. A typical stopping criterion is constructed by looking at the residual

$$\mathbf{r}_k = \|A\mathbf{x}_k - \mathbf{b}\|_2^2$$

The iterative solver is then stopped when the residual is reduced sufficiently. Basic iterative methods such as the Jacobi Method or the Gauss-Seidel method are based on splitting matrix  $A$  into simpler parts. A direct drawback of such basic iterative methods is that the matrix  $A$  needs to be given explicitly in order to compute the decompositions. Furthermore, basic iterative methods do not converge fast enough for application. Faster iterative methods are therefore needed. A family of such solvers are called the Krylov-subspace iterative methods.

### 4.6.1 Krylov-subspace iterative methods

The fundamentals of Krylov-subspace iterative methods are based on the so-called Cayley-Hamilton theorem. The Cayley-Hamilton theorem states that every  $n \times n$  matrix  $A$  satisfies  $p(A) = \mathbf{0}$ , where

$$p(\lambda) := \det(A - \lambda I_n)$$

is defined as the characteristic polynomial and  $\mathbf{0}$  is the  $n \times n$  zero matrix. As a simple illustration consider the matrix

$$A = \begin{bmatrix} 1 & 2 \\ 3 & 4 \end{bmatrix}$$

The characteristic polynomial is given by

$$p_A(\lambda) = \det(A - \lambda I_n) = \det \begin{pmatrix} 1 - \lambda & 2 \\ 3 & 4 - \lambda \end{pmatrix} = \lambda^2 - 5\lambda - 2$$

Now define  $p(X) = X^2 - 5X - 2I_2$ , then one can simply verify that  $p(A) = \mathbf{0}$ .

A direct result from the Cayley-Hamilton theorem is that for any invertible matrix  $A$ , the matrix satisfies the following identity:

$$p(A) = A^n + c_{n-1}A^{n-1} + \dots + c_1A + (-1)^n \det(A)I_n = \mathbf{0}$$

This leads to the following expression for the inverse  $A^{-1}$ :

$$A^{-1} = \frac{(-1)^{n-1}}{\det A} (A^{n-1} + c_{n-1}A^{n-2} + \dots + c_1I_n)$$

Thus, for any invertible matrix  $A$ , its inverse can be expressed into terms of powers of  $A$  (where  $I_n = A^0$ ), or

$$A^{-1} \in \text{span}(I, A, A^2, \dots, A^{n-1})$$

Consider for now the system  $A\mathbf{x} = \mathbf{b}$  where  $A$  is invertible. Due to the above observations, the Cayley-Hamilton theorem implies that the solution  $\mathbf{x}^* = A^{-1}\mathbf{b}$  can be written as

$$\begin{aligned} \mathbf{x}^* = A^{-1}\mathbf{b} &= \frac{(-1)^{n-1}}{\det A} (A^{n-1} + c_{n-1}A^{n-2} + \dots + c_1I_n)\mathbf{b} \\ &= \frac{(-1)^{n-1}}{\det A} (A^{n-1}\mathbf{b} + c_{n-1}A^{n-2}\mathbf{b} + \dots + c_1\mathbf{b}) \end{aligned}$$

which means that  $\mathbf{x}^* \in \text{span}(\mathbf{b}, A\mathbf{b}, A^2\mathbf{b}, \dots, A^{n-1}\mathbf{b})$ . This is the starting point for Krylov-subspace iterative methods. We define the  $k$ -th Krylov subspace  $\mathcal{K}_k(A, \mathbf{b})$  associated to  $A$  and  $\mathbf{b}$  to be the subspace spanned by the product of the first  $k - 1$  powers of  $A$  and  $\mathbf{b}$ :

$$\mathcal{K}_k(A, \mathbf{b}) = \text{span}(\mathbf{b}, A\mathbf{b}, \dots, A^{k-1}\mathbf{b})$$

Observe that  $\mathbf{x}^* \in \mathcal{K}_n(A, \mathbf{b})$  and for natural numbers  $p \leq q$  that  $\mathcal{K}_p(A, \mathbf{b}) \subseteq \mathcal{K}_q(A, \mathbf{b})$ .

Krylov-subspace iterative methods are iterative methods that seek the  $k$ -th approximation of the solution in the Krylov subspace  $\mathcal{K}_k(A, \mathbf{b})$  of order  $k$ . Because of the nested behavior of the Krylov subspaces each iterate is a better approximation of the solution.

One of the first Krylov-subspace methods is the so-called *Conjugate Gradient Method* (CG method). Originally this method was formulated for symmetric positive definite matrices, but later the method was extended to a larger class of matrices. A nice feature of the CG method is that it only requires one matrix-vector product for each iteration, and the memory allocation is independent of the number of iterations. This makes the method a compact solver to implement. A detailed explanation on this method can be found in [25, Ch. 6].

## 4.7 CGLS method

If the matrix  $A$  is not symmetric positive definite, the Conjugate Gradient Method cannot be applied. An alternative iterative method for non-square matrices is the so-called Conjugate Gradient Method for Least Squares (CGLS). The method is basically the application of the CG method to the normal equations

$$A^T A \mathbf{x} = A^T \mathbf{b}$$

without ever forming the product  $A^T A$ . This is a very nice feature because forming the product  $A^T A$  can be a very expensive operation. We give an explanation of this method.

In the CGLS method, the  $k$ -th CGLS iterate is a solution to the minimization problem

$$\mathbf{x}_k = \arg \min_{\mathbf{x} \in \mathcal{K}_k(A^T A, A^T \mathbf{b})} \|\mathbf{A}\mathbf{x} - \mathbf{b}\|_2^2 \quad (4.10)$$

which we can interpret as the element  $\mathbf{x}_k$  in the Krylov subspace  $\mathcal{K}_k(A^T A, A^T \mathbf{b})$  that minimizes the residual  $r = \|\mathbf{A}\mathbf{x} - \mathbf{b}\|_2^2$  or, equivalently, the vector such that  $\mathbf{A}\mathbf{x}_k$  is closest to  $\mathbf{b}$ . Solving the minimization problem is equivalent to the minimization of the functional

$$\Phi(\mathbf{x}) = \frac{1}{2} \mathbf{x}^T A^T A \mathbf{x} - \mathbf{x}^T A^T \mathbf{b}$$

Indeed, as  $A^T A$  is positive-semidefinite, the surface defined by the quadratic form  $\Phi(\mathbf{x})$  is shaped like a paraboloid bowl, hence  $\Phi(\mathbf{x})$  has a global minimum. Furthermore, the minimum of  $\Phi(\mathbf{x})$  can be found by setting the gradient of  $\Phi(\mathbf{x})$  to zero. This leads to

$$\nabla \Phi(\mathbf{x}) = A^T A \mathbf{x} - A^T \mathbf{b} = \mathbf{0}$$

Hence, any solution of the equation  $\nabla \Phi(\mathbf{x}) = 0$  satisfies the normal equations and thus leads to a solution of minimization problem 4.7.7.

### 4.7.1 Residual error

For the  $k$ -th iterate we define the residual error

$$\mathbf{r}_k = A^T \mathbf{b} - A^T A \mathbf{x}_k$$

which can be interpreted as a measure for the goodness of fit of the  $k$ -th iterate to the data. When the length of the vector  $\mathbf{r}_k$  is small, we expect that the iterate  $\mathbf{x}_k$  is a good least-squares solution.

### 4.7.2 Sequential linear searches

The search for the minimizer is done by performing sequential linear searches along the  $A^T A$ -conjugate directions,

$$\mathbf{p}_0, \mathbf{p}_1, \dots, \mathbf{p}_{k-1},$$

where  $A^T A$ -conjugate means that the vectors  $\mathbf{p}_k$  satisfy the condition

$$\mathbf{p}_j^T A^T A \mathbf{p}_k = 0, \quad j < k$$

or in terms of inner products, that the search directions are  $A^T A$ -orthogonal to each other:

$$\langle \mathbf{p}_j, \mathbf{p}_k \rangle_{A^T A} = \langle A \mathbf{p}_j, A \mathbf{p}_k \rangle = 0, \quad j < k$$

Hence the search directions  $\mathbf{p}_0, \mathbf{p}_1, \dots, \mathbf{p}_{k-1}$  form an orthogonal system in the Krylov subspace  $\mathcal{K}_k(A^T A, A^T \mathbf{b})$  with respect to the inner product  $\langle \cdot, \cdot \rangle_{A^T A}$ .

The iterate  $\mathbf{x}_k$  is determined by updating the previous iterate  $\mathbf{x}_{k-1}$  and using the search direction  $\mathbf{p}_{k-1}$  via the formula

$$\mathbf{x}_k = \mathbf{x}_{k-1} + \alpha_{k-1} \mathbf{p}_{k-1} \quad (4.11)$$

where the coefficient  $\alpha_{k-1}$  solves the minimization problem

$$\alpha_{k-1} = \arg \min_{\alpha \in \mathbb{R}} \Phi(\mathbf{x}_{k-1} + \alpha \mathbf{p}_{k-1})$$

Observe that the above minimization takes place along a one-dimensional hyper-space (a straight line) in  $\mathcal{K}_k(A^T A, A^T \mathbf{b})$ , which makes it easy to solve the minimization problem.

### 4.7.3 The value of stepsize $\alpha_{k-1}$

Next we show that the value of  $\alpha_{k-1}$  is given by

$$\alpha_{k-1} = \frac{\|\mathbf{r}_{k-1}\|_2^2}{\|A \mathbf{p}_{k-1}\|_2^2}$$

The derivation of the value is done in three steps. We start by computing the minimum of the function  $\Phi(\mathbf{x}_{k-1} + \alpha \mathbf{p}_{k-1})$ . This result is formulated in the following lemma.

**Lemma 4.7.1.** *The minimum value of the function  $\alpha \mapsto \Phi(\mathbf{x}_{k-1} + \alpha \mathbf{p}_{k-1})$  is taken at the point*

$$\alpha = \frac{\mathbf{p}_{k-1}^T \mathbf{r}_{k-1}}{\mathbf{p}_{k-1}^T A^T A \mathbf{p}_{k-1}}$$

*Proof.* First we write out the expression  $\Phi(\mathbf{x}_{k-1} + \alpha \mathbf{p}_{k-1})$ :

$$\Phi(\mathbf{x}_{k-1} + \alpha \mathbf{p}_{k-1}) = \frac{1}{2} (\mathbf{x}_{k-1} + \alpha \mathbf{p}_{k-1})^T A^T A (\mathbf{x}_{k-1} + \alpha \mathbf{p}_{k-1}) - (\mathbf{x}_{k-1} + \alpha \mathbf{p}_{k-1})^T A^T \mathbf{b}$$

Now compute  $\frac{\partial \Phi}{\partial \alpha}(\mathbf{x}_{k-1} + \alpha \mathbf{p}_{k-1})$  with respect to the variable  $\alpha$ . This leads to

$$\frac{\partial \Phi}{\partial \alpha}(\mathbf{x}_{k-1} + \alpha \mathbf{p}_{k-1}) = \mathbf{p}_{k-1}^T A^T A (\mathbf{x}_{k-1} + \alpha \mathbf{p}_{k-1}) - \mathbf{p}_{k-1}^T A^T \mathbf{b}$$

Solving  $\frac{\partial \Phi}{\partial \alpha} = 0$  for  $\alpha$  gives us:

$$\alpha = \frac{\mathbf{p}_{k-1}^T A^T (\mathbf{b} - A \mathbf{x}_{k-1})}{\mathbf{p}_{k-1}^T A^T A \mathbf{p}_{k-1}} = \frac{\mathbf{p}_{k-1}^T \mathbf{r}_{k-1}}{\mathbf{p}_{k-1}^T A^T A \mathbf{p}_{k-1}}$$

□

#### 4.7.4 New search direction $\mathbf{p}_k$

The construction of the new search direction  $\mathbf{p}_k$  from the previous search direction  $\mathbf{p}_{k-1}$  is given by

$$\mathbf{p}_k = \mathbf{r}_k + \beta_k \mathbf{p}_{k-1} \quad (4.12)$$

where  $\beta_k$  is chosen such that  $\mathbf{p}_k$  is  $A^T A$ -conjugate to the previous search directions. Lastly define

$$\mathbf{d}_k = \mathbf{b} - A\mathbf{x}_k \quad (4.13)$$

as the discrepancy associated with  $\mathbf{x}_k$ . Note that the residual of the normal equations and the discrepancy are related to each other via

$$\mathbf{r}_k = A^T \mathbf{d}_k \quad (4.14)$$

#### 4.7.5 Simplification of the expression for $\alpha$

We have found the value of  $\alpha$  that minimizes the functional described above. However, One can show further simplification of the expression for  $\alpha$ . The next step is the following observation about the orthogonality between the search directions and the residual errors

**Lemma 4.7.2.** *For all  $k \in \mathbb{N}$  we have that*

$$\mathbf{p}_{k-1} \perp \mathbf{r}_k$$

*Proof.* We start with the observation that  $\mathbf{r}_k$  can be defined recursively:

$$\mathbf{r}_k = \mathbf{r}_{k-1} - \alpha_{k-1} A^T A \mathbf{p}_{k-1}$$

Using the expression found for  $\alpha$  leads to

$$\begin{aligned} \mathbf{p}_{k-1}^T \mathbf{r}_k &= \mathbf{p}_{k-1}^T \mathbf{r}_{k-1} - \frac{\mathbf{p}_{k-1}^T \mathbf{r}_{k-1}}{\mathbf{p}_{k-1}^T A^T A \mathbf{p}_{k-1}} \mathbf{p}_{k-1}^T A^T A \mathbf{p}_{k-1} \\ &= \mathbf{p}_{k-1}^T \mathbf{r}_{k-1} - \mathbf{p}_{k-1}^T \mathbf{r}_{k-1} \\ &= 0 \end{aligned}$$

Hence  $\mathbf{p}_{k-1}^T$  and  $\mathbf{r}_k$  are orthogonal. □

A direct result of this is the following lemma.

**Lemma 4.7.3.** *For all  $k \in \mathbb{N}$  we have*

$$\mathbf{p}_k^T \mathbf{r}_k = \mathbf{r}_k^T \mathbf{r}_k$$

*Proof.* From the recursive definition of  $\mathbf{p}_k$  and the previous lemma it follows that

$$\mathbf{p}_k^T \mathbf{r}_k = (\mathbf{r}_k^T + \beta_k \mathbf{p}_{k-1}^T)^T \mathbf{r}_k = \mathbf{r}_k^T \mathbf{r}_k + \beta \mathbf{p}_{k-1}^T \mathbf{r}_k = \mathbf{r}_k^T \mathbf{r}_k$$

□

From the previous lemma it follows that the expression for  $\alpha$  can be simplified to

$$\alpha_{k-1} = \frac{\|\mathbf{r}_{k-1}\|_2^2}{\|A\mathbf{p}_k\|_2^2}$$

#### 4.7.6 The value of $\beta_k$

We claim that the value of  $\beta_k$  in equation 4.12 is given by

$$\beta_k = \frac{\|\mathbf{r}_k\|_2^2}{\|\mathbf{r}_{k-1}\|_2^2}$$

The derivation of this expression is analogously to the derivation of  $\alpha$ . We need two lemmas that we give without proof.

**Lemma 4.7.4.** For all  $k \in \mathbb{N}$  we have  $\mathbf{p}_k^T A^T A \mathbf{p}_k = \mathbf{p}_k^T A^T A \mathbf{r}_k$ .

**Lemma 4.7.5.** For all  $k \in \mathbb{N}$  we have  $\mathbf{r}_k \perp \mathbf{r}_{k+1}$ .

We now have enough tools to determine the value of  $\beta_k$ .

**Lemma 4.7.6.** The value of  $\beta_k$  is given by

$$\beta_k = \frac{\|\mathbf{r}_k\|_2^2}{\|\mathbf{r}_{k-1}\|_2^2}$$

*Proof.* From the recursive definition of  $\mathbf{p}_{k+1}$  we find that

$$\mathbf{p}_{k-1}^T A^T A \mathbf{p}_k = \mathbf{p}_{k-1}^T A^T A \mathbf{r}_k + \beta_k \mathbf{p}_{k-1}^T A^T A \mathbf{p}_{k-1}$$

The above should be equal to zero due to the definition of the search directions, hence

$$\beta_k = -\frac{\mathbf{p}_{k-1}^T A^T A \mathbf{r}_k}{\mathbf{p}_{k-1}^T A^T A \mathbf{p}_{k-1}} \quad (4.15)$$

Observe that  $\mathbf{d}_k$  can be defined recursively by

$$\mathbf{d}_k = \mathbf{d}_{k-1} - \alpha_{k-1} A \mathbf{p}_{k-1}$$

Hence this can be rewritten as

$$A \mathbf{p}_{k-1} = \frac{\mathbf{d}_{k-1} - \mathbf{d}_k}{\alpha_{k-1}} \quad (4.16)$$

Using equations 4.14, 4.15 and 4.16 and lemma 4.7.5, the value  $\beta_k$  can now be rewritten as:

$$\begin{aligned} \beta_k &= -\frac{\mathbf{p}_{k-1}^T A^T A \mathbf{r}_k}{\mathbf{p}_{k-1}^T A^T A \mathbf{p}_{k-1}} \\ &= \frac{(\mathbf{d}_k - \mathbf{d}_{k-1})^T A \mathbf{r}_k}{\mathbf{p}_{k-1}^T A^T A \mathbf{p}_{k-1}} \frac{\mathbf{p}_{k-1}^T A^T A \mathbf{p}_{k-1}}{\|\mathbf{r}_{k-1}\|^2} \\ &= \frac{(\mathbf{r}_k - \mathbf{r}_{k-1})^T \mathbf{r}_k}{\mathbf{p}_{k-1}^T A^T A \mathbf{p}_{k-1}} \frac{\mathbf{p}_{k-1}^T A^T A \mathbf{p}_{k-1}}{\|\mathbf{r}_{k-1}\|^2} \\ &= \frac{(\mathbf{r}_k - \mathbf{r}_{k-1})^T \mathbf{r}_k}{\|\mathbf{r}_{k-1}\|^2} \\ &= \frac{\|\mathbf{r}_k\|^2}{\|\mathbf{r}_{k-1}\|^2} \end{aligned}$$

□

#### 4.7.7 Properties of $\mathbf{x}_k$ and $\mathbf{d}_k$

Recall that each iterate in the CGLS method solves the minimization problem and that  $\mathcal{K}_k(A^T A, \mathbf{b}) \subseteq \mathcal{K}_{k+1}(A^T A, \mathbf{b})$ . This implies that the discrepancies  $\mathbf{d}_k$  form a non-increasing sequence

$$\|\mathbf{d}_{k+1}\| \leq \|\mathbf{d}_k\|$$

as we minimize the functional in 4.7.7 over a “larger” space.

With some extra effort (using the orthogonality properties of the search directions), the norms of the solutions form a non-decreasing sequence:

$$\|\mathbf{x}_{k+1}\| \geq \|\mathbf{x}_k\|$$

A proof of this property is found in [12, Section 4].

#### 4.7.8 The CGLS method algorithm

The CGLS method algorithm is summarized as follows. For simplicity we set the initial guess  $\mathbf{x}_0 = \mathbf{0}$ . The algorithm does not contain a stopping criterion, though it is easy to built in such a criterion in the algorithm.

---

**Algorithm 1** The CGLS Algorithm: given the right hand side  $\mathbf{b}$  and matrix  $A$

---

**Initialize:**

$$\begin{aligned}\mathbf{x}_0 &= \mathbf{0}; \\ \mathbf{d}_0 &= \mathbf{b} - A\mathbf{x}_0; \\ \mathbf{r}_0 &= A^T \mathbf{d}_0; \\ \mathbf{p}_0 &= \mathbf{r}_0; \\ \mathbf{y}_0 &= A\mathbf{p}_0;\end{aligned}$$

**for**  $k = 1, 2, \dots$  until stopping criterion is satisfied

$$\begin{aligned}\alpha &= \frac{\|\mathbf{r}_{k-1}\|_2^2}{\|\mathbf{y}_{k-1}\|_2^2}; \\ \mathbf{x}_k &= \mathbf{x}_{k-1} + \alpha \mathbf{p}_{k-1}; \\ \mathbf{d}_k &= \mathbf{d}_{k-1} - \alpha \mathbf{y}_{k-1}; \\ \mathbf{r}_k &= A^T \mathbf{d}_k; \\ \beta &= \frac{\|\mathbf{r}_k\|_2^2}{\|\mathbf{r}_{k-1}\|_2^2}; \\ \mathbf{p}_k &= \mathbf{r}_k + \beta \mathbf{p}_{k-1}; \\ \mathbf{y}_k &= A\mathbf{p}_k;\end{aligned}$$

**end**

---

## 4.8 Regularization properties of the CGLS method

Facing ill-posed linear inverse problems of the form

$$Ax = \mathbf{b} + \mathbf{e}$$

we know that the matrix  $A$  is ill-conditioned. This means that the condition number of  $A$  is large. (In general, condition numbers of the order of  $10^5$  start becoming of concern.) This is caused by the tiny singular values of matrix  $A$ .

When using iterative methods for solving such ill-conditioned linear systems, a semi-convergence behavior can often be observed. Semi-convergence means that at first the iterates tend to converge to some meaningful solution, but as the iterations proceed, they begin to diverge. The divergence can be explained by the noisy term in the right-hand side of the linear system in combination with the singular values of  $A$ . At some point in the iteration the noise becomes more and more amplified and the iterates start to diverge from the (least-squares) solution of the system.

The amplification is due to the growing Krylov subspaces. In [10, Ch 6.3.3] Hansen explains that when we use the CGLS method, after each iteration the Krylov subspaces becomes larger as we are searching for a solution in more search directions. For the first iterations the CGLS method aims at reducing the discrepancy

$$\mathbf{d}_k = \mathbf{b} - A\mathbf{x}_k$$

in the singular direction associated with the larger singular values. On later iterations the discrepancy is reduced in the singular directions that are associated with the smaller singular values. The small singular values begin to spoil the iterates. Hence we conclude that the CGLS method starts with focusing on the most significant components of the SVD expression (the components that contain the most information about the solution that we seek). In [2], Example 4.6, this behavior is also illustrated.

Therefore, we need to capture the solution in time, before the amplified noise takes over. This can be done by truncating the iteration in time before the semi-convergence behavior kicks in. By equipping the iterative method with a stopping rule effective at filtering the amplified noise from the computed solution, we can make the problem less sensitive to perturbations in the data. This process of regularizing by a stopping rule is called *regularization by truncated iteration*. The idea behind regularization by truncated iteration is similar to the truncated SVD expression. When we apply the truncated SVD method, we also try to separate the noise from the solution by truncating the SVD expression, taking only in account the most significant components. More details on the regularizing effects of the CGLS method can be found in an article by A. van der Sluis and H.A. van der Horst [23, Section 6].

When the iterative method stops too early, the solution becomes oversmoothed by the iterative method, while the solution becomes undersmoothed if the iterative method

does not stop in time. Recall that

$$\|\mathbf{d}_{k+1}\| \leq \|\mathbf{d}_k\|, \quad \|\mathbf{x}_{k+1}\| \geq \|\mathbf{x}_k\|$$

where  $\mathbf{d}_k$  is the discrepancy of the  $k$ -th iterate. A solution of the system

$$A\mathbf{x} = \mathbf{b}$$

solved by the CGLS method should be a good fit of the data, while  $\|\mathbf{x}\|$  should not be large. The above observation suggests that there is an iterate  $k$  for which the balance between a good fit of the data and the length of the solution vector is optimal. This observation leads to the so-called  $L$ -curve for the CGLS method. An example of such a typical  $L$ -curve that we encounter in our inverse problem is shown in figure 4.1. We omit the explanation of this method and refer to [19]. As discussed in the  $L$ -curve method for Tikhonov regularization, the optimal point on the  $L$ -curve of the CGLS method is the corner with the largest curvature of the graph described by

$$\Gamma = (\log_{10} \|\mathbf{d}_k\|^2, \log_{10} \|\mathbf{x}_k\|^2), \quad \text{where } k = 1, 2, \dots$$

We will use this criterion when solving our inverse problem with the CGLS method to find the best approximation to the linear inverse problem.

We want to emphasize that this criterion is not a stopping criterion. In order to have a clear view on the shape of the graph  $\Gamma$ , we need to do a large number of iterations to construct  $\Gamma$ . Therefore, this approach does not really seem to be a time efficient one, but we believe that the solutions found via the  $L$ -curve criterion lead to the best approximations. This idea is tested in Chapter 6.

Lcurve and optimal k = 1519

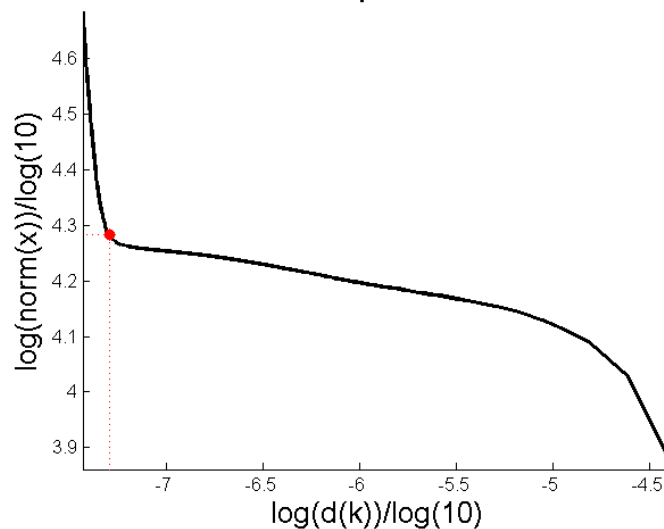


Figure 4.1: Typical  $L$ -curve that we encounter in our discrete inverse problem.



## 5 Application/Test case

In this chapter we discuss the case (the mock-up) and the software programs that we have used during the research project. As a geometry we look at a mock-up model that serves as an input for the Inverse Model. In the first section, we give an outline on the properties and dimensions of the mock-up and the simplifications we have done in the corresponding CAD-model. Then, we discuss the meshing of the mock-up that is done in `COMSOL`, which is a multiphysics Finite Element program that can be used to compute magnetic field surrounding the mock-up. In section 5.2, we give a brief introduction to `COMSOL` and lastly we discuss the ideas behind the simulations in `COMSOL` of magnetic fields.

### 5.1 Mock-up

In order to validate the mathematical physical model, we test the model on a small scaled mock-up of a ship. The mock-up is approximately 5 meters long, 2 meters wide and 1 meter high. The mock-up model is called the **M4** which stands for the “Mock-up for Magnetic Monitoring Measurements”. A *CAD-model* of this mock-up is created in the modeling tool `Rhino` Version 5.0. This 3-D modeling tool is used by designers for the creation of very complex objects. From jewelry to complete ships, the program is user friendly and can be used in combination with various other programs. In figure 5.1 an example<sup>1</sup> of a model created `Rhino` is showed.



Figure 5.1: An example of a model created in `Rhino`

1. <http://www.rhino3d.com/gallery/>

A development of the mock-up can be found in appendix F. The model consists of 9 two-dimensional welded polygons that are welded to a plate that represents the typical upside of a boat. By defining the positions of the corners of the mock-up the polygons are easily defined in *Rhino3d*.

After the creation of the CAD-model in *Rhino3d* it is exported to *COMSOL* to do simulations of the magnetic signature of the **M4**.

### 5.1.1 Real version of the M4

A similar real mock-up is built by the Marinebedrijf in Den Helder to realize a measurement campaign at the item range “Grosse Eva” in Borgstedt, Germany. In figure 5.2 a picture of the **M4** is shown. The mock-up is coated to protect the steel against corrosion.



Figure 5.2: The mock-up **M4**, located at TNO before it was transported to the measurement facility “Grosse Eva”.

### 5.1.2 Simplifications in the CAD-model

A few simplifications in the CAD-model are made with respect to the real version of the mock-up in order to reduce the complexity of the problem.

First we neglect the contributions of weldings to the magnetic properties of the mock-up. As the real mock-up is built by welding several parts together, the weldings may have effect on the magnetic properties of the ship’s steel construction. But as we are only interested in *some* source distribution in the steel, we neglect these weldings.

There are some hoisting eyes welded to the mock-up for transport and furthermore there is a small hole made in the back of the ship so that any water inside the mock-up can be removed easily. These hoisting eyes and the small hole are not present in the CAD-model.

Finally, it appears that the real mock-up consists of steel plates that are slightly bent. The stress on the steel due to the bending affects the hysteresis curve of the steel. However, in the CAD-model we assume that the steel plates are flat plates, and therefore we accept a small error in the geometry of the **M4**.

### 5.1.3 Properties of the steel used

The steel plates used for the construction of the mock-up consist of standard ship steel 52. This special kind of steel is used in the construction of naval ships, excluding submarines, mine hunters and mine sweepers. The hull of mine hunters and mine sweepers of the Royal Netherlands Navy are made of glass-reinforced polyester and the superstructure of these ships are of aluminum. The reason for this is that most influence mines are triggered by disturbances in the magnetic field and this type of construction reduces such disturbances.

### 5.1.4 Meshing of the mock-up

The Petrov Galerkin Method (see section 2.4) is a Finite Element Method (FEM) based on discretisation of an object  $\Omega$  into internal and boundary elements. As explained earlier, this method is used to reduce the inverse problem to a finite-dimensional linear inverse problem that can be solved by means of (iterative) solvers.

The multiphysics software program `COMSOL` contains a mesh-generating algorithm that can define partitions of a given object. In our case, the CAD-model of **M4** is imported into `COMSOL`. The mesh-generating algorithm is used to mesh the **M4**. As very fine partitions often lead to a severe under-determined linear system, we have to choose the discretisation in such a way that we avoid many unknowns in the linear problem, while keeping enough unknowns in order to approximate the solution well enough. An example of a discretisation of the mock-up can be found in figure ??.

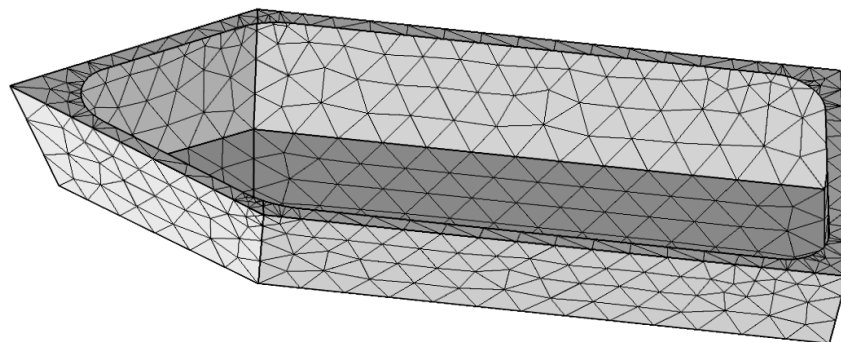


Figure 5.3: Example of the meshing of the mock-up.

## 5.2 Introduction to COMSOL

The Multiphysics program `COMSOL` is a great software package that can simulate different physical phenomena at the same time. `COMSOL` enables the calculation of multiple coupled physical phenomena including either interactions and interconnections. It gives engineers and designers more insight in the physics so they can design better products. Fluid flows and heat flows can be considered simultaneously to see how heat diverges in air, for example. The extensive GUI can be used to create great plots and to export simulation results out of `COMSOL`.

A sophisticated mesh generator makes it possible to compute solutions of mathematical-physical models by the so-called *Finite Element Method*. The mesh generator is able to define a triangulation of an object in terms of mesh points, triangular internal elements, line boundary elements and hexagonal volume elements. Furthermore, advanced numerical methods such as the *Conjugate Gradient Method* and *Preconditioning* are implemented in order to create numerically stable solutions.

Note that, although these methods converge in most of the time, we should always be careful with the solutions produced. Such solutions are not always the correct ones and furthermore the mesh generator sometimes defines a mesh which is not feasible at all. Too large or too tiny elements can lead to unstable solutions. If one suspects this behavior, one should apply enhanced numerical methods and pre-conditioners to achieve stable solutions. These options are built into `COMSOL`.

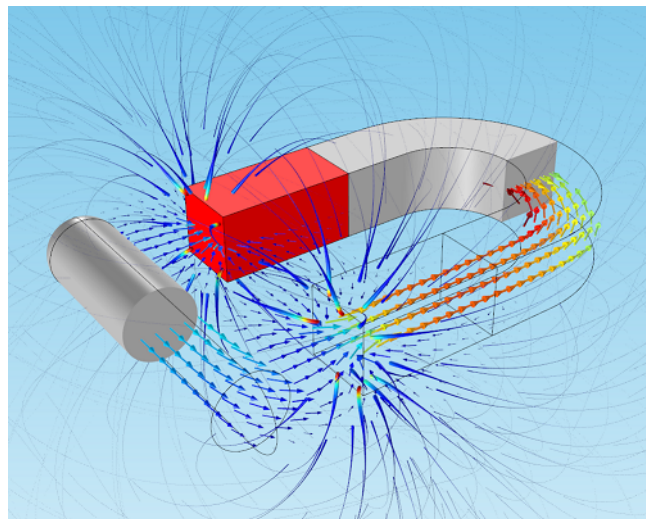


Figure 5.4: Example of the magnetic behavior of two magnets. In this picture, `COMSOL` shows the computed magnetization inside each magnet and the magnetic induction field that surrounds the magnets. source: <http://www.comsol.com>

### 5.2.1 Computation of the (reduced) magnetic field and magnetic shielding

Recall for a moment the *domain equations* that describe the interaction between the magnetization of an object  $\Omega$  and its induced magnetic field (as discussed in Chapter 2.1). First of all, we assume that in a current-free space (so  $\mathbf{J} = \mathbf{0}$ ) the magnetic fields  $\mathbf{H}$  are curl-free:

$$\nabla \times \mathbf{H} = \mathbf{0}$$

This guarantees the existence of some potential  $V_m$  that generates the magnetic field

$$\mathbf{H} = -\nabla V_m$$

Furthermore, due to Maxwell's equations, a magnetic induction field is divergence-free:

$$\nabla \cdot \mathbf{B} = 0$$

The constitutive relation between the magnetic flux density and the magnetic field that leads to the coupled behavior of the fields  $\mathbf{B}$ ,  $\mathbf{H}$  and the magnetization  $\mathbf{M}$  of the object  $\Omega$  is given by

$$\mathbf{B} = \mu_0(\mathbf{M} + \mathbf{H})$$

With these relations an equation for  $V_m$  can be found and is given by

$$-\nabla \cdot (\mu_0 \nabla V_m - \mu_0 \mathbf{M}) = 0$$

In COMSOL, we can choose to solve the above domain equations for the *full field*, that is the sum of all fields that are present, or for the so-called *reduced field*, where we solve the equations for a potential  $V_m$  that corresponds to the induced magnetic induction field  $\mathbf{B}_{red}$  by some magnetization of  $\Omega$ . The potential  $V_m$  is computed in some *space of computation*  $\mathbb{S}$ . In COMSOL we choose this to be a large bounding box that surrounds  $\Omega$ . It is important to note that the boundary of the bounding box should be far away from  $\Omega$ . This becomes clear when we talk about the boundary conditions that we have to add to the problem.

In our work we want to compute the reduced field that is induced by some present background field  $\mathbf{B}_b$ . This means that we are looking for some potential  $V_m$  that generates the reduced magnetic field  $\mathbf{H}_{red}$  where

$$\mathbf{H}_{red} = -\nabla V_m$$

In the simulations we assume that any permanent magnetization is absent, so we only model the interaction between ferromagnetic material and a background field.

In order to make the solution of this PDE unique *boundary conditions* are required. In COMSOL, the following boundary conditions are assumed. Firstly, the **continuity condition** is implemented that guarantees the continuity of the normal component of the magnetic flux density  $\mathbf{B}$ . This is given by

$$\mathbf{n}_2 \cdot (\mathbf{B}_1 - \mathbf{B}_2) = 0$$

between two domains 1 and 2, where  $\mathbf{n}_2$  is the normal vector on domain 2 that is pointing outwards.

Given an magnetization  $\mathbf{M}$  of the ferromagnetic object  $\Omega$ , it is easy to compute the magnetic field with COMSOL by a so-called finite-element package that is built into COMSOL. The *Galerkin weighted residual method* is implemented in COMSOL and can be used to transform the system of PDE (domain equations plus boundary conditions) into a large system of linear equations. The idea behind this method is to expand the potential on a meshed object:

$$V_m = \sum_{i=1}^n W_i V_i$$

where  $W_i$  are so-called predefined weight functions. See for an explanation on this approach [3].

It is also possible in COMSOL to compute reduced magnetic fields that are induced by some present background field. This can be done by solving the problem with a finite-element method. Again, the system of PDE is transformed into a large system of linear equations but due to the complexity of this linear system, all kinds of difficulties such as numerical stability and the lack of memory in the solver are introduced. Therefore extra assumptions are required to reduce the complexity of the problem. A well known method implemented in COMSOL is the so-called *magnetic shielding condition*.

Especially for geometries consisting of thin steel plates, the magnetic shielding method is a way of adding extra boundary conditions to the problem in order to reduce the three-dimensional object to a two-dimensional surface. This is based on the following two assumptions. The first assumption is that the thickness of the steel plates is very small and (for the sake of simplicity) the thickness is constant over the plate. Furthermore, we assume that the magnetization is tangential to the plate, so that everything “happens” along the surface of a plate. This means that when we decompose the magnetization  $\mathbf{M}$  into a tangential component  $\mathbf{M}^{\parallel}$  (along the surface) and a component  $\mathbf{M}^{\perp}$  perpendicular to the surface, we have that  $\mathbf{M}^{\perp} \equiv \mathbf{0}$ .

In [3] and [17] a derivation can be found of the magnetic shielding conditions. The magnetic shielding conditions are given by

$$\mathbf{n} \cdot (\mathbf{B}_1 - \mathbf{B}_2) = -\nabla_t \cdot (\mu_0 \mu_r t \nabla_t V_m), \quad \text{over the surface } \partial\Omega$$

Here,  $\mu_r$  is the relative magnetic permeability of the medium and  $t$  is the plate thickness. The operator  $\nabla_t$  represents a tangential gradient along the surface. After applying the Galerkin weighted residual method these conditions transform into linear equations.

It remains to define proper boundary conditions on the boundary  $\partial\mathcal{S}$  of the computation space. These conditions are required in order to have a unique solution and to

simplify calculations when applying the Galerkin weighted residual method. The first boundary condition is given by the expression

$$-\mathbf{n} \cdot \mathbf{B}_{red} = 0, \quad \text{on } \partial\mathbb{S}$$

and means that the reduced magnetic induction field is insulated inside the computation space  $\mathbb{S}$ . We immediately observe that this is a significant assumption of the behavior of the magnetic induction field. In reality, the magnetic field is defined for each point  $\mathbf{r} \in \mathbb{R}^3$  and the magnetic field is weaker as the distance between the object and an observation point  $\mathbf{r}$  becomes larger. An induced magnetic field is never isolated in some region  $\mathbb{S}$ . But for a large  $\mathbb{S}$ , the error this condition makes becomes smaller.

After adding the boundary conditions discussed to the mathematical model in COMSOL a FEM can be applied to solve the problem for the potential  $V_m$ . By interpolations, the potential  $V_m$  is approximated in the whole space  $\mathbb{S}$ . This allows us to compute the magnetic field via  $\mathbf{H} = -\nabla V_m$ . By this method COMSOL computes the reduced magnetic induction field, induced by the background field  $\mathbf{B}_b$  present.



## 6 Validation and analysis of the prediction model

As we have seen in Chapter 5, the multiphysics program `COMSOL` can be used to calculate the magnetic signature of the **M4** that is placed in some background field  $B_b$ . Note that the magnetic signature, simulated in `COMSOL`, does not contain contributions due to any *permanent magnetization* of the **M4**. The absence of permanent magnetization may simplify the complexity of the signature of the **M4** and therefore makes it easier to predict the magnetic signature.

In this chapter we execute the so-called “Comsol, Inverse, Forward and Validation” routine to investigate the validity of both the inverse formulation and the prediction model. We abbreviate this by a **CIFV** routine. Using the simulations of the magnetic signature in `COMSOL`, we investigate the validity of the prediction model.

This chapter is organized as follows. After an explanation of the **CIFV** process we investigate performance and behavior of the prediction model by considering the following topics:

- **SVD analysis:** looking at the SVD decomposition of the linear inverse system, what can we conclude about the behavior of the system?
- **Solver:** does the choice of a solver (that solves the inverse problem) affect the performance of the prediction model?
- **Double layer potential:** in the inverse formulation the magnetic field is described by three components. Can we neglect the last term in the formulation that describes the normal component of the magnetic field (“double layer component”)?
- **Noise:** The influence of noise in the measurement data on the solutions of the inverse problem.

## 6.1 Introduction to the CIFV process

A flow chart of a **CIFV** routine can be found in figure 6.1. We discuss the steps that are taken in this routine.

In *Rhinoceros* we have created a CAD-file of the **M4**. We modeled the **M4** as a two-dimensional surface with one-dimensional boundaries. This allows us to use the magnetic shielding conditions in *COMSOL* to simulate a magnetic signature of the **M4**, given some background field. The model is processed and exported as a CAD-file into *COMSOL*.

In *COMSOL* we simulate a static background field. We mesh the model using the mesh generator and compute the induced magnetic field surrounding the mock-up. Observe that for accurate simulations of the magnetic signature in *COMSOL*, we need a very fine mesh. The computed reduced magnetic field serves as input for the prediction model, as well as validation for the performance of the prediction model.

Each simulation in *COMSOL* gives rise to a magnetic signature of the mock-up. From this simulation we can define two sets of data. The first data set is a set of values of the magnetic signature at one meter below the **M4** and the second set consists of the values of the magnetic field “on-board” of the **M4**. The first set is used to investigate the validity of the inverse problem, while the values of the second set can be interpreted as the measurements at predefined sensor positions. The second set is therefore used as input for the inverse problem.

Next, the magnetic signature inside the **M4** and one meter below the mock-up is computed and exported as two data sets into *MATLAB*. The inverse problem is executed and magnetic sources  $f, g$  and  $h$  are obtained. These magnetic sources are used to predict the magnetic signature.

The predicted magnetic signature, at one meter below the mock-up, is then compared to the magnetic signature from *COMSOL*.

### 6.1.1 Relative and absolute errors

The investigation of the inverse formulation is done by looking at the relative error

$$\tau(\mathbf{r}) = \frac{\|\mathbf{B}_{predicted}(\mathbf{r}) - \mathbf{B}_{comsol}(\mathbf{r})\|_2}{\|\mathbf{B}_{comsol}(\mathbf{r})\|_2}$$

between the magnetic signature predicted via solving the inverse problem and the magnetic signature simulated in *COMSOL*. Furthermore we look at the absolute error defined by

$$\varepsilon(\mathbf{r}) = \|\mathbf{B}_{predicted}(\mathbf{r}) - \mathbf{B}_{comsol}(\mathbf{r})\|_2$$

and the numbers  $\varepsilon_{max}$ ,  $\tau_{min}$  and  $\tau_{max}$ .

As explained in the introduction of this report, the relative error can be used as a tool to investigate the validity of the model. We call a performance of the prediction model

good if the relative error  $\tau$  is small (which means that there is a good fit between the predicted magnetic signature and the magnetic signature from COMSOL) and that the absolute errors made by the prediction are low, so  $\varepsilon_{max}$  should be low.

### 6.1.2 Meshing

In the validation of the prediction model we look at six different meshes of the mock-up model, from coarse meshes to (very) fine meshes. As the dimension of the mesh influences the number of unknowns in the inverse formulation, it is interesting to investigate in which way the meshing of the mock-up influences the performance of the prediction model. In table 6.1 the dimensions of six meshes are shown, mesh I corresponds to figure 5.3.

|        |     | $ P $ | $ E $ | $ BE $ | unknowns |
|--------|-----|-------|-------|--------|----------|
| Meshes | I   | 527   | 943   | 269    | 1312     |
|        | II  | 394   | 677   | 246    | 1023     |
|        | III | 364   | 617   | 243    | 960      |
|        | IV  | 328   | 545   | 234    | 879      |
|        | V   | 313   | 515   | 233    | 848      |
|        | VI  | 2322  | 4404  | 710    | 5343     |

Table 6.1: Dimensions of the different meshes used in the **CIFV** routines. Here  $|P|$  denotes the number of mesh points,  $|E|$  denotes the number of triangular elements and  $|BE|$  denotes the number of boundary elements. The last column contains the number of unknowns in the inverse problem; the length of vector  $\mathbf{p}$  in equation 2.8 in section 2.4.1.

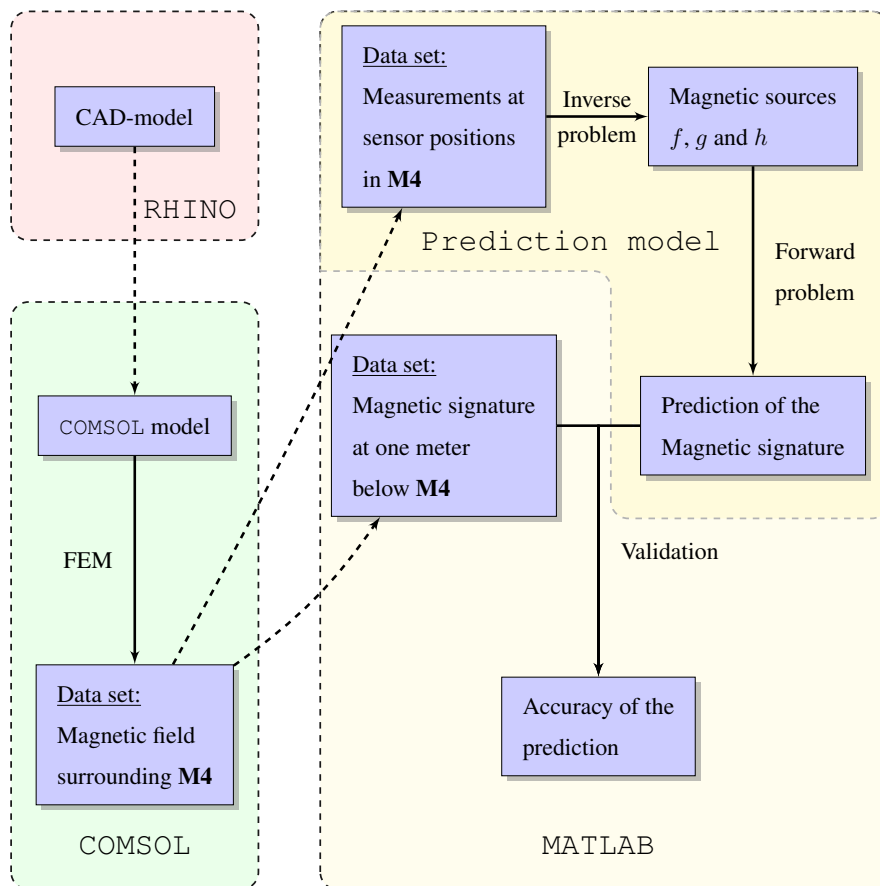


Figure 6.1: Flow chart of the CIFV routine.

## 6.2 Simulation: uniform background field along the $u_x$ -direction

Let  $B_b$  be the static uniform back ground field given by

$$B_b = 50 \cdot 10^{-6} u_x \text{ [T]} \quad (6.1)$$

We compute the magnetic signature of the **M4** in COMSOL. We construct a data set of the magnetic signature that consists of 176 possible sensor positions on-board of the **M4** and construct a data set of the magnetic signature that consists of values at one meter below the **M4** in an array of reference points. The results (the two data sets) are then exported as plain text files and are converted into matrices in MATLAB.

In Appendix A the results of these **CIFV** routines can be found. The results based on 176 measurements inside the **M4** for four different methods and several meshes of the **M4**. In the second table the results are of the use of Tikhonov regularization in the SVD method. The regularization parameter is chosen with the “L-curve” principle. Furthermore we investigated the stability of the usage of a *QR* decomposition. The iterative CGLS method is applied to the system with a total of 528 iterations (the rank of *A*). Due to bad results we have skipped some of the computations of the SVD and QR method.

### 6.2.1 Results of CIFV routines

This section presents some results of the application of the prediction model to the COMSOL input. We consider the magnetic signature of the **M4** in a local background field described in equation 6.1. Therefore, we expect that the induced magnetisation of the **M4** is orientated in the same direction.

A good performance of the prediction model is observed in the case that we mesh the **M4** by mesh IV and using the CGLS method to solve the inverse problem. Here, we used the *L*-curve criterion as as stopping criterion for the CGLS method. The *L*-curve in this particular case is found in figure 6.5. We see that the optimal solution is found at  $k = 137$ .

The prediction of the magnetic signature is quite good in this case. We have that the relative error  $\tau$  at one meter below the **M4** satisfies

$$0.004 \leq \tau \leq 0.074$$

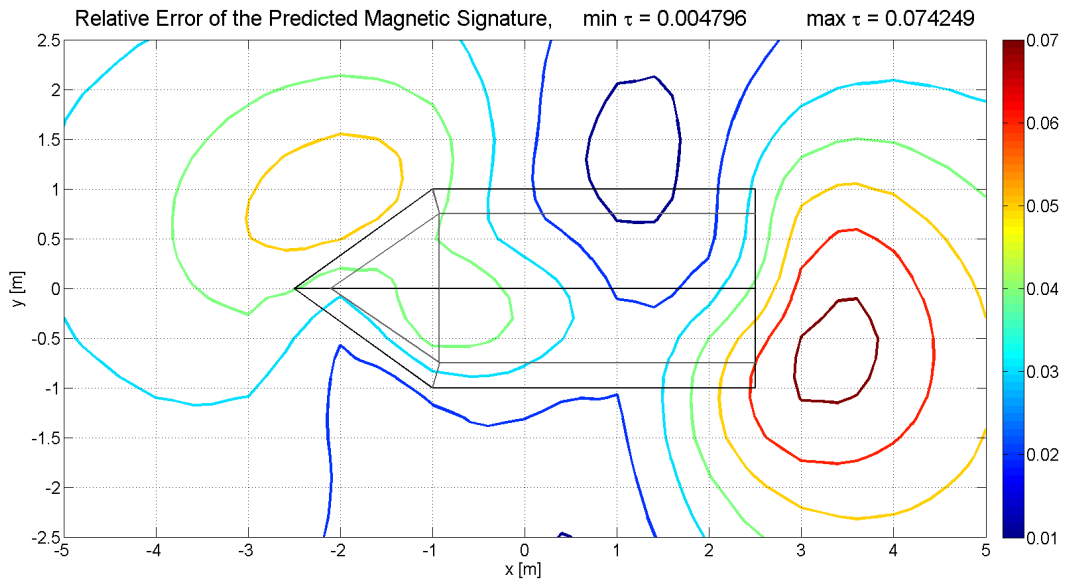
and that the absolute error of the predicted signature satisfies

$$4.5\text{nT} \leq \varepsilon \leq 117\text{nT},$$

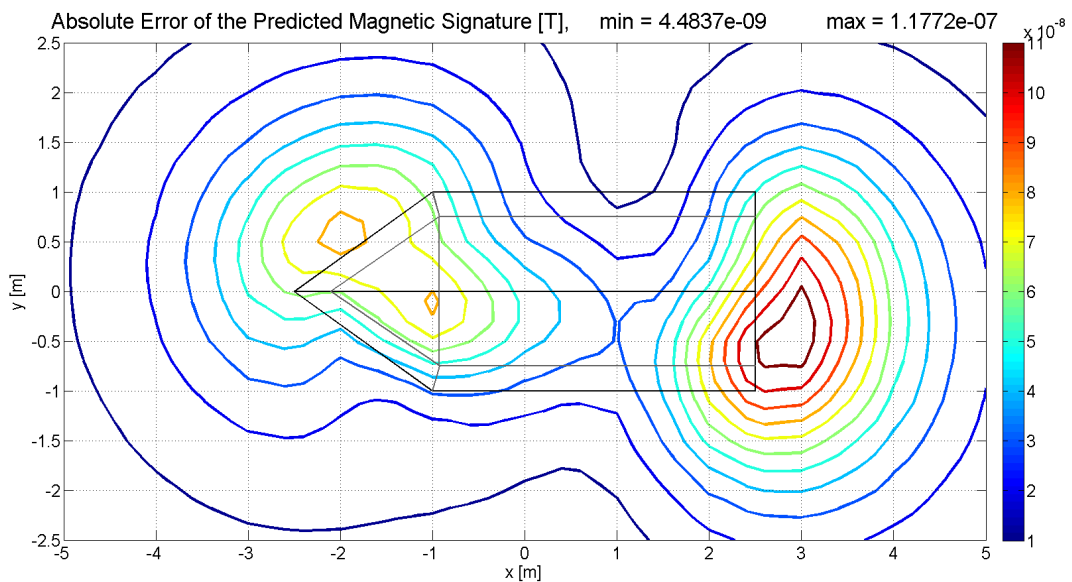
so the absolute error is maximal 117nT. The relative error and absolute errors at one meter below the **M4** are shown in figure 6.2. The predicted signature and COMSOL signature are shown in figure 6.3. Observe that the shape of the intensity of the

predicted magnetic signature is corresponding to the COMSOL magnetic signature, which shows that the magnetic sources of the inverse problem are well distributed in the **M4**.

In figure 6.4 and ??, the magnetic solutions  $f, g$  and  $h$  of the inverse problem show that the **M4** is acting like a bar magnet, with its magnetic poles at the stern and bow of the **M4**. The inverse problem seems to approximate the correct magnetic sources, although we only use 178 many measurements of the magnetic field inside the **M4**.

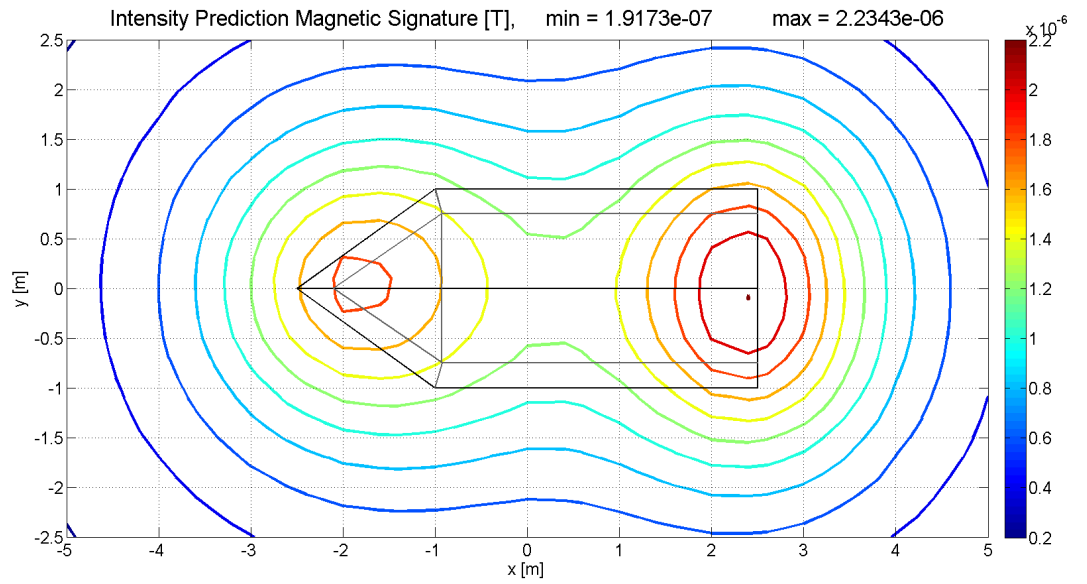


(a) Relative errors.

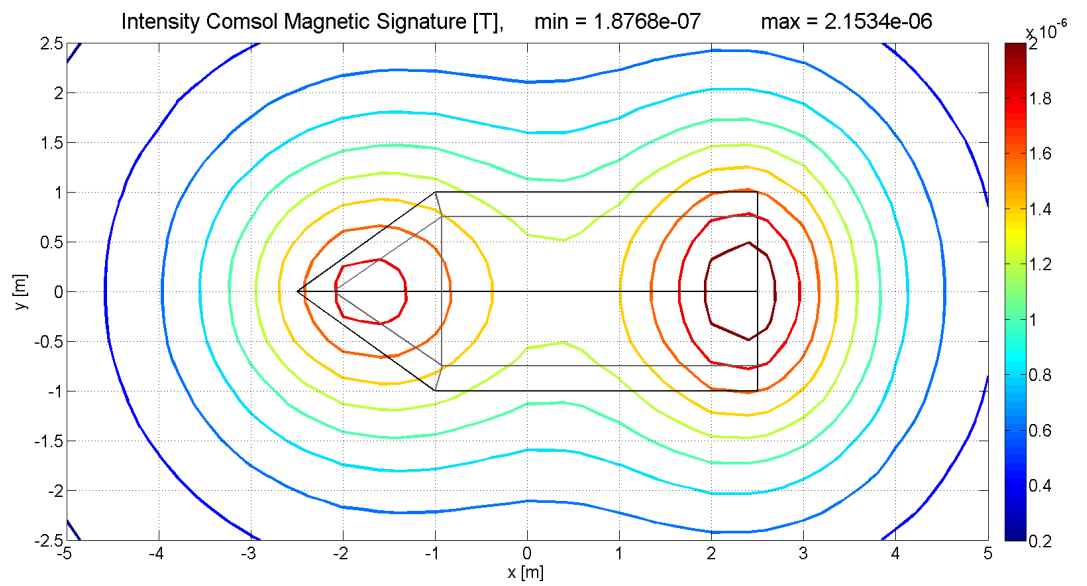


(b) Absolute errors.

Figure 6.2: The relative and absolute errors of the CGLS predicted signature.



(a) Prediction magnetic signature.



(b) COMSOL magnetic signature.

Figure 6.3: The CGLS predicted and COMSOL magnetic signature.

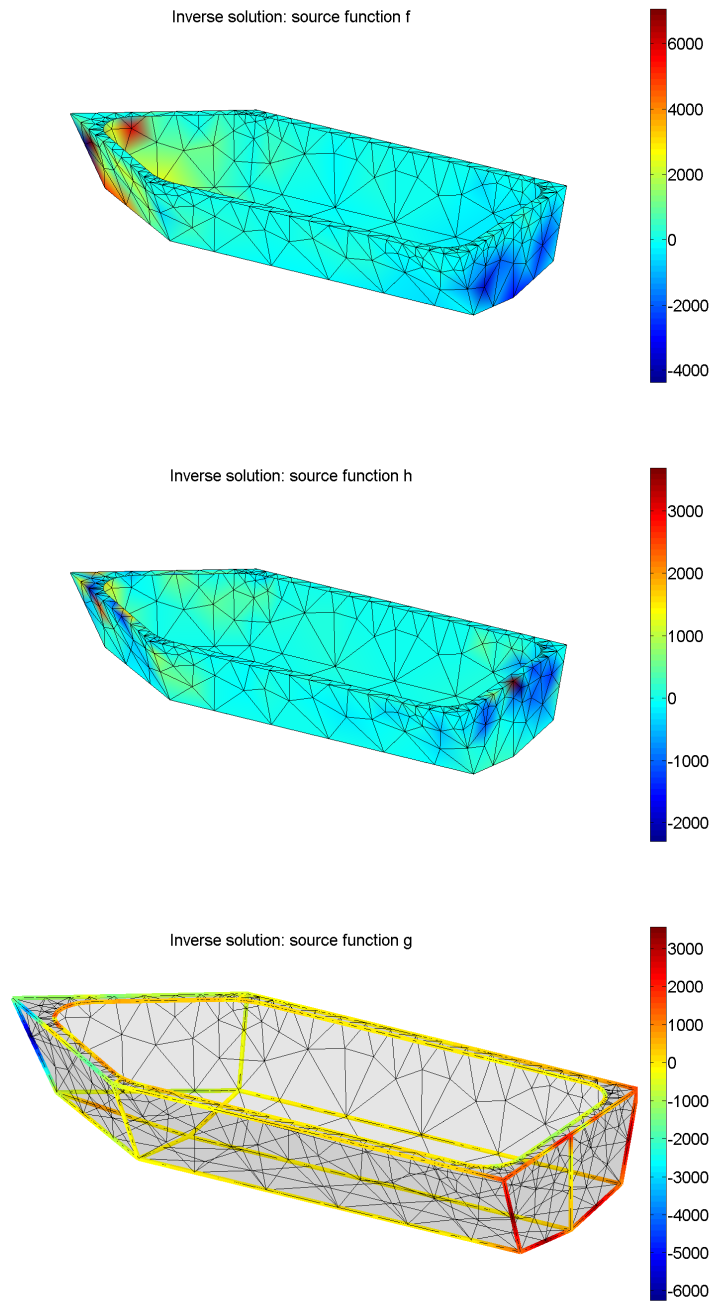


Figure 6.4: The magnetic sources  $f$ ,  $g$  and  $h$  in the **M4**, computed by the inverse problem.

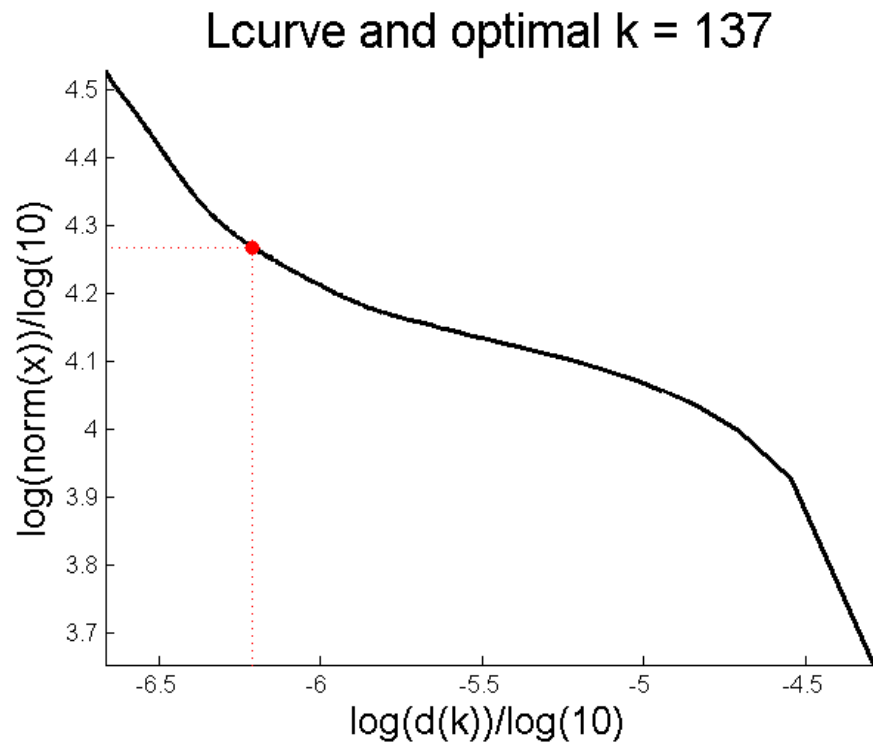


Figure 6.5: The  $L$ -curve in loglog-scale corresponding to the system  $Ax = b$  in the inverse problem described in section 6.2.1. Here, the optimal solution is found at  $k = 137$ .

## 6.3 Investigation of behavior of the prediction model

This section presents the analysis of our prediction model. In the introduction of this chapter we described different topics we considered in this analysis, such as the use of the solver in the inverse problem, the use of different meshes, neglecting the double layer potential and the influence of noise on the performance of the prediction model. These topics are covered in the next sections.

### 6.3.1 Direct solvers

The condition numbers involved in the inverse problem are all  $\mathcal{O}(10^{17})$ . As we already established in Chapter 3, large condition numbers imply that the inverse problem is ill-conditioned and therefore that direct solvers such as the SVD and QR method are useless for our simulations.

To illustrate the accuracy of solutions of direct solvers, we consider the **CIFV** routine where we use the SVD method as solver. We partition the **M4** by means of Mesh II, choose 176 measurements of the magnetic signature and execute the routine (see also Table A.1). In this situation we have  $\text{cond}(A) = 2.2 \cdot 10^{17}$ . For the solution of the inverse problem we have

$$r = \|\mathbf{b} - A\mathbf{p}\|_2 = 9 \cdot 10^{-18}$$

and thus the solution fits the measured data, stored in  $\mathbf{b}$ . In figure 6.6 we see the source solutions computed by the SVD method and in figure 6.7 the corresponding predicted magnetic signature at one meter below the **M4** is shown. Although the inverse solution fits the data well, the magnetic signature that it induces does not make any sense.

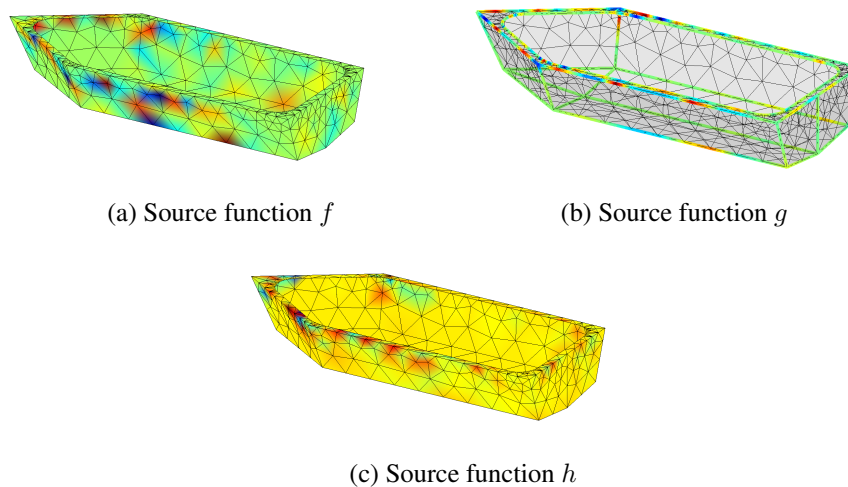


Figure 6.6: Source solutions computed by the SVD method. The source functions show large variations and many local extremes.

Both figure 6.7 and Table A.1 indicate that the solutions found by the SVD method are useless as the magnetic signature prediction does not coincide at all with the real signature: the shape of the predicted signature is very odd and not physical. We conclude that direct solvers (without any regularization) lead to useless solutions of the inverse problem.

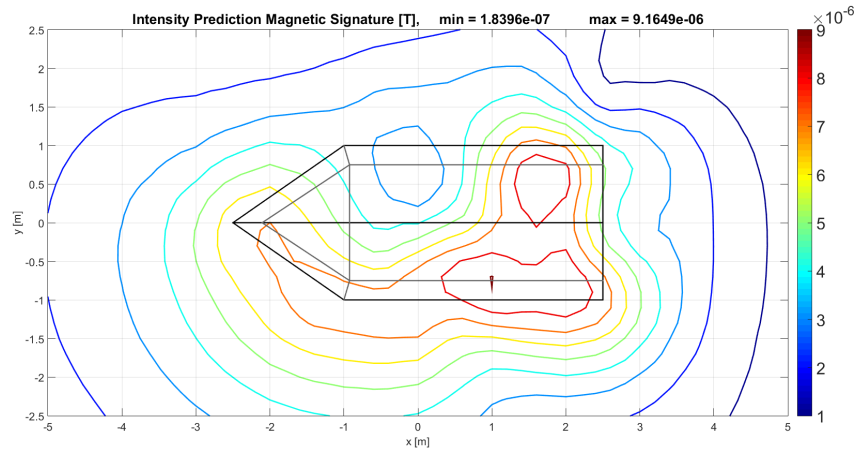


Figure 6.7: Predicted magnetic signature computed via the SVD method. The magnetic signature has a strange shape. This is caused mainly by the chaotic behavior of the non-physical source functions determined from the inverse problem displayed in figure 6.6.

### 6.3.2 SVD analysis

In this section we consider the SVD decomposition of a linear inverse problem that we encounter in the simulations. We look at one specific example, but the behavior is similar for each system that we encounter. We have seen in Chapter 4 that singular values describe the behavior of the inverse problem. The number of singular values depends on the number of measurements taken as input in the inverse problem. In particular, if we take  $n$  measurements of the magnetic field, then there is a total of  $3n$  singular values. In Appendix , some values of the singular values and their corresponding SVD components are presented. Also the ratio between the singular value and the associated SVD component is shown. The SVD decomposition is found in the **CIFV** routine discussed in section 6.2.1.

The last 6 singular values are below the machine precision  $\varepsilon = 2.2 \cdot 10^{-16}$ , which means that those values cannot be trusted. We may say that these are practically zero. In Figure 6.9c the singular values are shown in a graph and in 6.9b the corresponding SVD components are shown. Observe that both the singular values and the corresponding SVD components decrease. However, from the ratios in Table A.2 we observe that the singular values decreases much faster than the SVD components. This means that the *Picard Criterion* (see section 4.3) is violated, as the SVD components do not decrease faster than the singular values. Hence the naive solution represents a solution that is not “nice”.

In this case, the smallest singular values are approximately  $10^{-15}$  (when we neglect the last singular values below the machine precision). Recall that the naive solution is given by

$$\mathbf{x}^\dagger := A^\dagger(\mathbf{b}_e + \mathbf{e}) = \sum_{i=1}^r \frac{\langle \mathbf{b}_e, \mathbf{u}_i \rangle}{\sigma_i} \mathbf{v}_i + \sum_{i=1}^r \frac{\langle \mathbf{e}, \mathbf{u}_i \rangle}{\sigma_i} \mathbf{v}_i, \quad r := \text{rank}(A) \quad (6.2)$$

Observe that in the presence of a noise term  $\mathbf{e}$ , the naive solution drifts away from the exact solution because the second summation becomes large, if singular values are small. Thus, small perturbations in the right-hand side due to noise spoil the solution and therefore regularization is really necessary.

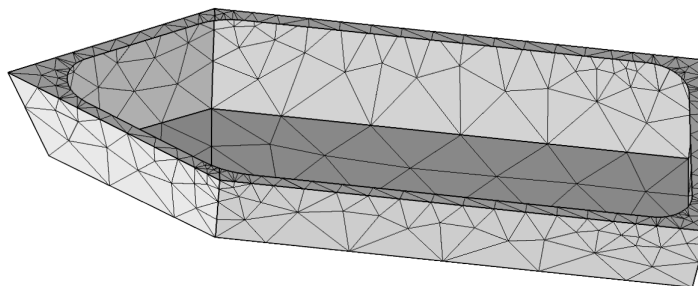
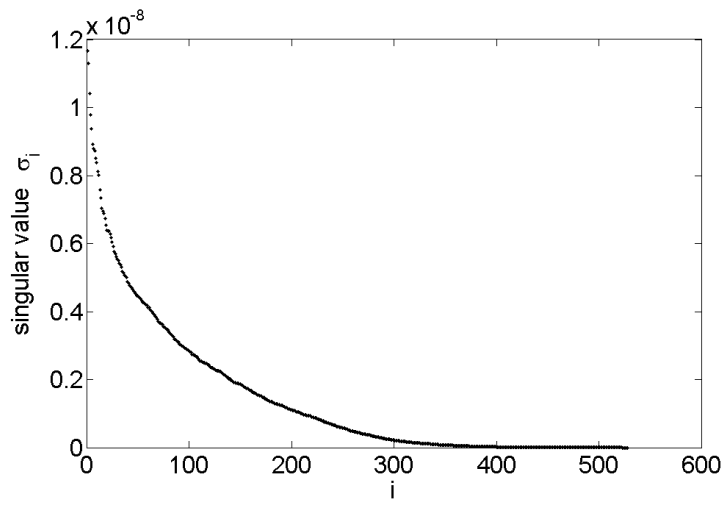
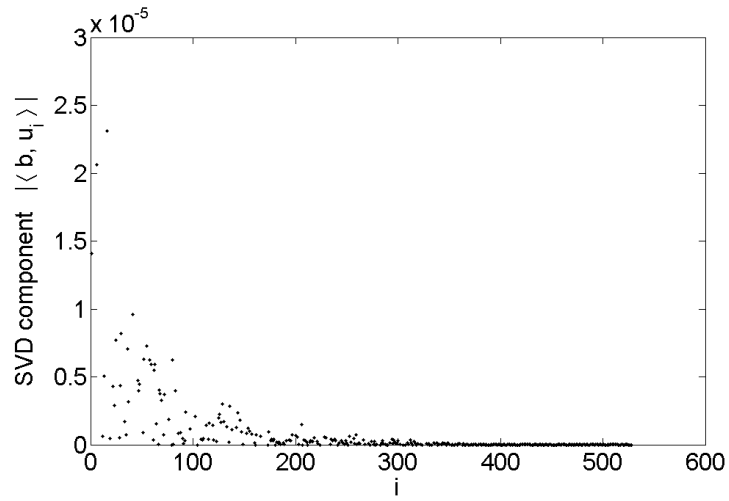


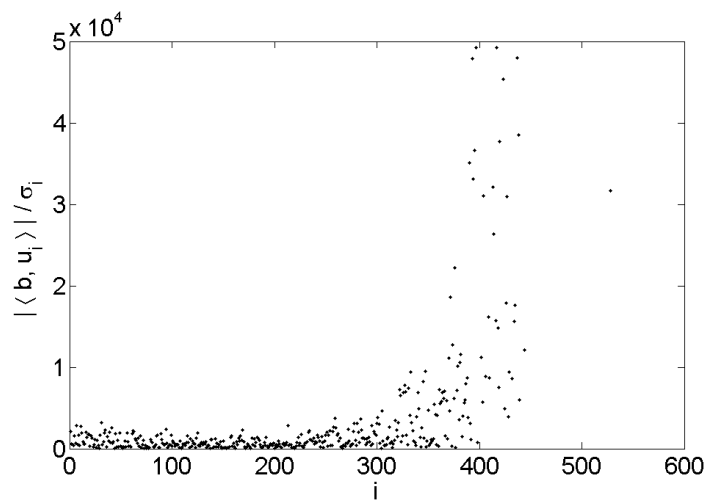
Figure 6.8: Mesh IV, defined on the mock-up.



(a) Singular values of the inverse problem.



(b) SVD components of the inverse problem.



(c) The quotients of SVD components and singular values.

Figure 6.9: The singular values and the SVD components of the inverse problem.

### 6.3.3 CGLS and SVD+Tikh simulations

In Table A.1 the errors of the prediction for different solvers and meshings of the mock-up **M4** are shown. We see that for the CGLS method and SVD+Tikh method the prediction model performs good. The performance of the prediction is already illustrated in section 6.2.1.

The relative and absolute error plots in figure 6.2 show that the prediction model has some difficulties to predict the shape of the signature at the stern and at the bow. Note that the distribution of the relative errors and the absolute errors are a bit suspicious. An explanation for the typical shape is that the signature that COMSOL simulates is an approximation of the magnetic field, and contains rounding errors and approximation errors caused by the FEM used.

### 6.3.4 Anomalies in the prediction model

Looking at the errors in the predictions of the magnetic signature, we observe that there are some typical spots at the stern and bow of the mock-up where the relative error is high. Two explanations of these local anomalies are the following.

We may argue that these anomalies are caused in the numerical approximation of the real magnetic signature by COMSOL. Of course, COMSOL uses a Finite Element Method to compute that magnetic signature of the **M4** and although we have used a very fine partition to compute the signature, we cannot avoid any numerical errors in the computation. Furthermore, any human mistakes in simulating the magnetic signature cannot be ruled out and we should emphasize that COMSOL describes the physics in a different way.

Another explanation may be that the prediction model has difficulties at those points where the gradient of the vector field<sup>1</sup>  $\nabla\mathbf{B}$  is large. If we look at the locations of the anomalies we see that the anomalies are indeed nearby large gradients of the vector field. However if we look at a background field orient along the  $y$ -direction we observe that the anomalies are still positioned at the stern of the mock-up. Therefore this explanation tends to be false.

## 6.4 Double Layer Component in the Magnetic Field Formulation

For a thin magnetic shell  $\Omega$ , the magnetic shielding condition, described in Section 5.2.1, is used to describe the induced magnetic field. In this description we assume that, when the steel object has a very small thickness, the magnetization of  $\Omega$  is tangential and that any magnetization normal to the shell  $\Omega$  can be neglected. This condition is used in the simulation of the magnetic signature of the mock-up in COMSOL.

---

1. Suppose that  $\mathbf{v} : \mathbb{R}^m \rightarrow \mathbb{R}^n$  is a vector field. Write  $\mathbf{v} = \sum_{i=1}^n v_i(x_1, \dots, x_m) \mathbf{e}_i$  where  $\{\mathbf{e}_1, \mathbf{e}_2, \mathbf{e}_3\}$  is an orthonormal basis for  $\mathbb{R}^n$ . Then  $\nabla\mathbf{B}$ , the gradient of the vector field  $\mathbf{B}$ , is defined as the matrix  $(\partial_i v_j)_{i,j=1,2,3}$  (the Jacobian of  $\mathbf{v}$ ).

### 6.4.1 Changing the prediction model

In our forward problem formulation, the potential that solves Poissons problem is built out of single layer potentials and a double layer potential. This potential leads to the following description of the magnetic induction field outside the mock-up that was given by (eq 2.3)

$$\begin{aligned} \mathbf{B}(\mathbf{r}) = & -\frac{\mu_0 t}{4\pi} \iint_{\Omega} \frac{\mathbf{r} - \mathbf{r}'}{|\mathbf{r} - \mathbf{r}'|^3} \nabla \cdot \mathbf{M}(\mathbf{r}') d\mathbf{r}' + \frac{\mu_0 t}{4\pi} \int_{\partial\Omega} \frac{\mathbf{r} - \mathbf{r}'}{|\mathbf{r} - \mathbf{r}'|^3} \mathbf{n}'(\mathbf{r}') \cdot \mathbf{M}(\mathbf{r}') d\mathbf{r}' \\ & + \frac{\mu_0 t}{4\pi} \iint_{\Omega} \frac{\partial}{\partial \nu'} \left( \frac{\mathbf{r} - \mathbf{r}'}{|\mathbf{r} - \mathbf{r}'|^3} \right) \mathbf{n}'(\mathbf{r}') \cdot \mathbf{M}(\mathbf{r}') d\mathbf{r}' \end{aligned} \quad (6.3)$$

where the third integral corresponds to the double layer potential. Now for our mock-up it holds that the thickness of the steel is relatively small to the other dimensions of the mock-up. Therefore we argue that the contribution of this double layer component can be neglected in the prediction model. The magnetic field in the forward problem is then described by

$$\overline{\mathbf{B}}(\mathbf{r}) = -\frac{\mu_0 t}{4\pi} \iint_{\Omega} \frac{\mathbf{r} - \mathbf{r}'}{|\mathbf{r} - \mathbf{r}'|^3} \nabla \cdot \mathbf{M}(\mathbf{r}') d\mathbf{r}' + \frac{\mu_0 t}{4\pi} \int_{\partial\Omega} \frac{\mathbf{r} - \mathbf{r}'}{|\mathbf{r} - \mathbf{r}'|^3} \mathbf{n}'(\mathbf{r}') \cdot \mathbf{M}(\mathbf{r}') d\mathbf{r}' \quad (6.4)$$

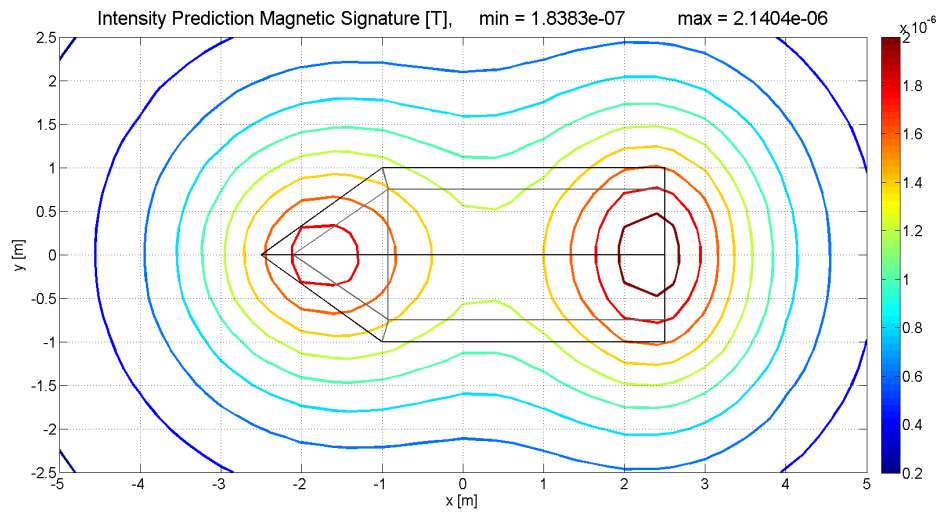
and the inverse problem is the task of finding magnetic sources  $f$  and  $g$  that fit the measurements.

### 6.4.2 Results neglecting the double layer component

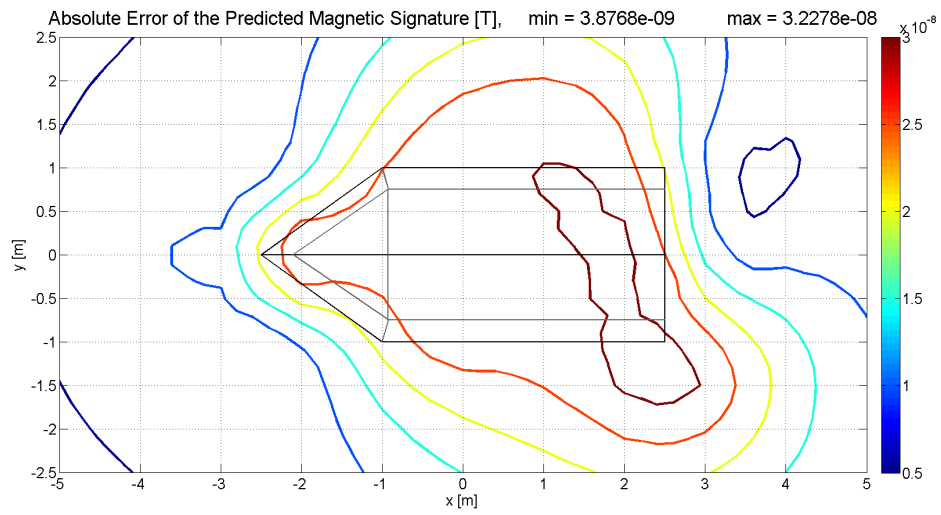
We investigate the performance of the prediction model in the absence of the double layer component. In Table 6.2 the errors of the prediction can be found. Observe that when we neglect the double layer component, the performance of the prediction model increases significantly. In particular, for mesh  $V$  we see that the prediction is more or less perfect, with an absolute error of maximal 34nT. In figure 7.9c the results in this case are shown.

|              |     | With double layer component |              |              | Without double layer component |              |              |
|--------------|-----|-----------------------------|--------------|--------------|--------------------------------|--------------|--------------|
| Mesh         |     | $\varepsilon_{max}$ [nT]    | $\tau_{min}$ | $\tau_{max}$ | $\varepsilon_{max}$ [nT]       | $\tau_{min}$ | $\tau_{max}$ |
| Solver: CGLS | I   | 208                         | 0.004        | 0.097        | 106                            | 0.018        | 0.055        |
|              | II  | 176                         | 0.012        | 0.103        | 74                             | 0.001        | 0.042        |
|              | III | 152                         | 0.009        | 0.093        | 65                             | 0.002        | 0.042        |
|              | IV  | 71                          | 0.003        | 0.054        | 71                             | 0.003        | 0.054        |
|              | V   | 126                         | 0.007        | 0.088        | 34                             | 0.005        | 0.042        |
|              | VI  | 150                         | 0.007        | 0.087        | 158                            | 0.021        | 0.081        |

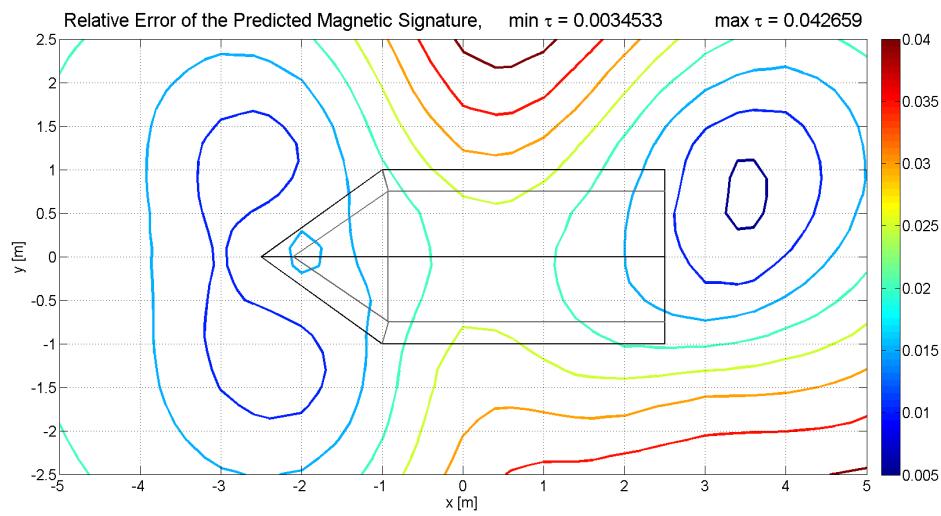
Table 6.2: Simulation errors based on 176 measurements inside the **M4**. We compare the simulation errors of the prediction with and without the double layer component.



(a) Predicted magnetic signature.



(b) Absolute error of the predicted signature.



(c) Relative error of the predicted signature.

Figure 6.10: The relative errors and the absolute errors made by the prediction model, when we neglect the double layer component.

Although neglecting the double layer component leads to better predictions, we have to be careful. The increase of performance can be explained by the mathematical physical model of the static magnetic field inside COMSOL. As described in section 5.2.1, the computation of the magnetic field in COMSOL uses the magnetic shielding boundary conditions to reduce the complexity of the problem. We argue that in this model, the normal component of the magnetic field is neglected too and that this causes the increase of performance that we have observed in this section.

It remains a question if the double layer component can be neglected in practice. An experiment should clarify if this is the case.

## 6.5 Noisy Measurements and the use of Regularization

In the previous sections we analyzed the prediction model's performance. We have seen the performance of the prediction model for different meshes and solvers, and we saw that the CGLS method produced the best inverse solutions. However, in the simulations we did not consider any noisy measurements (besides any numerical rounding errors in COMSOL, but these are small). In this section we consider noisy measurements and investigate to what extent the regularizing behavior of the CGLS can deal with this noise.

### 6.5.1 Modeling of noise

Suppose that our discrete inverse problem is of the form

$$A\mathbf{p} = \mathbf{b} + \mathbf{e}$$

where we introduce a noise term  $\delta$  in the vector  $\mathbf{b}$ . We model the noisy  $\delta$  as Gaussian noise with mean zero. For each measurement vector  $\mathbf{x} \in \mathbb{R}^3$  at some sensor position we have that

$$\delta \sim \mathcal{N}(0, \sigma^2 I_3)$$

with probability density

$$\pi_{\delta}(\mathbf{x}) = \frac{1}{(2\pi)^{\frac{3}{2}} \sigma^3} \exp\left(-\frac{1}{2\sigma^2} \|\mathbf{x}\|^2\right)$$

The covariance matrix  $\Sigma = \sigma^2 I_3$  indicates that the entries  $\delta_i$  of noise vector  $\delta$  are independent. Noise that is modeled in this manner is called *white Gaussian noise*. For  $K$  sensor positions the noise vectors can be concatenated to a vector  $\mathbf{e}$ , the noise vector that appears in the discrete inverse problem.

When we measure the magnetic field inside the **M4** using a magnetic flux-gate sensor, experience learned that the measurement can deviate a couple of hundreds of nanotesla. More specifically,

$$\|\mathbf{B}_{\text{exact}}(\mathbf{r}) - \mathbf{B}_{\text{measured}}(\mathbf{r})\|_2 \leq 300nT, \quad \text{for each measurement } \mathbf{r}$$

Therefore, a reasonable value for  $\sigma$  is

$$3\sigma = \frac{1}{3}\sqrt{3} \cdot 300 \cdot 10^{-9}T$$

so that 99% of the mass below the probability density lies within the interval  $[-3\sigma, 3\sigma]$ . This means that the noise in each measurement most likely varies between  $0nT$  and  $300nT$ . Hence, the model for the noise in each sensor position is given by

$$\delta \sim \mathcal{N}(0, \sigma^2 I_3), \quad \sigma = \frac{1}{9}\sqrt{3} \cdot 300 \cdot 10^{-9} \quad (6.5)$$

### 6.5.2 A remark on independency in the modeling of noise

We must keep in mind that, in practice, a fluxgate magnetic sensor measures the three components of the field by three small coils. These coils are placed inside the sensor perpendicular to each other. Recall Faraday's law of induction: a current inside a coil generates a magnetic field. Therefore, at a small scale, the field in the three coils are coupled. This is a reason to believe that the noise in a measurement is, at some point, dependent. It is unclear at this moment what the influence of the coupled behavior of the coils is on the noise. Therefore, for now we consider the modeling of the noise as described above.

### 6.5.3 Numerical tests

In this section we restrict ourselves to a fixed prediction of the magnetic signature, and investigate the effect of *regularization by truncation* (see section 4.8) when the on-board measurements of the magnetic field are contaminated by noise.

We start by choosing the predicted magnetic signature described in section 6.2.1. By  $\mathbf{B}_{\text{sign}}$  we denote the predicted magnetic signature in this simulation. The prediction of  $\mathbf{B}_{\text{sign}}$  was done in any absence of noise ( $\mathbf{e} = \mathbf{0}$ ) in the measurements. Recall that the absolute error of this predicted signature is

$$4.5\text{nT} \leq \varepsilon \leq 117\text{nT}$$

Next, we model a noise vector  $\mathbf{e} \in \mathbb{R}^{3K}$  via the Gaussian noise model discribed in 6.5, where  $K$  is the number of sensorpositions and add this vector to the discrete inverse problem.

The discrete inverse problem is then solved using the CGLS method in combination with the  $L$ -curve criterion, and leads to a predicted signature based on noisy measurements. This simulation is done a number of times and leads to a set of predictions of the magnetic signature

$$\{\mathbf{B}_1, \mathbf{B}_2, \dots, \mathbf{B}_T\}$$

where  $T$  is the number of simulations. For each simulation  $i \leq T$  we compute the relative error

$$\tau_i(\mathbf{r}) = \frac{\|\mathbf{B}_{\text{sign}}(\mathbf{r}) - \mathbf{B}_i(\mathbf{r})\|_2}{\|\mathbf{B}_{\text{sign}}(\mathbf{r})\|_2}$$

and absolute error

$$\varepsilon_i(\mathbf{r}) = \|\mathbf{B}_{\text{sign}}(\mathbf{r}) - \mathbf{B}_i(\mathbf{r})\|_2$$

at one meter below the mock-up. We define the mean of the relative and absolute errors

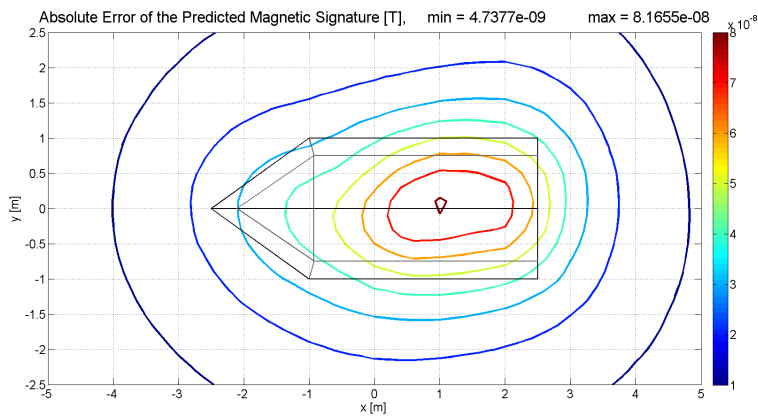
$$\bar{\tau} = \frac{1}{T} \sum_{i=1}^T \tau_i, \quad \bar{\varepsilon} = \frac{1}{T} \sum_{i=1}^T \varepsilon_i$$

The mean of the relative and absolute errors are used to investigate the regularizing behavior of the CGLS method (in combination with the  $L$ -curve criterion). By looking

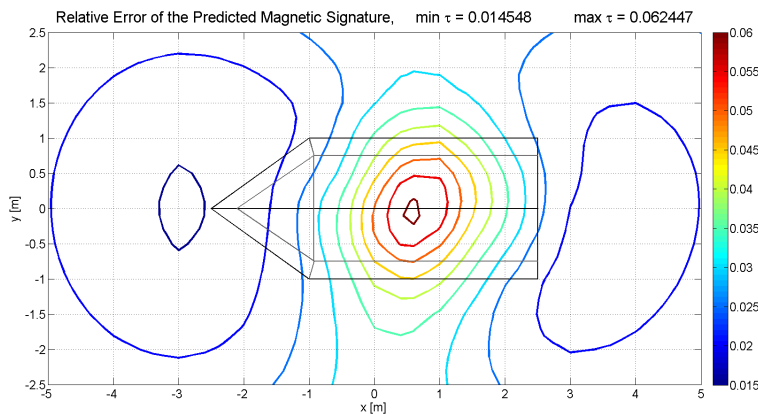
at the values of  $\bar{\tau}$  and  $\bar{\varepsilon}$  we take away any rare spike that can occur when the noise vectors  $e$  are generated.

The above procedure is executed for  $T = 20$ . The results of this simulation is shown in figure 6.11. The absolute error plot shows that, although the predicted signatures are done based on noisy measurements, the model produces an accurate prediction of the magnetic signature. The maximal mean absolute error is around 82nT, which means that in general the prediction model makes an additional error of 82nT when we are using noisy measurements.

Adding up the values of the absolute error of  $\mathbf{B}_{\text{sign}}$  (with respect to the COMSOL signature) and the mean absolute error we conclude that in general the prediction model makes an estimated absolute error of around 200nT, which is around 10% of the intensity field  $\|\mathbf{B}_{\text{sign}}\|_2$ .



(a) Mean absolute error.



(b) Mean relative error.

Figure 6.11: Mean errors between  $\mathbf{B}_{\text{sign}}$  and the CGLS predicted signatures with noisy measurements.

## 7 Measurement Campaign and application of Prediction Model

A measurement campaign took place in Germany to support the validation of the proposed prediction model. In this chapter we test the performance of the prediction model based on the data of the measurement campaign.

In section 7.1 the measurement campaign is described. Some observations are made during the campaign and we discuss these observations in section 7.2. The resulting measurements are shown in section ?? and in section ?? we demonstrate the performance of the prediction model using real data.

### 7.1 Measurement Campaign

A measurement campaign took place in October 2015 at the measurement range “Grosse Eva” at the Wehrtechnische Dienststelle 71 (WTD71) in Borgstedt, Germany. The WTD71 uses the measurement facility to measure small magnetic objects such as tanks, and to demagnetize them to certain norms if necessary. The small inhomogeneities in the background field are of less importance for WTD71, because they are more interested in the relative magnetic disturbances of the object.

However, in our research we are interested in the absolute disturbances. This places greater demands on the accuracy of the background field, sensor positions and the measurements of the magnetic field. In particular, the prediction model uses sensor positions for inverse modeling of the magnetic sources. For good performances of the prediction model, the position of the sensor must be known accurately.

A mock-up model is built by the Marine Bedrijf in Den Helder, the Netherlands, and is transported to the item range in order to be measured under several magnetic conditions. The “Mock-up for Magnetic Monitoring Measurements”, simply called the M4, is built out of steel plates that are 4 mm thick. The steel plates are typically used in the construction of naval vessels. The M4 has dimensions of approximately 5 m (length) x 2 m (width) x 1 m (height) and has a weight of approximately 1000 kg.

The goal was to collect data that serve as input for the development of the prediction model for magnetic signature monitoring and to collect data that can be used to investigate the Hysteresis behavior of the steel used in the mock-up. The measurement campaign was a great opportunity to get some experience in measurements and to understand the complexity of the application of the prediction in practice.

### 7.1.1 Campaign plan

We want to measure the magnetic induction field  $\mathbf{B}$  surrounding the mock-up under different magnetic states and background fields. The magnetic state (or Permstate) is defined as the permanent part of the magnetization inside the steel of the mock-up. For each magnetic state, we consider several background fields. The permanent magnetic state can be changed by a strong magnetic background field.

#### 7.1.1.1 Helmholtz coil

In the measurement facility “Grosse Eva”, two coil systems are built-in. The coil configurations are based on the so-called *Helmholtz Coil*. However, the coils systems in the facility are different. The specific details are classified.

A Helmholtz coil is a device for producing a region with a nearly uniform magnetic field. A schematic drawing of a Helmholtz coil is found in figure 7.1. It consists of two solenoids of radius  $R$  on the same axis, positioned at a distance  $R$  between the two solenoids.

The computation of the exact magnetic field at any point surrounding the Helmholtz coil is very complex. However, at the midpoint (at  $x = R/2$ ) between the two electromagnets the field is computed easily using Biot-Savart law:

$$\mathbf{B}(x = R/2) = \left(\frac{4}{5}\right)^{\frac{3}{2}} \frac{\mu_0 n I}{R}$$

where  $\mu_0$  is the permeability of vacuum,  $n$  is the number of turns in each coil,  $I$  is the coil current (in amperes) and  $R$  is the coil radius (in meters). We see that the field is proportional to the coil current and the number of windings. Therefore, in theory, any uniform field can be generated by this coil configuration.

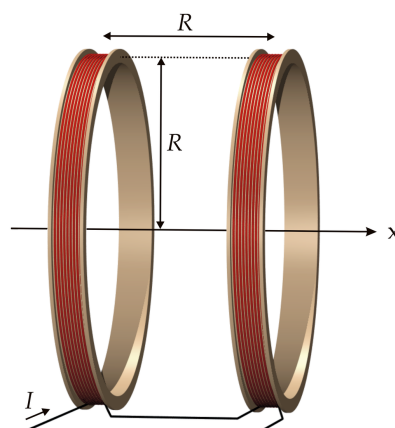


Figure 7.1: A schematic drawing of a Helmholtz coil. Near the x-axis the field, generated by the electromagnets, is uniform.

#### 7.1.1.2 Deperming

We start with *de-perming* the mock-up to a minimal permanent magnetization level. The de-perm process is done by changing the background field in the facility in some special manner, using a Helmholtz coil system inside the facility. The magnetic state obtained serves as the initial magnetic state of the **M4** and it ensures us that the values of the magnetic field are within the range of the magnetic sensors used.

#### 7.1.1.3 Permstate I

After the deperming, the magnetic field under five different background field conditions is measured. The background field can be changed using the larger Helmholtz coil system inside the measurement facility. In fact, the measurement facility consists of several Helmholtz coil configurations. These can be used to change the background field inside the facility.

The different background fields are: (1) in absence of the background field (zero field), (2, 3, 4) uniform background fields in the three directions x, y and z with a strength of  $50\mu T$ , and (5) again a measurement with no background field. The last measurement is done to see whether the three uniform background fields changed any permanent magnetization in the mock-up significantly. A possible change would indicate a change in the permanent magnetization.

#### 7.1.1.4 Remark on the positioning of the mobile sensor

For each field condition we want to measure the magnetic induction field **B** inside the mock-up at several measurement points and we want to measure the magnetic field below the mock-up at several depths. Around 150 manual measurements of the magnetic field inside the **M4** are planned.

To do accurate measurements inside the mock-up with a mobile sensor, a grid is defined inside the mock-up, see figure 7.2. The local coordinates, defined by the grid, can be transformed to the global coordinate system that is used in the prediction model, by suitable coordinate transformations. The measurements inside the mock-up are done manually. The mobile sensor is attached to a aluminium frame at a fixed distance, so that each on-board measurement was done at a fixed distance to the mock-up. We fixed the mobile sensor at a height of 20cm. So, in local coordinates, the *z*-coordinate of each measurement is the same.

By moving the mock-up's position with respect to the sensor array, we create a grid of measurements of the magnetic field below the mock-up. This grid of measurements will serve as input for the validation of the mathematical-physical model. It is of great importance to know the location of the measurement positions accurately for the performance of the current prediction model.

#### 7.1.1.5 A remark on measuring the magnetic signature

For each run, the magnetic signature is measured of the **M4** for four different headings: north, east south and west. The mock-up is moved from the south of the hall to the north, along a rail. Below the rail an array of sensors are fixed at different heights, for near field measurements and far field measurements. Near field we mean the magnetic field between one meter and two meters below the mock-up, while the far field is the magnetic field at two meters or more. Changing the heading of the mock-up is done manually, by rotating the platform of the trolley where the mock-up is placed on.

#### 7.1.1.6 Hysteresis Modeling

For further studies it is important to know how the magnetization changes over time, when we change the background field in the de-perm and perm process and when we change the background field for our measurements. The data can be used to further understand the *hysteresis* of steel, i.e. the magnetic history of steel. However, this study is out of the scope of this project.

#### 7.1.1.7 Change the permstate of the **M4**

After the five runs have been executed, we change the permanent magnetic states using the strong Helmholtz coils. This procedure is called a *perm-process*. The Perm-process is an time-intensive one. Note that for the new permstate, the magnetic signature of the **M4** must be within the measuring range of sensors. Otherwise, the measurements cannot be trusted.



Figure 7.2: A grid, painted on the inside of the mock-up, that is used to do accurate on-board measurements.

#### 7.1.1.8 Permstate II

With the new perm state, we execute another set of measurements. Instead of considering the background fields in the first run, we looked at another set of background fields: (1) zero field, (2) the local earth magnetic field at Bünsdorf, (3) a uniform background field in the z-direction and (4) a uniform background field in the x-direction. The earth magnetic field at the facility in Bünsdorf is approximately

$$B_x = 17575nT, \quad B_y = 690nT, \quad B_z = 46500nT$$

These values are found using a numerical model of the “National Centers for Environmental Information” [22]. Bünsdorf is at latitude  $54.4^\circ$  North and longitude  $9.730542^\circ$  East.

#### 7.1.1.9 Schedule

In table 7.1 we give an overview of the plan for the measurement campaign. Observe that by zero field, we mean that the Helmholtz coils generate a magnetic field that cancels out the earth magnetic field.

|  |  |
|--|--|
| <b>1. Deperm</b>   | De-perm the mock-up to minimal permanent magnetization by using the system of large coils. |
| <b>2. Permstate I</b>  |  |
| (a)  | No background field / zero field   |
| (b)  | Uniform background field in $\mathbf{u}_x$ direction, intensity of $50\mu T$               |
| (c)  | Uniform background field in $\mathbf{u}_y$ direction, intensity of $50\mu T$               |
| (d)  | Uniform background field in $\mathbf{u}_z$ direction, intensity of $50\mu T$               |
| (e)  | No background field / zero field   |
| Each item consists of 150 manual readings and a signature measurement using the near field sensor array. |  |
| <b>3. Perm</b>   | The magnetic state of the mock-up is changed by a Perm procedure.                          |
| <b>4. Permstate II</b>   |  |
| (f)  | No background field / zero field   |
| (g)  | Local background field at Bünsdorf   |
| (h)  | Uniform background field in $\mathbf{u}_z$ direction, intensity of $50\mu T$               |
| (i)  | Uniform background field in $\mathbf{u}_x$ direction, intensity of $50\mu T$               |
| Each item consists of 150 manual readings and a signature measurement using the near field sensor array. |  |

Table 7.1: An overview of the measurement campaign plan. Items (a) – (i) indicate the measurements done in the facility.

## 7.2 Observations during the campaign

In this section we discuss three observations we made during the measurement campaign in October 2015.

### 7.2.1 Inhomogeneity of the background field

We have observed that the magnetic field inside the facility is quite inhomogeneous. When the coil systems were disabled, we used a mobile sensor to measure the magnetic field at five positions inside the facility (near the location where we measured the **M4**). So only the local background field and possible stray fields were measured.

The values are given in table 7.2. The positions of the measurements are sketched in figure 7.3. Here, we have marked the location of the **M4** and the trolley by the dashed lines. The mock-up was removed when we did the five measurements.

|     | $B_x$ (nT) | $B_y$ (nT) | $B_z$ (nT) |
|-----|------------|------------|------------|
| (1) | 17418      | 2146       | 46555      |
| (2) | 17941      | 2665       | 46310      |
| (3) | 18148      | 2694       | 46136      |
| (4) | 17148      | 1887       | 46603      |
| (5) | 17426      | 860        | 46664      |

Table 7.2: Values of the background field, measured at different positions, as described in figure 7.3.

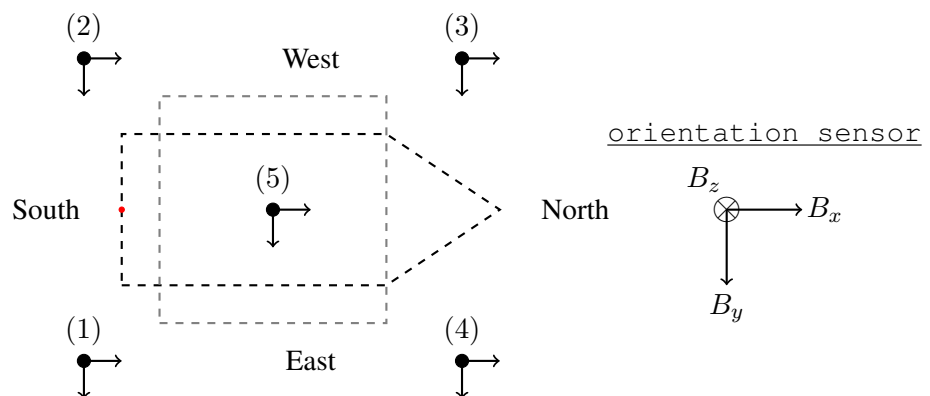


Figure 7.3: **(left)**: Positions of measurements and direction of the local background field at Bünsdorf. The origin of the global coordinate system is denoted by the red dot. In gray: the trolley on which the mock-up is placed on. **(right)**: The orientation of the mobile sensor is sketched (right-hand side rule), so  $z$  is downwards.

An explanation for the inhomogeneity of the magnetic field is that there are all kinds of equipment and objects present in the hall. It is plausible that stray fields coming from these objects are causing this inhomogeneity. In particular, when we did measurements of the local earth field, the mock-up was placed at the end of the hall of the facility (the hall is approximately 50 meters long). It is possible that the magnetic field of the mock-up is sensed by the mobile sensor.

If we want to use the prediction model, we need to measure the magnetic field of the mock-up. However, in practice, a mobile sensor measures the sum of all magnetic contributions, say

$$\mathbf{B}_{\text{measurement}}(\mathbf{r}) = \mathbf{B}_{\text{background}}(\mathbf{r}) + \mathbf{B}_{\mathbf{M4}}(\mathbf{r})$$

The inverse problem uses the data  $\mathbf{B}_{\mathbf{M4}}(\mathbf{r})$  as input, so we need to find a way to separate the two fields and retrieve the values  $\mathbf{B}_{\mathbf{M4}}(\mathbf{r})$ .

If the background field were uniform, the value of the background field could be used to do a correction on the measured values. But we have seen that the background field is not uniform. To resolve this issue, we propose that we can do a correction by using the mean vector of the five measurements

$$\bar{\mathbf{B}} = \frac{1}{5} \sum_{i=1}^5 \mathbf{B}(\mathbf{r}_i)$$

as shown in figure 7.3 (without the  $\mathbf{M4}$ ). By taking the mean of the five measurements, we are confident that the correction is sufficient. Of course, if we want to do such a correction, we have to know the background field in each measurement point. But in practice this is not possible.

## 7.2.2 Manual measurements

The on-board measurements of each run are done manually, using the aluminum frame and the attached mobile sensor. We kept the corner aluminium frame at some lattice point of the white grid, shown in figure 7.2. The measurements of the mobile sensor are shown on a display in the center of the hall inside the facility. We wrote down the values of a single measurement in a spread sheet.

Doing a measurement in such a way is most likely inaccurate. We have to keep the sensor at some fixed position manually. This is very hard without any construction, so small variations in the position and the orientation of the sensor were clearly visible on the screen. The variations in the values of the measurements are around 500nT. Such variations can be problematic for the performance of the inverse problem. But at this point, we do not have a good overview how these variations are distributed.

It is better to keep a sensor at some measurement point, hold it there for some time, and use the mean of the measured values at that position as a measurement of the field. In this way any noise in the measurement is minimized. Unfortunately, this was

not possible in the facility. The data from the mobile sensor could not be exported directly. For future measurements it is important to overcome this.

Apart from the variations in the measured values due to movement of the sensor, we have seen that when the mobile sensor lies still, there was still some noise present in the measured field. This is most likely due to the internal structure and noise in a sensor, something that cannot be avoided. Luckily, regularization can deal with this kind of noise.

### 7.2.2.1 Orientation of the sensor

A mobile sensor is used to measure the magnetic field inside the mock-up. We have observed some odd behavior of this sensor.

We did the following experiment. We turned off the coil systems, so only the local background field of Bünsdorf (and strayfields) are present. First, we orient the mobile sensor as shown in figure 7.4. We wrote down the measured values of the local background field, rotated the mobile sensor clockwise over  $90^\circ$  and measured again, see figure 7.4. By rotating the sensor, the orientation of the sensor changes, and the magnetic field is measured in a different way.

The values of the measurement in the two situations are given in table 7.3. What we expected is that the field component  $B_y$  does not change if we go from situation I to II, because the  $y$ -component is pointing in the same direction. Also, we expect that the values of  $B_x$  and  $B_z$  are interchanged, with some extra minus signs. Remarkably, this was not the case. The values of  $B_x$  and  $B_z$  are more or less consistent with the orientation of the sensor. However, there is a difference of  $1145 - (1955) = 3000\text{nT}$  between the field components  $B_y$ . We do not know what causes this odd behavior. Most probably it is caused by some internal malfunctioning of the sensor, for instance by some magnetic material inside the sensor.

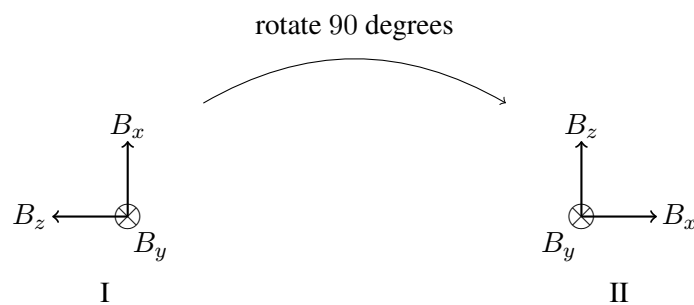


Figure 7.4: Orientation of sensor (I) and the orientation of the rotated sensor (II).

The observed behavior could be very problematic for our prediction model. Observe that we moved the mobile sensor when we measured the field inside the mock-up. We also changed its orientation now and then. The change of orientation therefore influences the values of the measurement a lot. This may have consequences for the performance of the prediction model.

| Component  | I      | II    |
|------------|--------|-------|
| $B_x$ (nT) | 2595   | 49854 |
| $B_y$ (nT) | -1955  | 1145  |
| $B_z$ (nT) | -50029 | 2112  |

Table 7.3: Values of the field components in situation I and II.

### 7.3 Results

At the end of the measurement campaign we obtained a large data set of measurements of magnetic signatures of the **M4**. To demonstrate the prediction model on real measurement data, we present the results of the measurement in a specific case, namely the measurements in the local background field at Bünsdorf. Recall that the earth background field at Bünsdorf is given by  $B_x = 17575nT$ ,  $B_y = 690nT$  and  $B_z = 46500nT$ .

In figure 7.6 and figure 7.5 the magnetic signature of the **M4** in the background field at Bünsdorf is shown.

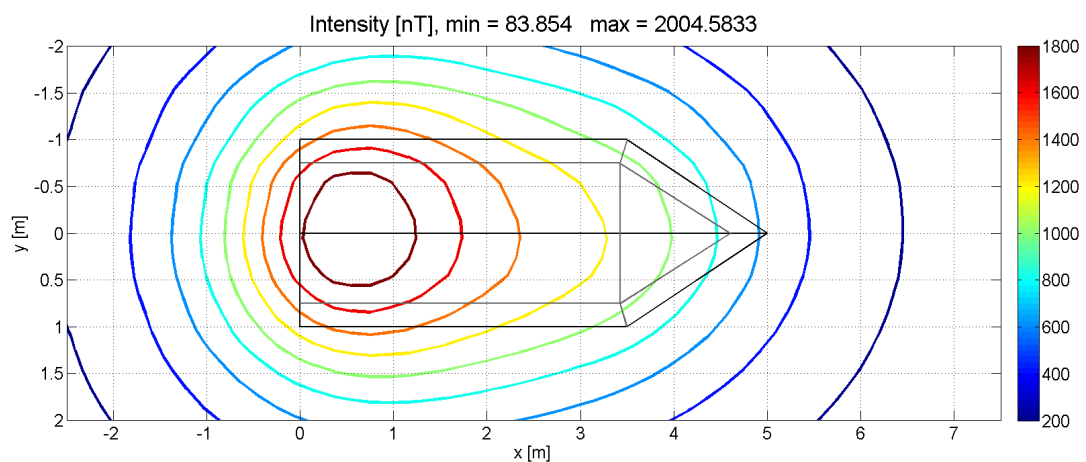
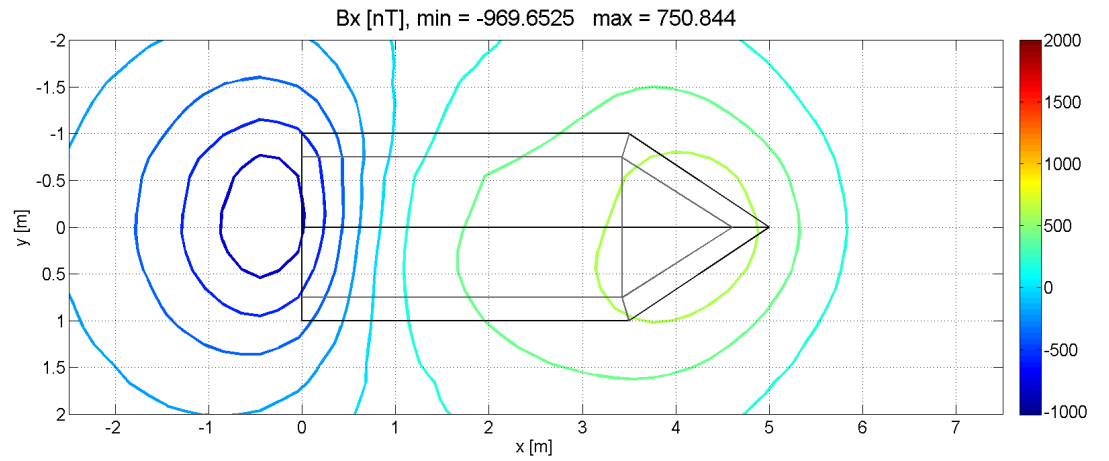
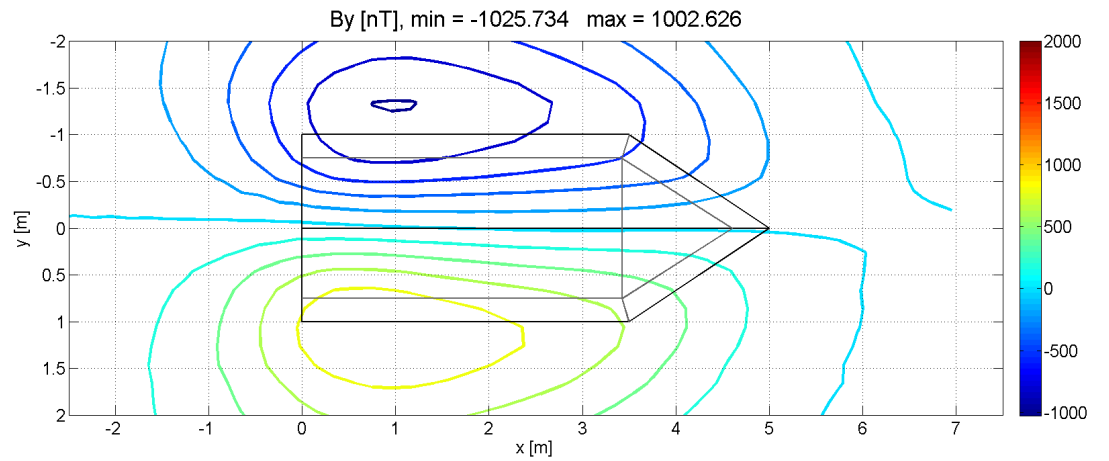


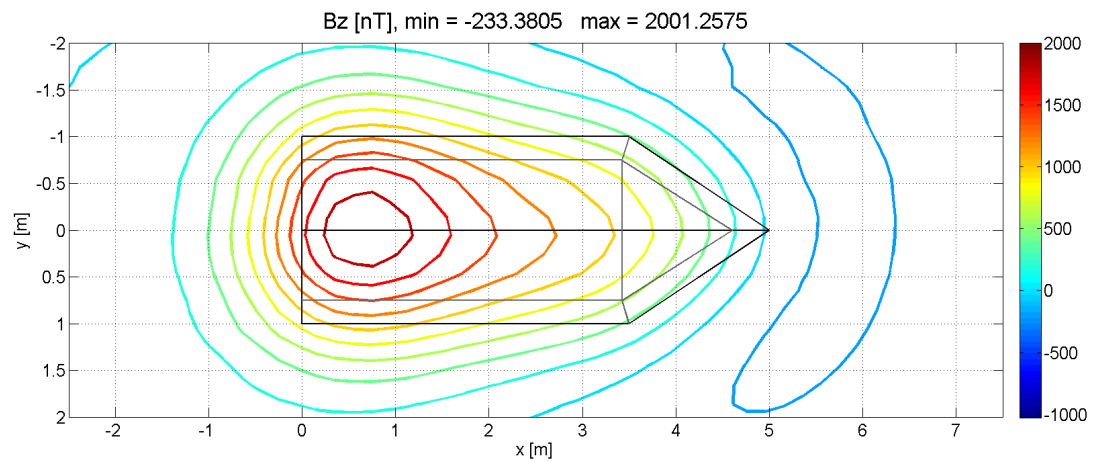
Figure 7.5: Intensity of the magnetic signature of the **M4** at Bünsdorf.



(a) Mean relative error.



(b) Mean relative error.



(c) Mean relative error.

Figure 7.6: Field components of the magnetic signature of the **M4** at Bünsdorf.

### 7.3.1 Demonstration of the prediction model on the measurement data

We end this chapter with the demonstration of the prediction model, applied to the measurements in the local background field at Bünsdorf. We partition the **M4** by Mesh I, and take 138 measurements of the magnetic field inside the mock-up.

The condition number of the matrix  $A$  in the discrete inverse problem is approximately  $\text{cond}(A) \sim 10^5$ , which is relatively low. Due to noisy measurements inside the mock-up (movement of the sensor and positioning errors), we use the SVD method in combination with Tikhonov regularization (where  $L = I$ ) to solve the inverse problem. The source solutions are shown in figure ???. If we look at the source function  $g$ , we see that the magnetic poles of the magnetisation of the **M4** are at the top and bottom of the mock-up. This indicates that the magnetic signature is shaped like a magnetic dipole, pointing in the  $z$ -direction. This is what we expected to see, looking at the measured magnetic signature at one meter below the mock-up, see figure 7.5.

The predicted magnetic signature components are shown in figure 7.9. If we compare figure 7.9 with figure 7.6 we see that there is some agreement between the measured signature and the predicted signature. In particular, we observe that the intensity of both fields do not differ a lot. However the “location” of the predicted signature and the magnetic signature does not agree. This can be explained because at the measurement campaign we did not do an accurate measurement of the location of the **M4** with respect to the array of sensors. Therefore, there is a mismatch in locations.

Note that due some errors in the positioning of the mock-up with respect to the global

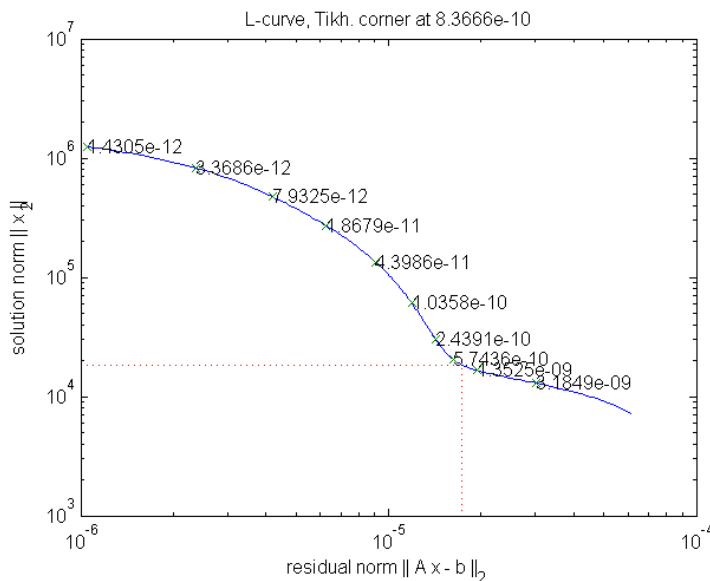


Figure 7.7: The  $L$ -curve that is used to choose the optimal regularization parameter in Tikhonov regularization of the inverse problem.

coordinate system, we cannot use the absolute error and relative error functions. These functions would simply indicate that there is a complete mismatch between the predicted signature and the real signature. This is however not true, as we have observed.

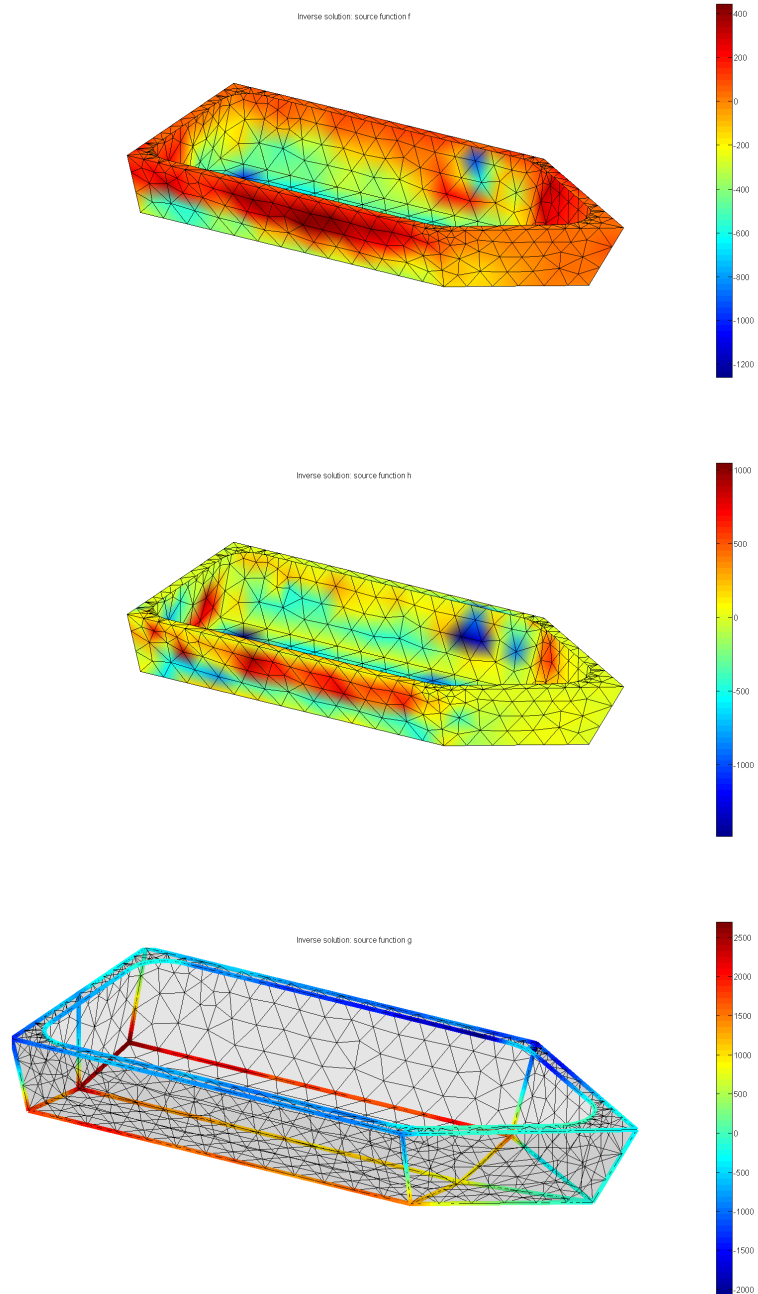
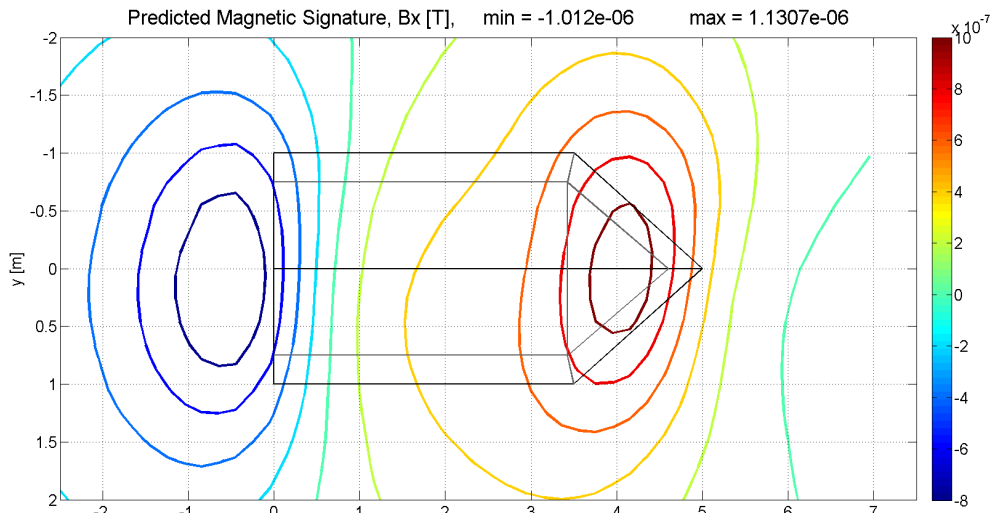
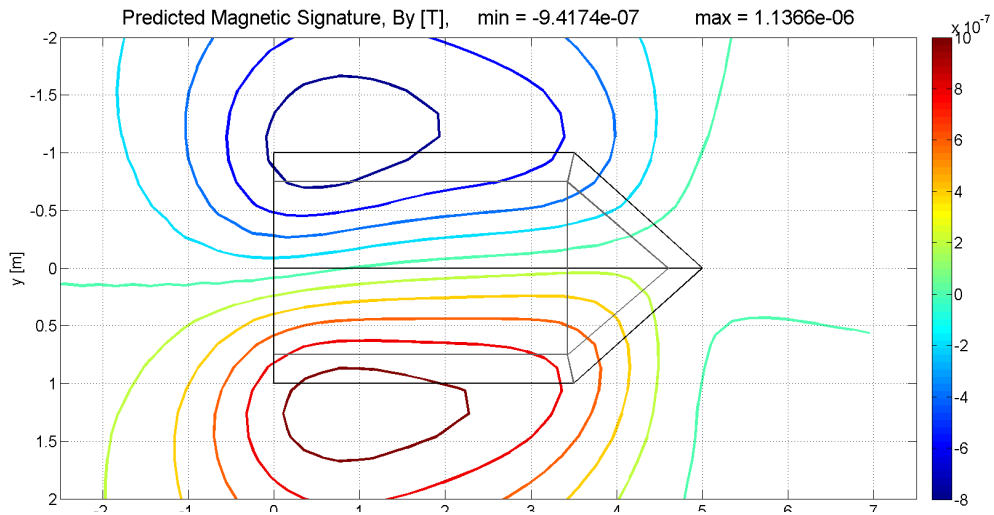


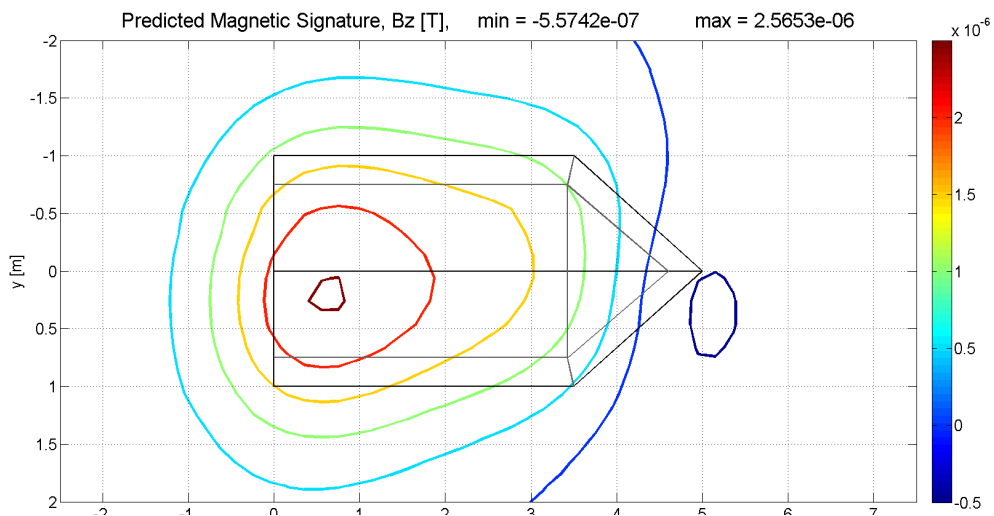
Figure 7.8: The magnetic sources  $f$   $g$  and  $h$  in the **M4**, computed by the inverse problem.



(a) Predicted signature component  $B_x$ .



(b) Predicted signature component  $B_y$ .



(c) Predicted signature component  $B_z$ .

Figure 7.9: Field components of the magnetic signature at Bünsdorf.

## 8 Conclusion and Further Research

### 8.1 Results

In the introduction we defined five research goals:

- Determine a correct formulation of this prediction model.
- Analyze the inverse problem and study regularization methods.
- Use simulated data to investigate whether the model can predict accurately.
- Analyze the influence of noise in the measurement data with respect to the solutions of the inverse problem.
- Apply the prediction model to real on-board measurement data.

In chapters 2-4 we have covered the first two research goals. We have determined a formulation of a prediction model, under suitable assumptions. Furthermore, its behavior and regularization methods have been studied. The correctness of the formulation seems to be justified by numerical experiments. We are confident that the proposed prediction model is able to predict the magnetic signature, based on on-board measurements of the magnetic field.

#### 8.1.1 Performance of the prediction model

In Chapter 7 we have investigated the performance and behavior of the prediction model, based on simulations in COMSOL. We have seen that the prediction model performs well with these simulations of a background field. For the uniform background field  $\mathbf{B}_b = 50 \cdot 10^{-6} \mathbf{u}_x \text{T}$  we have seen that the prediction model (in the absence of noisy measurements) performs very good: the best performance was observed in the numerical test where we neglected the double layer component in the forward and inverse problem formulation. A maximum absolute error  $\varepsilon_{\max}$  of around  $34nT$  and a relative error in the range of  $[0.005, 0.042]$  was obtained. Relatively, this means that the predicted signature is maximally 4 percent off. (In practice, a maximal percentage of 10 percent is acceptable.) However, many on-board measurements (176 measurements) are required to achieve these results.

#### 8.1.2 Reducing the influence of noise in measurements on performance

We also investigated the effect of regularization when we used noisy measurements in the prediction model. We defined a simple noise model and added this noise to the on-board measurements of the signature. The noise vector  $\mathbf{e}$  was modeled as White Gaussian noise, where each of the entries  $e_i$  were independently normally distributed. As a reasonable value for  $\sigma$  we took the value

$$\sigma = \frac{1}{9} \sqrt{3} \cdot 300 \cdot 10^{-9} T$$

This variance is what we expect in practice. In the numerical tests we have seen that regularization often leads to a good performance of the prediction model. When we compare the predicted signatures without noisy measurement to those with noise, we see that regularization reduces the influence of the ill-posedness of the problem significantly.

Note that the proposed background fields were **uniform**. In practice, it may be the case that a background field is not uniform, but has some strong local variations. It remains a question whether the proposed prediction model performs well in such a case. In practice, the field is reasonably uniform. However, the field is not static as the ship moves in the earth's magnetic field.

### 8.1.3 **Demonstration of the prediction model on real measurement data**

In Chapter 7 we have demonstrated the prediction model on real measurement data. It was shown that the prediction of the magnetic signature is in some sense in agreement with the measured magnetic signature. However, due to noisy measurements in the **M4** we argue that this is causing the mismatch between the predicted magnetic signature and the measured magnetic signature. The prediction must be enhanced in such a way that it can deal with such noisy measurements. This will be done in the near future.

## 8.2 Future research

At this point, we would like to present some new research directions and challenges for the near future.

### 8.2.1 Bayesian inference and techniques from Bayesian statistics

In this report we solved the discrete inverse problem  $A\mathbf{x} = \mathbf{y} + \mathbf{e}$  deterministically, by using an approximation of the best-approximate solution

$$\mathbf{x}^\dagger = A^\dagger(\mathbf{y} + \mathbf{e})$$

where  $\mathbf{e}$  is some unknown noise vector. The solution is regularized using Tikhonov regularization and we have seen that this choice lead to a good performance of the prediction model, under the assumption that we knew how the noise was distributed. However, in practice we do not have any access to such descriptions.

Another approach to solving the discrete inverse problem is to solve it in a stochastic way. This can be done by formulating the discrete inverse problem in a so-called *Bayesian inference* problem. In this Bayesian statistical framework, everything that is unknown in a problem is considered as a **random variable**. In the discrete inverse problem  $A\mathbf{x} = \mathbf{y}$  both  $\mathbf{x}$ ,  $\mathbf{y}$  and noise vector  $\mathbf{e}$  are considered unknown a-priori, whereas  $A$  usually is known. The discrete inverse problem can be stochastically extended to  $AX = Y + E$  where  $X$ ,  $Y$  and  $E$  are random variables.

Solving the stochastic extension means that we look for a solution that is *the most probable*, amongst all possible solutions. Suppose that we know the a-priori distribution of  $X$  and the distribution of  $E$ , where the probability density of  $E$  is given by  $\pi$ , and that the random variables  $X$  and  $Y$  are independent. Then, using Bayes formula

$$\pi(x|y) = \frac{\pi(y|x)\pi_{\text{prior}}(x)}{\pi(y)}$$

we can derive the so-called *a posteriori density* of  $X$

$$\pi(x|y) = \frac{\pi(y|x)\pi_{\text{prior}}(x)}{\pi(y)}, \quad y = y_{\text{observed}}$$

In the Bayesian statistical framework, *the a posteriori solution*  $X$  is the solution of the inverse problem  $A\mathbf{x} = \mathbf{y}$ . It can be shown that (under suitable conditions) the most probable solution, also called the *Maximum A Posteriori (MAP) estimator*, given by

$$x_{\text{MAP}} = \arg \max \pi(x|y)$$

corresponds with the least-squares solution of the system  $A\mathbf{x} = \mathbf{y} + \mathbf{e}$ .

Several techniques in the Bayesian statistic framework are known to improve the inverse solution by means of *statistical preconditioners* and *prior-densities*. This means that we can improve the performance of the prediction model, *if we are able to give an accurate description of the solution  $\mathbf{x}$  that we seek*. For example, the physics that

the solution (should) satisfy can be used in formulating an a-priori distribution of  $X$ . Notice the similarity between these a-priori distributions and the notion of Tikhonov regularization. In fact, one can show that, in this Bayesian statistical framework, these two notions are the same.

Lastly, the notion of *Bayesian learning* sounds promising as an enhancement of the prediction model. For an introduction to Bayesian statistics, we refer to [2].

### 8.2.2 Advanced regularization methods

As already noted, the notion of prior densities in the Bayesian framework is closely related to Tikhonov regularization. In this project we look at Tikhonov regularization to regularize solutions of the inverse problem. As we have shown in section 4.4, a Tikhonov regularized solution solves the minimization problem

$$\mathbf{x}_\lambda = \arg \min \{ \|\mathbf{Ax} - \mathbf{b}\|_2^2 + \lambda^2 \|\mathbf{x}\|^2 \}$$

where the parameter  $\lambda$  is chosen in such a way that there is a nice balance between minimizing the residual  $r = \|\mathbf{Ax} - \mathbf{b}\|^2$  and the norm of the vector  $\|\mathbf{x}\|^2$ . We also discussed that the general form of Tikhonov regularization is given by

$$\mathbf{x}_\lambda = \arg \min \{ \|\mathbf{Ax} - \mathbf{b}\|_2^2 + \lambda^2 \|\mathbf{Lx}\|^2 \}$$

where  $L$  is a matrix that contains *a-priori* information about the inverse solutions. In this project we took  $L = I$ , indicating that we try to limit the norm of the inverse solutions that we seek. However, by using more advanced information about the solutions, we may improve the performance of the prediction model. For instance, one could impose a smoothness conditions on the inverse solution. Imposing the existence of a first order derivative can be described by the derivative operator

$$L_1 = \begin{bmatrix} -1 & 1 & & & \\ & & \ddots & \ddots & \\ & & & & -1 & 1 \end{bmatrix}$$

and a second order derivative is described by

$$L_1 = \begin{bmatrix} 1 & -2 & 1 & & \\ & \ddots & \ddots & \ddots & \\ & & & & 1 & -2 & 1 \end{bmatrix}$$

Besides smoothness conditions one could think of other properties that the inverse solutions should satisfy. The absence of any magnetic monopoles, which is formulated in Gauss' law ( $\nabla \cdot \mathbf{B} = 0$ ) leads to the observation that, when we sum up all magnetic sources, the net charge should vanish. For the magnetic source solutions  $f, g$  and  $h$  this implies that

$$\iint_{\Omega} f(\mathbf{r}') d\mathbf{r}' + \iint_{\Omega} h(\mathbf{r}') d\mathbf{r}' + \int_{\partial\Omega} g(\mathbf{r}') d\mathbf{r}' = 0$$

Using a discretization of the object  $\Omega$  leads to the following description for the unknown vector  $\mathbf{p}$

$$R\mathbf{p} = 0$$

Other regularization methods could prove to be useful as well.

### 8.2.3 Inhomogeneity of the background field

In the application of the prediction model (and inverse model), we assumed that the magnetic field in the sensor positions was available. In practice, a measurement consists of the total field of all contributions to the magnetic field, i.e. the combination of the earth's background field, the magnetic field of a naval vessel and noise. The separation of the magnetic field and the other magnetic fields is impossible on a moving vessel. Therefore, the prediction model should be adjusted in such a way that it takes into account this observation.

For instance, the prediction model could be modified in such a way that it “knows” that in each of the on-board measurements, there is some constant value  $\mathbf{B}_{\text{constant}}$ . This constant value should then in turn be present in the predicted magnetic signature as well. At this point it is unclear if this can be modeled into the PDE (see eq 2.1) directly.

### 8.2.4 Use of sensors in magnetic signature monitoring

As we have observed in the measurement campaign, the use of sensors as source for input in the prediction model should be approached with caution. We have seen that small angle changes in the orientation of the sensor have large effects in the actual measurements. We observed that such deviations are in the order of a few  $100nT$ .

On a naval vessel, the movement of a naval vessel induces such changes in the orientation of on-board sensors and therefore these effects are critical for the performance of the prediction model.

### 8.2.5 The magnetic field measured in closed spaces

In the inverse formulation, we use an on-board measurement of the magnetic signature to determine the magnetic sources in the steel. We use the distance between the sensor position and the steel (involved in the geometry) to determine the influence of the magnetization in that steel on the measured field in the sensor. If the distance is large, the magnetic sources in the steel are small.

However, in closed spaces, it could be the case that a measurement by a magnetic sensor cannot be used to predict the magnetic sources in *all* steel plates, but only in some subset. Namely, those steel plates that enclose the space.

It is known that the magnetic field is captured in steel boxes. If this behavior is also present in practice, we should adjust the prediction model. To each on-board mea-

surement, a subset of the geometry should be associated that supports the magnetic sources.

### **8.2.6 Reducing the number of measurements**

In the present prediction model, we need a lot of measurements at sensor positions to compute an accurate prediction of the magnetic signature. However, in practice, we only have a very limited number of magnetic sensors at our disposal (say, around twenty sensors) because magnetic sensors are expensive. To achieve a good prediction of the magnetic signature, additional information about the magnetic signature should be added to the prediction model to achieve a reduction of the number of measurements.

### **8.2.7 Reducing the complexity of the geometry**

The geometry of an actual naval vessel like a frigate is very complex. If we wish to use the geometry in the prediction model, it is of the essence to investigate in what way we can reduce the complexity of the geometry of the ship.

For instance, we can ask ourselves whether it is necessary to model all the steel contributions in the vessel (like engines, and weaponry). Observe that a naval ship also acts like a magnetic shield: it keeps the magnetic sources inside the vessel. Therefore, one could argue that some of the magnetic sources inside are not visible from the outside, and therefore a reduction of the complexity of the geometry can be made.

### **8.2.8 Double layer component**

In section 6.4 we discussed whether the double layer component in our prediction model can be neglected. We compared our predictions with the COMSOL signatures and we observed that the performance of the prediction model increases significantly if we neglect the double layer component. However, we noticed that the formulation of the static magnetic field in COMSOL also neglects a normal component of the field. Therefore, based on COMSOL simulations, we cannot conclude whether this term can be neglected or not.

An experiment should be invented to clarify if this is really the case. One could think of taking a single steel plate with a small thickness (around 4mm) and see how the magnetization varies in different background fields. In particular one should consider a background field that is perpendicular to the steel plate and see how strong the induced magnetic field is, compared to the induced magnetic field by some background field that is oriented tangential to the plate.

## Bibliography

- [1] L. Baratchart, D.P. Hardin, et al. Characterizing kernels of operators related to thin-plate magnetizations via generalizations of hodge decompositions. *IOP-SCIENCE Publishing*, 2013.
- [2] Daniela Calvetti and Erkki Somersalo. *Introduction to Bayesian Scientific Computing*. Springer, 2007.
- [3] Olivier Chadebec, Jean-Louis Coulomb, et al. Modeling of static magnetic anomaly created by iron plates. *IEEE Transactions On Magnetics*, 36(4), 2000.
- [4] Olivier Chadebec, Jean-Louis Coulomb, et al. How to well pose a magnetization identification problem. *IEEE Transactions On Magnetics*, 39(3), 2002.
- [5] Olivier Chadebec, Jean-Louis Coulomb, et al. Recent improvements for solving inverse magnetostatic problem applied to thin shells. *IEEE Transactions On Magnetics*, 38(2), 2002.
- [6] D.A. Dunavant. High degree efficient symmetrical gaussian quadrature rules for the triangle. *Internation Journal for Numerical Methods in Engineering*, 21, 1985.
- [7] H. Engl, M. Hanke, and A. Neubauer. *Regularization of Inverse Problems*. Kluwer Academic Publishers, 2000.
- [8] R. Goldberg. *Methods of Real Analysis*. Wiley, 1976.
- [9] D.J. Griffiths. *Introduction to Electrodynamics*. Pearson Education, 2007.
- [10] Per Christian Hansen. *Discrete Inverse Problems*. SIAM, 2010.
- [11] Per H. Hansen and Dianne P. O'Leary. The use of the *L*-curve in the regularization of discrete ill-posed problems. *SIAM Journal on Scientific Computing*, 14(6), 1993.
- [12] Magnus R. Hestenes and Eduard Stiefel. Methods of conjugate gradients for solving linear systems. *Journal of Research of the National Bureau of Standards*, 49(6), 1952.
- [13] John Holmes. *Exploitation of a Ship's Magnetic Field Signatures*. Morgan & Claypool, 2008.
- [14] John Holmes. *Modeling of Ship's Ferromagnetic Signatures*. Morgan & Claypool, 2008.
- [15] John Holmes. *Reduction of a Ship's Ferromagnetic Signatures*. Morgan & Claypool, 2008.
- [16] John David Jackson. *Classical Electrodynamics*. Wiley, 1999.
- [17] L. Krähenbühl and D. Muller. Thin layers in electrical engineering. example of shell models in analysing eddy-currents by boundary and finite element methods. *IEEE Transactions on magnetics*, 29(2), 1993.
- [18] Rainer Kress. *Linear Integral Equations*. Springer Text, 2010.

- [19] G. Landi. A discrete l-curve for the regularization of ill-posed inverse problems. A discrete L-curve for the regularization of ill-posed inverse problems.
- [20] David C. Lay. *Linear Algebra and its applications*. Pearson, 4th edition edition, 2010.
- [21] E.S.A.M. Lepelaars and D.J. Bekers. Static magnetic signature monitoring, rim-passe 2011 data analysis and development of a phenomenological model for cfav quest. Technical report, TNO, 2013.
- [22] NOAA. Numerical model for earth's magnetic field. <http://www.ngdc.noaa.gov/geomag-web/#igrfwmm>, June 2009.
- [23] A. van der Sluis and H.A. van der Vorst. Sirt- and cg-type methods for the iterative solution of sparse linear least-squares problems. *Elsevier Science Publishing Co*, 1990.
- [24] A.R.P.J. Vijn. Simplified magnetic signature monitoring. Technical report, TNO, 2015.
- [25] C. Vuik and D.J.P. Lahaye. Scientific computing. University Lecture, 2013.
- [26] Y. Vuillermet, Olivier Chadebec, et al. Scalar potential formulation and inverse problem applied to thing magnetic shees. *IEEE Transactions On Magnetics*, 44(6), 2008.

## A Tables

(See next page.)

|             | Mesh | $\varepsilon_{max}$ [nT] | $\tau_{min}$ | $\tau_{max}$ |
|-------------|------|--------------------------|--------------|--------------|
| Solver: SVD | I    | 7408                     | 0.170        | 5.407        |
|             | II   | 8246                     | 0.510        | 8.340        |
|             | III  | -                        | -            | -            |
|             | IV   | -                        | -            | -            |
|             | V    | -                        | -            | -            |
|             | VI   | -                        | -            | -            |

|                   | Mesh | $\varepsilon_{max}$ [nT] | $\tau_{min}$ | $\tau_{max}$ |
|-------------------|------|--------------------------|--------------|--------------|
| Solver: SVD+Tikh. | I    | 232                      | 0.005        | 0.108        |
|                   | II   | 162                      | 0.013        | 0.114        |
|                   | III  | 173                      | 0.007        | 0.091        |
|                   | IV   | 88                       | 0.004        | 0.082        |
|                   | V    | 124                      | 0.007        | 0.088        |
|                   | VI   | 161                      | 0.024        | 0.106        |

|            | Mesh | $\varepsilon_{max}$ [nT] | $\tau_{min}$ | $\tau_{max}$ |
|------------|------|--------------------------|--------------|--------------|
| Solver: QR | I    | 7397                     | 0.169        | 5.376        |
|            | II   | 8159                     | 0.540        | 8.290        |
|            | III  | -                        | -            | -            |
|            | IV   | -                        | -            | -            |
|            | V    | -                        | -            | -            |
|            | VI   | -                        | -            | -            |

|              | Mesh | $\varepsilon_{max}$ [nT] | $\tau_{min}$ | $\tau_{max}$ |
|--------------|------|--------------------------|--------------|--------------|
| Solver: CGLS | I    | 208                      | 0.004        | 0.097        |
|              | II   | 176                      | 0.012        | 0.103        |
|              | III  | 152                      | 0.009        | 0.093        |
|              | IV   | 71                       | 0.003        | 0.054        |
|              | V    | 126                      | 0.007        | 0.088        |
|              | VI   | 150                      | 0.007        | 0.087        |

Table A.1: Results based on 176 measurements inside the **M4** for four different methods. The iterative method CGLS and the application of Tikhonov Regularization in the SVD solver both lead to good predictions of the magnetic signature for this sensor configuration.

| $n$ | $\sigma_n$ | $\langle \mathbf{b}_e, \mathbf{u}_i \rangle$ | $\langle \mathbf{b}_e, \mathbf{u}_i \rangle / \sigma_i$ |
|-----|------------|--|---|
| 1   | 1.05e-08   | -9.65e-06                                    | -9.18e+02   |
| 2   | 8.89e-09   | -3.09e-05                                    | -3.48e+03   |
| 3   | 8.44e-09   | 2.73e-06                                     | 3.23e+02  |
| 4   | 8.16e-09   | -1.02e-06                                    | -1.24e+02   |
| 5   | 7.45e-09   | 8.89e-07                                     | 1.19e+02  |
| 6   | 7.13e-09   | 2.31e-07                                     | 3.24e+01  |
| 7   | 6.85e-09   | 4.32e-06                                     | 6.30e+02  |
| 8   | 6.55e-09   | 2.72e-06                                     | 4.16e+02  |
| 9   | 6.40e-09   | 2.89e-06                                     | 4.52e+02  |
| 491 | 1.47e-13   | -9.34e-09                                    | -6.35e+04   |
| 492 | 1.44e-13   | -4.12e-09                                    | -2.85e+04   |
| 493 | 1.37e-13   | 1.32e-09                                     | 9.64e+03  |
| 494 | 1.26e-13   | 1.57e-08                                     | 1.25e+05  |
| 495 | 1.20e-13   | 3.56e-09                                     | 2.97e+04  |
| 496 | 1.13e-13   | 1.00e-08                                     | 8.86e+04  |
| 497 | 1.07e-13   | -1.06e-08                                    | -9.95e+04   |
| 498 | 1.00e-13   | -4.62e-09                                    | -4.61e+04   |
| 518 | 1.08e-14   | -2.64e-09                                    | -2.44e+05   |
| 519 | 1.04e-14   | -2.12e-09                                    | -2.03e+05   |
| 520 | 8.41e-15   | -3.73e-09                                    | -4.43e+05   |
| 521 | 5.65e-15   | 2.36e-09                                     | 4.19e+05  |
| 522 | 4.93e-15   | -2.57e-09                                    | -5.20e+05   |
| 523 | 6.29e-25   | 7.78e-21                                     | 1.24e+04  |
| 524 | 6.29e-25   | 5.93e-21                                     | 9.43e+03  |
| 525 | 6.29e-25   | -3.28e-21                                    | -5.22e+03   |
| 526 | 6.29e-25   | 2.12e-22                                     | 3.37e+02  |
| 527 | 6.29e-25   | 1.91e-21                                     | 3.03e+03  |
| 528 | 6.29e-25   | 1.28e-20                                     | 2.04e+04  |

Table A.2: Selection of the singular values and the corresponding SVD components of the inverse problem. Mesh VI has been used and 176 measurements of the field to set up the inverse problem. The first column shows the singular values, in decreasing order. The second column are the corresponding SVD components.



## B Fundamental Solution of the Laplace Equation

### B.1 Introduction

Consider the general Laplace's equation in  $\mathbb{R}^n$  given by

$$\Delta u = 0, \quad \mathbf{x} \in \mathbb{R}^3$$

where  $\Delta$  is defined as the Laplacian operator

$$\Delta = \frac{\partial^2}{\partial x_1^2} + \frac{\partial^2}{\partial x_2^2} + \frac{\partial^2}{\partial x_3^2}$$

Any function satisfying this equation is called *harmonic*. It is easy to see that many functions satisfy this condition: every constant and linear function automatically satisfies this condition due to the vanishing character under taking the derivative twice.

In this appendix we derive the fundamental solution  $\Phi$  that satisfies

$$\Delta \Phi = \delta_0$$

The fundamental solution serves as a building block for the non-homogeneous version of the Laplace's equation called the *Poisson's equation*

$$\Delta u = f, \quad \mathbf{x} \in \mathbb{R}^3$$

Here,  $f \in C_c^2(\mathbb{R}^3)$  is a twice continuous differentiable function with compact support, i.e., the set

$$\{\mathbf{x} \in \mathbb{R}^n : f(\mathbf{x}) \neq 0\}$$

has compact closure. One can prove that, under the above assumptions, the solution of this partial differential equation is given by the convolution of the fundamental solution  $\Phi$  with  $f$ :

$$v(\mathbf{x}) \equiv \int_{\mathbb{R}^n} \Phi(\mathbf{x} - \mathbf{y}) f(\mathbf{y}) d\mathbf{y}$$

Given the symmetric behavior of the Laplace's equation, we are looking for solutions that exhibit this property. Therefore we are looking for a radial solution, i.e., a harmonic function on  $\mathbb{R}^3$  such that  $u(\mathbf{x}) = v(|\mathbf{x}|)$  (symmetric in  $|\mathbf{x}|$ ).

### B.2 Computation of the fundamental solution

We start by transforming the PDE into an ODE in the following way. Observe that whenever  $|\mathbf{x}| \neq 0$  then

$$u_{x_i} := \frac{\partial u}{\partial x_i} = \frac{x_i}{|\mathbf{x}|} v'(|\mathbf{x}|)$$

for each  $i = 1, 2, 3$ . Taking the second derivatives then leads to (for  $|\mathbf{x}| \neq 0$ )

$$u_{x_i x_i} = \frac{1}{|\mathbf{x}|} v'(|\mathbf{x}|) - \frac{x_i^2}{|\mathbf{x}|^3} v'(|\mathbf{x}|) + \frac{x_i^2}{|\mathbf{x}|^2} v''(|\mathbf{x}|)$$

Substitution of these expressions for  $u_{x_i x_i}$  into the Laplace operator  $\Delta$  leads to the following simple form:

$$\Delta u = \frac{2}{|\mathbf{x}|} v'(|\mathbf{x}|) + v''(|\mathbf{x}|)$$

Because we are looking for a radial function we set  $r = |\mathbf{x}|$ . So a radial solution  $v$  satisfies Laplace's equation if and only if it satisfies the following ordinary differential equation:

$$\frac{2}{r} v'(r) + v''(r) = 0$$

Solving leads to the following expression for  $v$ :

$$v(r) = \frac{A}{r} + B, \quad \text{so } v(x) = \frac{A}{|\mathbf{x}|} + B$$

where  $A$  and  $B$  are any real constants. The constant  $B$  is set to be zero, as the potential vanishes at infinity. Now let  $B_R(0)$  be the sphere of radius  $R$  centered at the origin. Then

$$1 = \iiint_{B_R(0)} \Delta v(x) dx = \iint_{\partial B_R(0)} \nabla v(x) \cdot dS = 4\pi R^2 \left. \frac{\partial v}{\partial r} \right|_{r=R} = -4\pi A$$

Taking  $A = \frac{1}{4\pi}$  leads to the following fundamental solution for the Laplace equation in three dimensions:

$$\Phi(\mathbf{x}) = -\frac{1}{4\pi} \frac{1}{|\mathbf{x}|}$$

## C Double layer potential

In this appendix we discuss a classical result in the field of potential theory. For steel object we assume that the magnetization is tangential to the surface of the object. This assumption works fine when solving the “forward problem” for steel thin shells, i.e., given some background field  $\mathbf{H}_b$ , determine the reduced magnetic field caused by the induced magnetization in  $S$ . This assumption can be found in many engineering applications and is called *magnetic shielding*.

However, in reality a magnetization of a steel thin shell is not entirely tangential to the shell even though the thickness of the shell is small; there exists some orthogonal component  $\mathbf{M}^\perp := \mathbf{M} \cdot \mathbf{n}'$  (where  $\mathbf{n}'$ ) is the normal vector to the surface  $S$ . This component also induces a potential that is called a *double layer potential*.

From potential theory we can derive an expression that can describe these contributions in terms of a scalar magnetic source density distribution on the surface of the thin shell. This is done in the first section of this appendix. Then, we apply a Symmetric Gaussian Quadrature rule to derive an expression of the magnetic induction field caused by this double layer potential. We end with a physical interpretation of the double layer potential.

### C.1 Further derivation of the potential expression of the Poisson problem

As described in Chapter 4 the forward problem consists of solving Poisson’s problem

$$\Delta\varphi = \nabla \cdot \mathbf{M}$$

where  $\nabla \cdot \mathbf{M}$  can be interpreted as the source of the potential  $\varphi$ . Let us consider for now the Poisson problem for some single steel plate  $\Omega$  with dimensions  $l, w$  and  $t$  (where  $t$  is relatively small compared to the length and width of the plate) and let  $\mathbf{M}$  be some magnetization of  $\Omega$ . We place the steel plate in such a way that the centroid of the plate coincide with the origin of the  $(x, y, z)$ -system, where  $z$  is pointing upwards.

The analytical solution of this problem can be formulated in terms of a fundamental solution ([16], page 176-177):

$$\varphi(\mathbf{r}) = \underbrace{\frac{-1}{4\pi} \iiint_{\Omega} \frac{1}{|\mathbf{r} - \mathbf{r}'|} \nabla \cdot \mathbf{M}(\mathbf{r}') d\mathbf{r}'}_{(1a)} + \underbrace{\frac{1}{4\pi} \iint_{\partial\Omega} \frac{1}{|\mathbf{r} - \mathbf{r}'|} \mathbf{n}' \cdot \mathbf{M}(\mathbf{r}') d\mathbf{r}'}_{(1b)} \quad (1)$$

Here, the normal vector  $\mathbf{n}'$  is pointing outwards, (1a) is the potential caused by the divergence of  $\mathbf{M}$  in the interior of the plate that represents magnetic anomalies in the

plate. The second term (1b) is the effective magnetic surface charge  $\sigma_M = \mathbf{n}' \cdot \mathbf{M}$  at the surface of the plate. This surface charge exists as the magnetization suddenly vanishes outside the plate (note that the magnetization is zero outside the plate!). Therefore, there is a discontinuity of the magnetization at the surface of the plate, that creates  $\sigma_M$ .

We take a look at (1b). Define the sets (see figure C.1)

$$\begin{aligned}\partial\Omega_1 &= \left\{ \mathbf{v} \in \Omega : [\mathbf{v}]_z = \pm \frac{t}{2} \right\} = \partial\Omega_1^+ \cup \partial\Omega_1^- \\ \partial\Omega_2 &= \left\{ \mathbf{v} \in \Omega : [\mathbf{v}]_x = \pm \frac{l}{2} \vee [\mathbf{v}]_y = \pm \frac{w}{2} \right\}\end{aligned}$$

By splitting the boundary of the plate into the two regions  $\partial\Omega_1$  and  $\partial\Omega_2$  we write (1b) as

$$(1b) := \underbrace{\frac{1}{4\pi} \iint_{\partial\Omega_1} \frac{1}{|\mathbf{r} - \mathbf{r}'|} \mathbf{n}' \cdot \mathbf{M}(\mathbf{r}') d\mathbf{r}'}_{(2a)} + \underbrace{\frac{1}{4\pi} \iint_{\partial\Omega_2} \frac{1}{|\mathbf{r} - \mathbf{r}'|} \mathbf{n}' \cdot \mathbf{M}(\mathbf{r}') d\mathbf{r}'}_{(2b)} \quad (2)$$

Let  $\Omega'$  be the two-dimensional projection of  $\Omega$  onto the  $(x, y)$ -plane (a rectangular domain in the  $(x, y)$ -plane of dimensions  $l$  and  $w$  as seen in figure C.2) with a one-dimensional boundary  $\partial\Omega'$ . We assume that the magnetization is uniform in  $t$ . Then (2b) is simplified to

$$(2b) := \frac{t}{4\pi} \int_{\partial\Omega'} \frac{1}{|\mathbf{r} - \mathbf{r}'|} \mathbf{n}' \cdot \mathbf{M}(\mathbf{r}') d\mathbf{r}'$$

On the boundary  $\partial\Omega_1$  it holds that

$$(\mathbf{n}' \cdot \mathbf{M})(z' = -t/2) = -(\mathbf{n}' \cdot \mathbf{M})(z' = t/2)$$

(so the magnetic surface charge is equal up to a sign). Define  $M_z = \mathbf{n}' \cdot \mathbf{M}$  on  $\partial\Omega_1$ .

Then

$$\begin{aligned}\frac{1}{4\pi} \iint_{\partial\Omega_1} \frac{1}{|\mathbf{r} - \mathbf{r}'|} \mathbf{n}' \cdot \mathbf{M}(\mathbf{r}') d\mathbf{r}' &= \frac{1}{4\pi} \iint_{\partial\Omega_1^+} \frac{M_z(x', y')}{|\mathbf{r} - \mathbf{r}'(z' = \frac{t}{2})|} d\mathbf{r}' + \frac{1}{4\pi} \iint_{\partial\Omega_1^-} \frac{-M_z(x', y')}{|\mathbf{r} - \mathbf{r}'(z' = -\frac{t}{2})|} d\mathbf{r}' \\ &= \frac{1}{4\pi} \iint_{\Omega'} M_z(x', y') \cdot \left[ \frac{1}{|\mathbf{r} - \mathbf{r}'(z' = \frac{t}{2})|} - \frac{1}{|\mathbf{r} - \mathbf{r}'(z' = -\frac{t}{2})|} \right] dx' dy'\end{aligned}$$

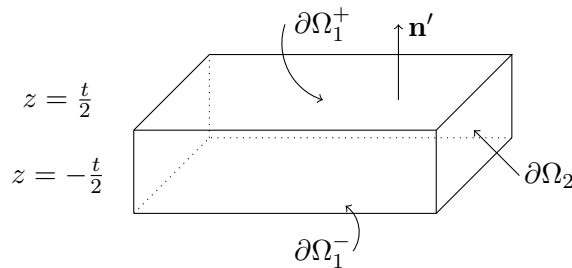


Figure C.1: Boundaries  $\partial\Omega_1$  and  $\partial\Omega_2$  of the plate.

Observe as  $t$  is small

$$\left[ \frac{1}{|\mathbf{r} - \mathbf{r}'(z' = \frac{t}{2})|} - \frac{1}{|\mathbf{r} - \mathbf{r}'(z' = -\frac{t}{2})|} \right] \approx t \frac{\partial}{\partial \nu'} \left( \frac{1}{|\mathbf{r} - \mathbf{r}'|} \right)$$

where

$$\frac{\partial}{\partial \nu'} := \mathbf{n} \cdot \nabla'$$

Bringing all the pieces together leads to the following expressions for the potential  $\varphi$

$$\begin{aligned} \varphi(\mathbf{r}) = & -\frac{t}{4\pi} \iint_{\Omega'} \frac{1}{|\mathbf{r} - \mathbf{r}'|} (\nabla \cdot \mathbf{M})(\mathbf{r}') d\mathbf{r}' + \frac{t}{4\pi} \iint_{\partial\Omega'} \frac{1}{|\mathbf{r} - \mathbf{r}'|} \mathbf{n}' \cdot \mathbf{M}(\mathbf{r}') d\mathbf{r}' \\ & + \frac{t}{4\pi} \iint_{\Omega'} \frac{\partial}{\partial \nu'} \left( \frac{1}{|\mathbf{r} - \mathbf{r}'|} \right) (\mathbf{n}' \cdot \mathbf{M})(\mathbf{r}') d\mathbf{r}' \end{aligned}$$

The potential consists of a term that represents the tangential component of the potential (along  $\Omega$ ) and a perpendicular component to  $\Omega$ . The perpendicular component is called a *double layer potential*. We write for the tangential component

$$\varphi^{\parallel}(\mathbf{r}) = \frac{t}{4\pi} \iint_{\Omega'} \frac{1}{|\mathbf{r} - \mathbf{r}'|} (\nabla \cdot \mathbf{M})(\mathbf{r}') d\mathbf{r}' + \frac{t}{4\pi} \iint_{\partial\Omega'} \frac{1}{|\mathbf{r} - \mathbf{r}'|} \mathbf{n}' \cdot \mathbf{M}(\mathbf{r}') d\mathbf{r}'$$

and for the double layer potential we have

$$\varphi^{\perp}(\mathbf{r}) = \frac{t}{4\pi} \iint_{\Omega'} \frac{\partial}{\partial \nu'} \left( \frac{1}{|\mathbf{r} - \mathbf{r}'|} \right) (\mathbf{n}' \cdot \mathbf{M})(\mathbf{r}') d\mathbf{r}'$$

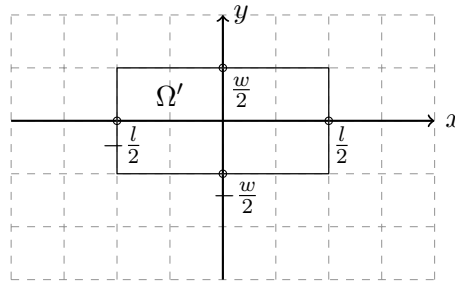


Figure C.2: The projection of  $\Omega$  onto the  $x, y$ -axis leads to a two-dimensional plate with an one-dimensional boundary.

## C.2 Approximation of the double layer expression for $\mathbf{B}^{\perp}$

In the previous section we obtained an expression for the double layer potential:

$$\varphi^{\perp}(\mathbf{r}) = \frac{t}{4\pi} \iint_{\Omega'} \frac{\partial}{\partial \nu'} \left( \frac{1}{|\mathbf{r} - \mathbf{r}'|} \right) (\mathbf{n}' \cdot \mathbf{M})(\mathbf{r}') d\mathbf{r}'$$

The magnetic induction field  $\mathbf{B}^{\perp}$  that is induced by this potential is given by

$$\mathbf{B}^{\perp}(\mathbf{r}) = \frac{\mu_0 t}{4\pi} \iint_{\Omega'} \frac{\partial}{\partial \nu'} \left( \frac{\mathbf{r} - \mathbf{r}'}{|\mathbf{r} - \mathbf{r}'|^3} \right) \sigma(\mathbf{r}') d\mathbf{r}'$$

Here we have used the constitutive relation  $\mathbf{B} = \mu_0 \mathbf{H} = \mu_0 \nabla \varphi$ , which is true outside the object  $\Omega$ . Note that

$$\frac{\partial}{\partial \mathbf{r}'} \equiv \mathbf{n}' \cdot \nabla' = n_{x'} \frac{\partial}{\partial x'} + n_{y'} \frac{\partial}{\partial y'} + n_{z'} \frac{\partial}{\partial z'}, \quad \text{at some point } \mathbf{r}' \in \Omega'$$

where  $\mathbf{n}' = (n_{x'}, n_{y'}, n_{z'})^T$  is depending on  $\mathbf{r}'$ . So the magnetic induction field  $\mathbf{B}^\perp$  can be written as

$$\begin{aligned} \mathbf{B}^\perp(\mathbf{r}) &= \frac{\mu_0 t}{4\pi} \iint_{\Omega'} \left[ n_{x'} \frac{\partial}{\partial x'} + n_{y'} \frac{\partial}{\partial y'} + n_{z'} \frac{\partial}{\partial z'} \right] \left( \frac{\mathbf{r} - \mathbf{r}'}{|\mathbf{r} - \mathbf{r}'|^3} \right) \sigma(\mathbf{r}') d\mathbf{r}' \\ &= \frac{\mu_0 t}{4\pi} \iint_{\Omega'} n_{x'} \frac{\partial}{\partial x'} \left( \frac{\mathbf{r} - \mathbf{r}'}{|\mathbf{r} - \mathbf{r}'|^3} \right) \sigma(\mathbf{r}') d\mathbf{r}' + \frac{\mu_0 t}{4\pi} \iint_{\Omega'} n_{y'} \frac{\partial}{\partial y'} \left( \frac{\mathbf{r} - \mathbf{r}'}{|\mathbf{r} - \mathbf{r}'|^3} \right) \sigma(\mathbf{r}') d\mathbf{r}' \\ &\quad + \frac{\mu_0 t}{4\pi} \iint_{\Omega'} n_{z'} \frac{\partial}{\partial z'} \left( \frac{\mathbf{r} - \mathbf{r}'}{|\mathbf{r} - \mathbf{r}'|^3} \right) \sigma(\mathbf{r}') d\mathbf{r}' \\ &\equiv \mathbf{B}_x^\perp + \mathbf{B}_y^\perp + \mathbf{B}_z^\perp \end{aligned}$$

For each of the component  $\mathbf{B}_x^\perp$ ,  $\mathbf{B}_y^\perp$  and  $\mathbf{B}_z^\perp$  we derive an expression. First we start by simplifying the expression for  $\mathbf{B}_x^\perp$ . A direct computation shows that

$$\begin{aligned} \frac{\partial}{\partial x'} \left( \frac{\mathbf{r} - \mathbf{r}'}{|\mathbf{r} - \mathbf{r}'|^3} \right) &= \frac{-1}{|\mathbf{r} - \mathbf{r}'|^3} \mathbf{e}_1 + \frac{\partial}{\partial x'} \left( \frac{1}{|\mathbf{r} - \mathbf{r}'|^3} \right) (\mathbf{r} - \mathbf{r}') \\ &= \frac{-1}{|\mathbf{r} - \mathbf{r}'|^3} \mathbf{e}_1 + 3 \frac{x - x'}{|\mathbf{r} - \mathbf{r}'|^5} (\mathbf{r} - \mathbf{r}') \end{aligned}$$

Hence we can rewrite  $\mathbf{B}_x^\perp$  as

$$\mathbf{B}_x^\perp(\mathbf{r}) = \frac{\mu_0 t}{4\pi} \iint_{\Omega'} n_{x'} \frac{-1}{|\mathbf{r} - \mathbf{r}'|^3} \mathbf{e}_1 \sigma(\mathbf{r}') d\mathbf{r}' + \frac{3\mu_0 t}{4\pi} \iint_{\Omega'} n_{x'} (x - x') \frac{\mathbf{r} - \mathbf{r}'}{|\mathbf{r} - \mathbf{r}'|^5} \sigma(\mathbf{r}') d\mathbf{r}'$$

Similar, for  $\mathbf{B}_y^\perp$  and  $\mathbf{B}_z^\perp$  we have

$$\begin{aligned} \mathbf{B}_y^\perp(\mathbf{r}) &= \frac{\mu_0 t}{4\pi} \iint_{\Omega'} n_{y'} \frac{-1}{|\mathbf{r} - \mathbf{r}'|^3} \mathbf{e}_2 \sigma(\mathbf{r}') d\mathbf{r}' + \frac{3\mu_0 t}{4\pi} \iint_{\Omega'} n_{y'} (y - y') \frac{\mathbf{r} - \mathbf{r}'}{|\mathbf{r} - \mathbf{r}'|^5} \sigma(\mathbf{r}') d\mathbf{r}' \\ \mathbf{B}_z^\perp(\mathbf{r}) &= \frac{\mu_0 t}{4\pi} \iint_{\Omega'} n_{z'} \frac{-1}{|\mathbf{r} - \mathbf{r}'|^3} \mathbf{e}_3 \sigma(\mathbf{r}') d\mathbf{r}' + \frac{3\mu_0 t}{4\pi} \iint_{\Omega'} n_{z'} (z - z') \frac{\mathbf{r} - \mathbf{r}'}{|\mathbf{r} - \mathbf{r}'|^5} \sigma(\mathbf{r}') d\mathbf{r}' \end{aligned}$$

The expression of the magnetic induction field  $\mathbf{B}^\perp$  can now be simplified to the following form:

$$\mathbf{B}^\perp(\mathbf{r}) = -\frac{\mu_0 t}{4\pi} \iint_{\Omega'} \frac{\mathbf{n}(\mathbf{r}')}{|\mathbf{r} - \mathbf{r}'|^3} \sigma(\mathbf{r}') d\mathbf{r}' + \frac{3\mu_0 t}{4\pi} \iint_{\Omega'} \mathbf{n}(\mathbf{r}') \cdot (\mathbf{r} - \mathbf{r}') \frac{\mathbf{r} - \mathbf{r}'}{|\mathbf{r} - \mathbf{r}'|^5} \sigma(\mathbf{r}') d\mathbf{r}'$$

Now we mesh the surface  $\Omega'$  into triangular elements  $(\mathbf{e}_i)_{i=1}^T$ . On each triangular element  $\mathbf{e}_i$  we have that  $\mathbf{n}$  is a constant vector. So

$$\mathbf{B}^\perp(\mathbf{r}) = -\frac{\mu_0 t}{4\pi} \sum_{i=1}^T \mathbf{n}_i \iint_{\mathbf{e}_i} \frac{1}{|\mathbf{r} - \mathbf{r}'|^3} \sigma(\mathbf{r}') d\mathbf{r}' + \frac{3\mu_0 t}{4\pi} \sum_{i=1}^T \iint_{\mathbf{e}_i} \mathbf{n}_i \cdot (\mathbf{r} - \mathbf{r}') \frac{\mathbf{r} - \mathbf{r}'}{|\mathbf{r} - \mathbf{r}'|^5} \sigma(\mathbf{r}') d\mathbf{r}'$$

On each of the integrals we can approximate the value of the integral by applying a symmetrical quadrature rule for triangles. In general we have the following approxi-

mation of the  $\mathbf{B}^\perp$ -field:

$$\begin{aligned} \mathbf{B}^\perp(\mathbf{r}) \approx & -\frac{\mu_0 t}{4\pi} \sum_{i=1}^T \left( |e_i| \sum_{k=1}^{n_g} w_k \frac{1}{|\mathbf{r} - \mathbf{r}'(s_k, t_k)|^3} \sigma(\mathbf{r}'(s_k, t_k)) \right) \mathbf{n}_i \\ & + \frac{3\mu_0 t}{4\pi} \sum_{i=1}^T |e_i| \sum_{k=1}^{n_g} w_k \mathbf{n}_i \cdot (\mathbf{r} - \mathbf{r}'(s_k, t_k)) \frac{\mathbf{r} - \mathbf{r}'(s_k, t_k)}{|\mathbf{r} - \mathbf{r}'(s_k, t_k)|^5} \sigma(\mathbf{r}'(s_k, t_k)) \end{aligned}$$

### C.3 Interpretation of the double layer potential

Consider a single plate  $\Omega$  with thickness  $t > 0$ . Such a steel plate has two parallel surfaces  $S_1$  and  $S_2$ . For given surface  $S_1$  the second surface  $S_2$  is described by

$$S_2 = \{y + t\nu(y) : y \in S_1\}$$

where  $\nu(y)$  is the normal vector in the point  $y \in S_1$  that points towards the surface  $S_2$ . For now, we only consider these two surfaces as two disconnected objects and not as part of the steel plate.

Suppose we have a magnetic charge distribution on the surface  $S_1$  in  $\mathbb{R}^3$  such that the magnetic charge distribution is given by  $\frac{\sigma}{t}$ . Furthermore, suppose that a magnetic charge distribution on the surface  $S_2$  is given by  $-\frac{\sigma}{t}$ . See also figure C.3. The magnetic field  $\mathbf{H}^\perp$  at point  $\mathbf{r} \in \mathbb{R}^3$  generated by these magnetic charges (the jumps in the magnetic charges give rise to such a potential) is given by  $\mathbf{H}^\perp = -\nabla\varphi^\perp$ , where  $\varphi^\perp$  is the associated potential which is given by the following description:

$$\varphi^\perp(\mathbf{r}) = -\frac{1}{4\pi} \iint_{S_1} \left[ \frac{1}{|\mathbf{r} - (\mathbf{r}' + t\nu'(\mathbf{r}'))|} - \frac{1}{|\mathbf{r} - \mathbf{r}'|} \right] \frac{\sigma(\mathbf{r}')}{t} d\mathbf{r}'$$

For the limit  $t \downarrow 0$  we have that

$$\left[ \frac{1}{|\mathbf{r} - (\mathbf{r}' + t\nu'(\mathbf{r}'))|} - \frac{1}{|\mathbf{r} - \mathbf{r}'|} \right] \frac{1}{t} \rightarrow \frac{\partial}{\partial \nu'} \left( \frac{1}{|\mathbf{r} - \mathbf{r}'|} \right)$$

So for thin plates the magnetic surface charge  $\sigma$  of some surface  $S$  induces some magnetic field  $\mathbf{H}^\perp$  which is generated by the potential  $\varphi^\perp$  given by

$$\varphi^\perp(\mathbf{r}) = -\frac{1}{4\pi} \iint_S \frac{\partial}{\partial \nu'} \left( \frac{1}{|\mathbf{r} - \mathbf{r}'|} \right) \sigma(\mathbf{r}') d\mathbf{r}'$$

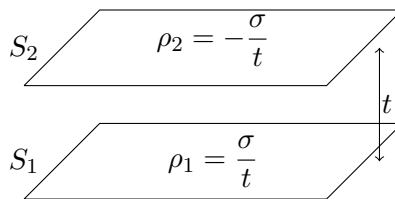


Figure C.3: Two parallel surface  $S_1$  and  $S_2$  with magnetic charge densities  $\rho_1$  and  $\rho_2$ .



## D Quadrature Rules

In this appendix we define the quadrature rules that are used in the derivation of the linear inverse problem. Furthermore the quadrature rules are used in the approximation of the analytical expression of the solution in the forward problem. The first two sections consist of derivations of the quadrature rules for generic triangular elements and line boundary elements. The third section consist of tables of specific quadrature rules used in the implementation of the inverse and forward problem.

### D.1 Quadrature rules for generic triangular elements

Let  $e$  be a triangular element in  $\mathbb{R}^3$  with nodal points  $\mathbf{v}_1, \mathbf{v}_2$  and  $\mathbf{v}_3$ . For further symbolic manipulations we write  $\mathbf{v}_i = (x_i, y_i, z_i)^T$  for  $i = 1, 2$  and  $3$ . We derive a quadrature rule for the integral

$$\iint_e f(\mathbf{r}) d\mathbf{r}$$

where  $f$  is any vector-valued function  $f : \mathbb{R}^3 \rightarrow \mathbb{R}^3$  defined on  $e$ . To derive such a quadrature rule we will use the known symmetric Gaussian quadrature rules defined on the reference triangle  $T_r$  in  $\mathbb{R}^2$ . (Here, the reference triangle  $T_r$  is the triangle in  $\mathbb{R}^2$  with nodal points  $(0, 0)$ ,  $(1, 0)$  and  $(0, 1)$ .) These rules can for example be found in [6]. See figure D.1.

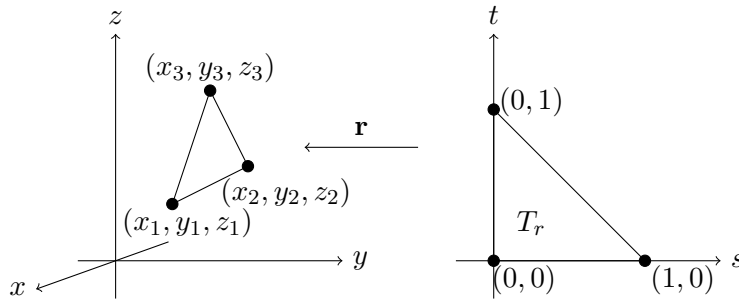


Figure D.1: Triangle transformation

We start by defining a suitable transformation that transforms the above surface integral into a surface integral over two dimensional triangular surface  $T_r$ . More specific, let  $\mathbf{r} : T_r \rightarrow e$  be the transformation that sends point  $(s, t) \in \mathbb{R}^2$  to point  $\mathbf{r} \in \mathbb{R}^3$ :

$$\mathbf{r}(s, t) = \begin{pmatrix} x_1 + (x_2 - x_1)s + (x_3 - x_1)t \\ y_1 + (y_2 - y_1)s + (y_3 - y_1)t \\ z_1 + (z_2 - z_1)s + (z_3 - z_1)t \end{pmatrix} = \mathbf{v}_1 + (\mathbf{v}_2 - \mathbf{v}_1)s + (\mathbf{v}_3 - \mathbf{v}_1)t$$

Observe that  $\mathbf{r}$  is bijective and continuous differentiable. Using that

$$\mathbf{X}_s = \frac{\partial \mathbf{r}}{\partial s} = \mathbf{v}_2 - \mathbf{v}_1, \quad \mathbf{X}_t = \frac{\partial \mathbf{r}}{\partial t} = \mathbf{v}_3 - \mathbf{v}_1$$

we can derive the following integral transformation:

$$\begin{aligned} \iint_e f(\mathbf{r}) d\mathbf{r} &= \iint_{T_r} f(\mathbf{r}(s, t)) |\mathbf{X}_s \times \mathbf{X}_t| d(s, t) \\ &= 2|e| \iint_{T_r} f(\mathbf{r}(s, t)) d(s, t) \end{aligned}$$

where  $|e|$  is the area of  $e$  and

$$|e| = \frac{1}{2} \|\mathbf{X}_s \times \mathbf{X}_t\| = \frac{1}{2} \|(\mathbf{v}_2 - \mathbf{v}_1) \times (\mathbf{v}_3 - \mathbf{v}_1)\|$$

Now using a symmetric  $n$ -point Gaussian quadrature rule on this reference triangle  $T_r$  yields the following approximation of the surface integral:

$$\begin{aligned} \iint_e f(\mathbf{r}) d\mathbf{r} &= 2|e| \iint_{T_r} f(\mathbf{r}(s, t)) d(s, t) \\ &\approx |e| \sum_{i=1}^{N_g} w_i f(\mathbf{r}(s_i, t_i)) \end{aligned}$$

### D.1.1 Choice of quadrature rule

In tables D.1 and D.2 one can find the particular symmetrical quadrature rule applied to the standard triangle that we have used in the implementation. This quadrature rule can be found in [6]. To avoid issues with respect to accuracy of the quadrature rule, we choose this slightly high-order quadrature rule. We choose the symmetrical quadrature rule where  $N_g = 61$  and  $p = 17$ , see [6, page 1142].

## D.2 Quadrature rule for line integrals over generic boundary elements

In a similar way we can define a quadrature rule for the line integral

$$\int_{be} f(\mathbf{r}) d\mathbf{r}$$

where  $be$  is a boundary line-element in  $\mathbb{R}^3$  and  $f$  is any vector-valued function  $f : \mathbb{R}^3 \rightarrow \mathbb{R}^3$  defined on  $be$ . To derive such a quadrature rule we will use the known line quadrature rules which are defined on the interval  $[-1, 1]$ , which we will call the reference interval. First we define the affine transformation  $\mathbf{r} : [-1, 1] \rightarrow be$  by

$$\mathbf{r}(\xi) = \begin{pmatrix} \frac{1}{2}(x_1 + x_2) + \frac{\xi}{2}(x_2 - x_1) \\ \frac{1}{2}(y_1 + y_2) + \frac{\xi}{2}(y_2 - y_1) \\ \frac{1}{2}(z_1 + z_2) + \frac{\xi}{2}(z_2 - z_1) \end{pmatrix} = \frac{1}{2}(\mathbf{v}_1 + \mathbf{v}_2) + \frac{\xi}{2}(\mathbf{v}_2 - \mathbf{v}_1)$$

Observe that  $\mathbf{r}(-1) = \mathbf{v}_1$  and  $\mathbf{r}(1) = \mathbf{v}_2$ . Using the fact that  $\left| \frac{d\mathbf{r}}{d\xi} \right| = \frac{1}{2}|be|$  where  $|be|$  is the length of the boundary element  $be$ , we have the following integral transformation

$$\begin{aligned} \int_{be} f(\mathbf{r}) d\mathbf{r} &= \int_{-1}^1 f(\mathbf{r}(\xi)) \left| \frac{d\mathbf{r}}{d\xi} \right| d\xi \\ &= \frac{|be|}{2} \int_{-1}^1 f(\mathbf{r}(\xi)) d\xi \end{aligned}$$

Applying an  $n$ -point line quadrature rule leads to the following approximation of the integral

$$\begin{aligned} \int_{be} f(\mathbf{r}) d\mathbf{r} &= \frac{|be|}{2} \int_{-1}^1 f(\mathbf{r}(\xi)) d\xi \\ &\approx \frac{|be|}{2} \sum_{i=1}^n w_i f(\mathbf{r}(\xi_i)) \end{aligned}$$

In table D.3 one can find the particular weights  $w_i$  and abscissa  $x_i$  that are used in the implementation in `MATLAB`. These linear quadrature rules can be found in most of the literature about quadrature rules.

## D.3 Tables of the quadrature rules

(see next page)

| $w_i$       | $s_i$       | $t_i$       |
|-------------|-------------|-------------|
| 0.033437199 | 0.333333333 | 0.333333333 |
| 0.005093415 | 0.005658919 | 0.497170541 |
| 0.005093415 | 0.497170541 | 0.005658919 |
| 0.005093415 | 0.497170541 | 0.497170541 |
| 0.014670865 | 0.035647355 | 0.482176323 |
| 0.014670865 | 0.482176323 | 0.035647355 |
| 0.014670865 | 0.482176323 | 0.482176323 |
| 0.024350878 | 0.099520062 | 0.450239969 |
| 0.024350878 | 0.450239969 | 0.099520062 |
| 0.024350878 | 0.450239969 | 0.450239969 |
| 0.031107551 | 0.199467521 | 0.400266239 |
| 0.031107551 | 0.400266239 | 0.199467521 |
| 0.031107551 | 0.400266239 | 0.400266239 |
| 0.031257111 | 0.495717464 | 0.252141268 |
| 0.031257111 | 0.252141268 | 0.495717464 |
| 0.031257111 | 0.252141268 | 0.252141268 |
| 0.024815654 | 0.675905991 | 0.162047005 |
| 0.024815654 | 0.162047005 | 0.675905991 |
| 0.024815654 | 0.162047005 | 0.162047005 |
| 0.014056073 | 0.848248235 | 0.075875883 |
| 0.014056073 | 0.075875883 | 0.848248235 |
| 0.014056073 | 0.075875883 | 0.075875883 |
| 0.003194676 | 0.968690546 | 0.015654727 |
| 0.003194676 | 0.015654727 | 0.968690546 |
| 0.003194676 | 0.015654727 | 0.015654727 |

Table D.1: Symmetrical Quadrature Rule for a triangle, part 1

| $w_i$       | $s_i$       | $t_i$       |
|-------------|-------------|-------------|
| 0.008119655 | 0.010186929 | 0.334319867 |
| 0.008119655 | 0.010186929 | 0.655493204 |
| 0.008119655 | 0.334319867 | 0.010186929 |
| 0.008119655 | 0.334319867 | 0.655493204 |
| 0.008119655 | 0.655493204 | 0.010186929 |
| 0.008119655 | 0.655493204 | 0.334319867 |
| 0.026805742 | 0.135440872 | 0.292221538 |
| 0.026805742 | 0.135440872 | 0.572337591 |
| 0.026805742 | 0.292221538 | 0.135440872 |
| 0.026805742 | 0.292221538 | 0.572337591 |
| 0.026805742 | 0.572337591 | 0.135440872 |
| 0.026805742 | 0.572337591 | 0.292221538 |
| 0.018459993 | 0.054423924 | 0.319574885 |
| 0.018459993 | 0.054423924 | 0.62600119  |
| 0.018459993 | 0.319574885 | 0.054423924 |
| 0.018459993 | 0.319574885 | 0.62600119  |
| 0.018459993 | 0.62600119  | 0.054423924 |
| 0.018459993 | 0.62600119  | 0.319574885 |
| 0.008476869 | 0.012868561 | 0.190704224 |
| 0.008476869 | 0.012868561 | 0.796427215 |
| 0.008476869 | 0.190704224 | 0.012868561 |
| 0.008476869 | 0.190704224 | 0.796427215 |
| 0.008476869 | 0.796427215 | 0.012868561 |
| 0.008476869 | 0.796427215 | 0.190704224 |
| 0.018292797 | 0.067165782 | 0.180483212 |
| 0.018292797 | 0.067165782 | 0.752351006 |
| 0.018292797 | 0.180483212 | 0.067165782 |
| 0.018292797 | 0.180483212 | 0.752351006 |
| 0.018292797 | 0.752351006 | 0.067165782 |
| 0.018292797 | 0.752351006 | 0.180483212 |
| 0.006665632 | 0.014663182 | 0.080711314 |
| 0.006665632 | 0.014663182 | 0.904625504 |
| 0.006665632 | 0.080711314 | 0.014663182 |
| 0.006665632 | 0.080711314 | 0.904625504 |
| 0.006665632 | 0.904625504 | 0.014663182 |
| 0.006665632 | 0.904625504 | 0.080711314 |

Table D.2: Symmetrical Quadrature Rule for a triangle, cont'd

| $w_i$              | $x_i$               |
|--------------------|---------------------|
| 0.0937684461602100 | 0.0000000000000000  |
| 0.0933564260655961 | -0.0936310658547334 |
| 0.0933564260655961 | 0.0936310658547334  |
| 0.0921239866433168 | -0.1864392988279916 |
| 0.0921239866433168 | 0.1864392988279916  |
| 0.0900819586606386 | -0.2776090971524970 |
| 0.0900819586606386 | 0.2776090971524970  |
| 0.0872482876188443 | -0.3663392577480734 |
| 0.0872482876188443 | 0.3663392577480734  |
| 0.0836478760670387 | -0.4518500172724507 |
| 0.0836478760670387 | 0.4518500172724507  |
| 0.0793123647948867 | -0.5333899047863476 |
| 0.0793123647948867 | 0.5333899047863476  |
| 0.0742798548439541 | -0.6102423458363790 |
| 0.0742798548439541 | 0.6102423458363790  |
| 0.0685945728186567 | -0.6817319599697428 |
| 0.0685945728186567 | 0.6817319599697428  |
| 0.0623064825303175 | -0.7472304964495622 |
| 0.0623064825303175 | 0.7472304964495622  |
| 0.0554708466316636 | -0.8061623562741665 |
| 0.0554708466316636 | 0.8061623562741665  |
| 0.0481477428187117 | -0.8580096526765041 |
| 0.0481477428187117 | 0.8580096526765041  |
| 0.0404015413316696 | -0.9023167677434336 |
| 0.0404015413316696 | 0.9023167677434336  |
| 0.0323003586323290 | -0.9386943726111684 |
| 0.0323003586323290 | 0.9386943726111684  |
| 0.0239155481017495 | -0.9668229096899927 |
| 0.0239155481017495 | 0.9668229096899927  |
| 0.0153217015129347 | -0.9864557262306425 |
| 0.0153217015129347 | 0.9864557262306425  |
| 0.0066062278475874 | -0.9974246942464552 |
| 0.0066062278475874 | 0.9974246942464552  |

Table D.3: The 33-point linear quadrature rule.

## E Expression of the magnetic field for uniform magnetized steel plates

The validation of the implementation of the forward problem is problematic because no closed form of the (total) magnetic induction field was known for any magnetization to the author. To come up with some validation we derive a closed form of the magnetic induction field, induced by a homogenous magnetization along the length of the plate. A similar computation can be made for homogenous magnetization along the width of the plate, so that for any uniform magnetization of the plate an closed form expression can be derived. This is for our validation not necessary so we omit that derivation.

A steel plate  $\mathcal{P}$  of length  $L$ , width  $W$  and thickness  $T$  is placed in a  $x, y, z$ -coordinate system such that the barycenter of  $\mathcal{P}$  coincides with the origin. Assuming that  $T \ll L, T \ll W$  we say that we consider a thin steel plate in the  $\{z = 0\}$  plane. Let the surface of this thin steel plate be denoted by  $\mathcal{S}$ . See figure E.1. The edges of the plate are labeled with  $L_1, L_2, R_1$  and  $R_2$ . Furthermore let

$$\mathbf{r}_1 = \begin{bmatrix} -\frac{l}{2} \\ -\frac{w}{2} \\ 0 \end{bmatrix}, \mathbf{r}_2 = \begin{bmatrix} -\frac{l}{2} \\ \frac{w}{2} \\ 0 \end{bmatrix}, \mathbf{r}_3 = \begin{bmatrix} \frac{l}{2} \\ -\frac{w}{2} \\ 0 \end{bmatrix}, \mathbf{r}_4 = \begin{bmatrix} \frac{l}{2} \\ \frac{w}{2} \\ 0 \end{bmatrix}$$

Assume that the plate is magnetized and that the magnetization of the plate is uniform in  $z$  so that we only have to describe the magnetization on  $\mathcal{S}$ . Let the magnetization on  $\mathcal{S}$  be given by  $\mathbf{M} = \mathbf{M}_u$  in the plate  $\mathcal{P}$  where

$$\mathbf{M}_u = M_x \mathbf{u}_x$$

is a uniform magnetization of the plate (here  $\mathbf{u}_x$  is an unit vector). The magnetic induction field  $\mathbf{B}$  is given by the following expression analytical expression (where two terms of the expression of  $\mathbf{B}$  vanishes due to the absence of  $\nabla \cdot \mathbf{M}$  and  $\mathbf{n} \cdot \mathbf{M} = 0$  for normal vectors  $\mathbf{n}$  defined on the surface  $\mathcal{S}$ ; there is no component of the magnetization  $\mathbf{M}$  in the  $z$ -direction.)

$$\mathbf{B}(\mathbf{r}) = -\frac{\mu_0 T}{4\pi} \oint_{\partial \mathcal{S}} \frac{\mathbf{r} - \mathbf{r}'}{|\mathbf{r} - \mathbf{r}'|^3} (-\mathbf{n}) \cdot \mathbf{M}(\mathbf{r}') d\mathbf{r}'$$

We have derived that for a uniform magnetization the divergence of  $\mathbf{M}$  vanishes in the interior of the plate and  $\mathbf{n} \cdot \mathbf{M}$  is constant along the edges of the plate. In particular

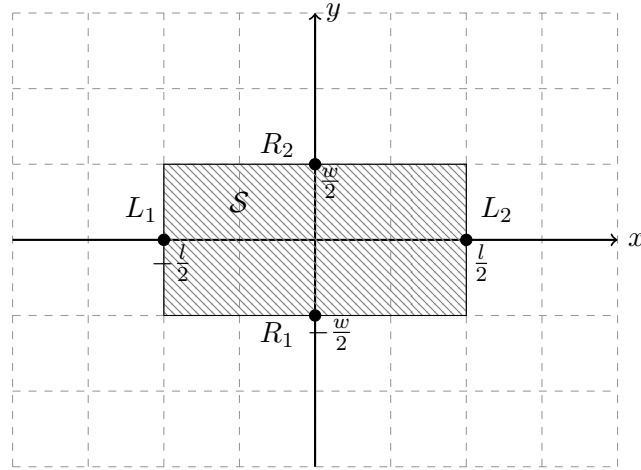


Figure E.1: A steel plate

we have that

$$\mathbf{n} \cdot \mathbf{M} = 0 \text{ on } R_1 \cup R_2, \quad \mathbf{n} \cdot \mathbf{M} = -M_x \text{ on } L_1, \quad \mathbf{n} \cdot \mathbf{M} = M_x \text{ on } L_2$$

$$\begin{aligned} \mathbf{B}(\mathbf{r}) &= -\frac{\mu_0 T}{4\pi} \int_{\delta S} \frac{\mathbf{r} - \mathbf{r}'}{|\mathbf{r} - \mathbf{r}'|^3} (-\mathbf{n}) \cdot \mathbf{M}(\mathbf{r}') d\mathbf{r}' \\ &= -\frac{\mu_0 T}{4\pi} \left[ \int_{L_1} \frac{\mathbf{r} - \mathbf{r}'}{|\mathbf{r} - \mathbf{r}'|^3} (-\mathbf{n}) \cdot \mathbf{M}(\mathbf{r}') d\mathbf{r}' + \int_{L_2} \frac{\mathbf{r} - \mathbf{r}'}{|\mathbf{r} - \mathbf{r}'|^3} (-\mathbf{n}) \cdot \mathbf{M}(\mathbf{r}') d\mathbf{r}' \right. \\ &\quad \left. + \int_{R_1} \frac{\mathbf{r} - \mathbf{r}'}{|\mathbf{r} - \mathbf{r}'|^3} (-\mathbf{n}) \cdot \mathbf{M}(\mathbf{r}') d\mathbf{r}' + \int_{R_2} \frac{\mathbf{r} - \mathbf{r}'}{|\mathbf{r} - \mathbf{r}'|^3} (-\mathbf{n}) \cdot \mathbf{M}(\mathbf{r}') d\mathbf{r}' \right] \\ &= -\frac{\mu_0 T}{4\pi} \left[ \int_{L_1} \frac{\mathbf{r} - \mathbf{r}'}{|\mathbf{r} - \mathbf{r}'|^3} (-\mathbf{n}) \cdot \mathbf{M}(\mathbf{r}') d\mathbf{r}' + \int_{L_2} \frac{\mathbf{r} - \mathbf{r}'}{|\mathbf{r} - \mathbf{r}'|^3} (-\mathbf{n}) \cdot \mathbf{M}(\mathbf{r}') d\mathbf{r}' \right] \end{aligned}$$

We will compute each of the integrals above by appropriate transforms discussed in the previous section. On the edges  $L_1$  and  $L_2$  we use the following transformations

$$\mathbf{r}'_1(t) = \begin{bmatrix} -\frac{L}{2} \\ \frac{W}{2}t \\ 0 \end{bmatrix}, \quad t \in [-1, 1] \quad \text{and} \quad \mathbf{r}'_2(t) = \begin{bmatrix} \frac{L}{2} \\ \frac{W}{2}t \\ 0 \end{bmatrix}, \quad t \in [-1, 1]$$

respectively. Applying these transformations leads to the following computation:

$$\begin{aligned} \mathbf{B}(\mathbf{r}) &= -\frac{\mu_0 T M_x}{4\pi} \left[ \int_{L_1} \frac{\mathbf{r} - \mathbf{r}'}{|\mathbf{r} - \mathbf{r}'|^3} d\mathbf{r}' - \int_{L_2} \frac{\mathbf{r} - \mathbf{r}'}{|\mathbf{r} - \mathbf{r}'|^3} d\mathbf{r}' \right] \\ &= -\frac{\mu_0 W T M_x}{8\pi} \left[ \int_{-1}^1 \frac{\mathbf{r} - \mathbf{r}'_1(t)}{|\mathbf{r} - \mathbf{r}'_1(t)|^3} dt - \int_{-1}^1 \frac{\mathbf{r} - \mathbf{r}'_2(t)}{|\mathbf{r} - \mathbf{r}'_2(t)|^3} dt \right] \end{aligned}$$

We will now consider each component of  $\mathbf{B}(\mathbf{r})$  to derive further simplifications. Further

derivation leads to:

$$\begin{aligned}\mathbf{B}_x(\mathbf{r}) &= -\frac{\mu_0 W T M_x}{8\pi} \left[ \int_{-1}^1 \frac{x + \frac{L}{2}}{|\mathbf{r} - \mathbf{r}'_1(t)|^3} dt - \int_{-1}^1 \frac{x - \frac{L}{2}}{|\mathbf{r} - \mathbf{r}'_2(t)|^3} dt \right] \\ &= -\frac{\mu_0 W T M_x}{8\pi} \left[ \left(x + \frac{L}{2}\right) \int_{-1}^1 \frac{1}{|\mathbf{r} - \mathbf{r}'_1(t)|^3} dt - \left(x - \frac{L}{2}\right) \int_{-1}^1 \frac{1}{|\mathbf{r} - \mathbf{r}'_2(t)|^3} dt \right]\end{aligned}$$

The two integrals can be computed in a closed form. For now we denote them by

$$\mathcal{I}_1(\mathbf{r}) = \int_{-1}^1 \frac{1}{|\mathbf{r} - \mathbf{r}'_1(t)|^3} dt, \quad \mathcal{I}_2(\mathbf{r}) = \int_{-1}^1 \frac{1}{|\mathbf{r} - \mathbf{r}'_2(t)|^3} dt$$

The expression for  $\mathbf{B}_x$  turns into the simple form

$$\mathbf{B}_x(\mathbf{r}) = -\frac{\mu_0 W T M_x}{8\pi} \left[ \left(x + \frac{L}{2}\right) \mathcal{I}_1(\mathbf{r}) - \left(x - \frac{L}{2}\right) \mathcal{I}_2(\mathbf{r}) \right]$$

Similar simplification can be made for the  $y$  and  $z$  component of the magnetic induction field  $\mathbf{B}$ . This leads to

$$\begin{aligned}\mathbf{B}_y(\mathbf{r}) &= -\frac{\mu_0 W T M_x}{8\pi} \left[ \int_{-1}^1 \frac{y - \frac{W}{2}t}{|\mathbf{r} - \mathbf{r}'_1(t)|^3} dt - \int_{-1}^1 \frac{y - \frac{W}{2}t}{|\mathbf{r} - \mathbf{r}'_2(t)|^3} dt \right] \\ &= -\frac{\mu_0 W T M_x}{8\pi} [\mathcal{I}_3(\mathbf{r}) - \mathcal{I}_4(\mathbf{r})]\end{aligned}$$

$$\text{where } \mathcal{I}_3(\mathbf{r}) = \int_{-1}^1 \frac{y - \frac{W}{2}t}{|\mathbf{r} - \mathbf{r}'_1(t)|^3} dt, \quad \mathcal{I}_4(\mathbf{r}) = \int_{-1}^1 \frac{y - \frac{W}{2}t}{|\mathbf{r} - \mathbf{r}'_2(t)|^3} dt.$$

For the  $z$ -component of the magnetic induction field we have

$$\begin{aligned}\mathbf{B}_z(\mathbf{r}) &= -\frac{\mu_0 W T M_x}{8\pi} \left[ \int_{-1}^1 \frac{z}{|\mathbf{r} - \mathbf{r}'_1(t)|^3} dt - \int_{-1}^1 \frac{z}{|\mathbf{r} - \mathbf{r}'_2(t)|^3} dt \right] \\ &= -\frac{\mu_0 W T M_x}{8\pi} [z (\mathcal{I}_1(\mathbf{r}) - \mathcal{I}_2(\mathbf{r}))]\end{aligned}$$

It remains to compute the four integrals  $\mathcal{I}_1, \dots, \mathcal{I}_4$ . To this end we use the following closed expressions:

$$\int \frac{1}{\sqrt{a + (b - ct)^2}} dt = \frac{b - ct}{ac\sqrt{a + (b - ct)^2}} + C$$

$$\int \frac{b - ct}{\sqrt{a + (b - ct)^2}} dt = \frac{1}{c\sqrt{a + (b - ct)^2}} + C$$

Using appropriate substitutions of the values of  $a$ ,  $b$  and  $c$  gives us a way to compute the integrals  $\mathcal{I}_1, \dots, \mathcal{I}_4$ . After defining the functions

$$\begin{aligned}\mathcal{F}_1(\mathbf{r}, t) &= \frac{1}{(x + \frac{L}{2})^2 + z^2} \frac{y - \frac{W}{2}t}{\sqrt{(x + \frac{L}{2})^2 + (y + \frac{W}{2}t)^2 + z^2}} \\ \mathcal{F}_2(\mathbf{r}, t) &= \frac{1}{(x - \frac{L}{2})^2 + z^2} \frac{y - \frac{W}{2}t}{\sqrt{(x - \frac{L}{2})^2 + (y + \frac{W}{2}t)^2 + z^2}} \\ \mathcal{F}_3(\mathbf{r}, t) &= \frac{1}{\sqrt{(x + \frac{L}{2})^2 + (y - \frac{W}{2}t)^2 + z^2}} \\ \mathcal{F}_4(\mathbf{r}, t) &= \frac{1}{\sqrt{(x - \frac{L}{2})^2 + (y - \frac{W}{2}t)^2 + z^2}}\end{aligned}$$

and some refreshing computations we have the following closed form expressions for the integrals  $\mathcal{I}_1, \dots, \mathcal{I}_4$ :

$$\begin{aligned}\mathcal{I}_1(\mathbf{r}) &= \frac{2}{W} (\mathcal{F}_1(\mathbf{r}, 1) - \mathcal{F}_1(\mathbf{r}, -1)) \\ \mathcal{I}_2(\mathbf{r}) &= \frac{2}{W} (\mathcal{F}_2(\mathbf{r}, 1) - \mathcal{F}_2(\mathbf{r}, -1)) \\ \mathcal{I}_3(\mathbf{r}) &= \frac{2}{W} (\mathcal{F}_3(\mathbf{r}, 1) - \mathcal{F}_3(\mathbf{r}, -1)) \\ \mathcal{I}_4(\mathbf{r}) &= \frac{2}{W} (\mathcal{F}_4(\mathbf{r}, 1) - \mathcal{F}_4(\mathbf{r}, -1))\end{aligned}$$

Using these expressions leads to the following closed form expressions of the  $x$ ,  $y$  and  $z$  component of the magnetic induction field

$$\begin{aligned}\mathbf{B}_x(\mathbf{r}) &= \frac{\mu_0 T M_x}{4\pi} \left[ \left( x + \frac{L}{2} \right) \left( \mathcal{F}_1(\mathbf{r}, 1) - \mathcal{F}_1(\mathbf{r}, -1) \right) - \left( x - \frac{L}{2} \right) \left( \mathcal{F}_2(\mathbf{r}, 1) - \mathcal{F}_2(\mathbf{r}, -1) \right) \right] \\ \mathbf{B}_y(\mathbf{r}) &= \frac{\mu_0 T M_x}{4\pi} \left[ \mathcal{F}_3(\mathbf{r}, 1) - \mathcal{F}_3(\mathbf{r}, -1) - \left( \mathcal{F}_4(\mathbf{r}, 1) - \mathcal{F}_4(\mathbf{r}, -1) \right) \right] \\ \mathbf{B}_z(\mathbf{r}) &= \frac{\mu_0 T M_x}{4\pi} \left[ z \left( \mathcal{F}_1(\mathbf{r}, 1) - \mathcal{F}_1(\mathbf{r}, -1) \right) - z \left( \mathcal{F}_2(\mathbf{r}, 1) - \mathcal{F}_2(\mathbf{r}, -1) \right) \right]\end{aligned}$$

## F Development of the M4

In the figure below the development of the M4 can be found. This development was the first sketch in the creation of the M4 by the Marine Bedrijf. We see some measures of the boat, namely, we can see that the boat is 5 meters long, 2 meters wide and approximately 1 meter high.

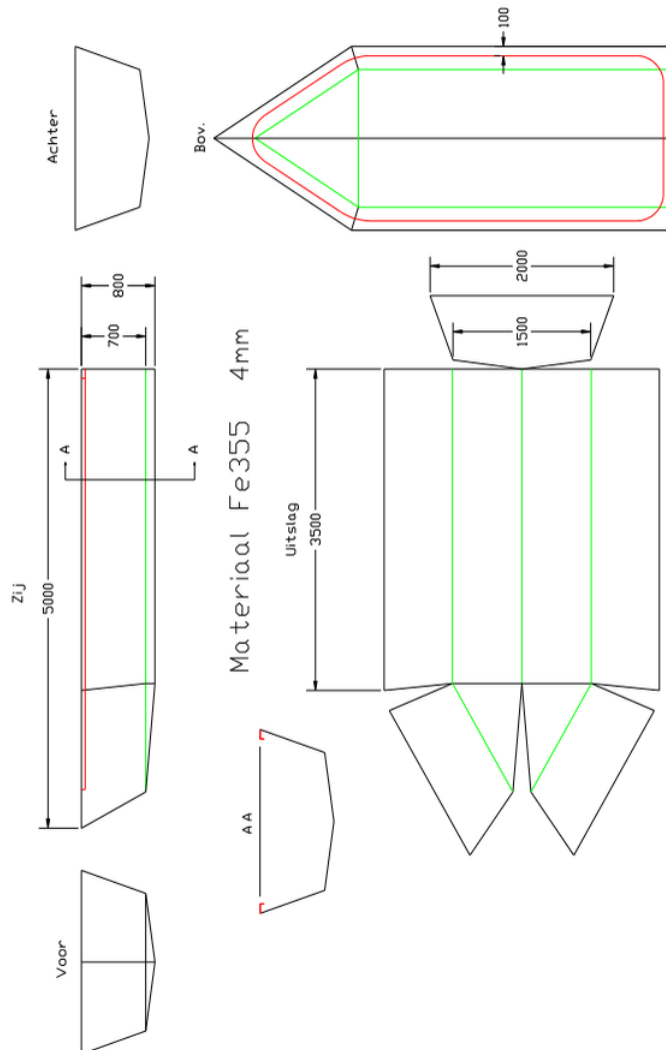


Figure F.1: Development of the M4. © Jan Sijs